The Dissertation Committee for Lawrence Robert Dunn Certifies that this is the approved version of the following dissertation:

Device Physics of Organic Field Effect Transistors and Organic Photovoltaic Devices

Committee:

Ananth Dodabalapur, Supervisor

Zhen Yao, Co-Supervisor

Greg Sitz

John Markert

Li Xiaoqin

Device Physics of Organic Field Effect Transistors and Organic Photovoltaic Devices

by

Lawrence Robert Dunn, B.A.; M.A.

Dissertation

Presented to the Faculty of the Graduate School of

The University of Texas at Austin

in Partial Fulfillment

of the Requirements

for the Degree of

Doctor of Philosophy

The University of Texas at Austin

December, 2008

Dedication

To My Family

Acknowledgements

First and foremost I would like to thank Prof. Ananth Dodabalapur for giving me the chance to join his group, and for constantly inspiring me to conduct research at the highest levels. I have learned a tremendous amount under his guidance. I would also like to thank the other members of my dissertation committee: Prof. Zhen Yao, for co-supervising my degree, Prof. John Markert, Prof. Greg Sitz, and Prof. Li Xiaoqin.

I would also like to thank my former co-supervisor at the Institute of Materials Research and Engineering, Prof. Alan Sellinger, for all of his help, guidance, and advice. My colleagues at IMRE were always a constant source of knowledge of inspiration. These include Dr. Thomas Kietzke, Dr. Ooi Zi-En, Dr Samarendra Singh, Dr. Prashant Sonar, Dr. Thelese Foong Ru Bao, Dr. Soh Mui Siang, Dr. Sudhakar Sundarraj, Dr. Cristina Tanese, and Tam Teck Lip.

I would like to thank my University of Texas group members Dr. Liang Wang, Dr. Tae Ho Jung, Deepak Sharma, Dr. Suvid Nadkarni, Davianne Duarte, Shannon Lewis, Chris Lombardo, Jae Won Shim, Chenguan Lee, Dr. Somya Dutta, and Dr. Daniel Fine. In particular Dr. Byungwook Yoo, Brian Cobb, Dharmendar Reddy, and Dr. Debarshi Basu deserve special recognition for their helpful ideas, suggestions, and aid in device fabrication.

Finally I would like to thank my family—my mother, father, brother, and sister—for their constant support, love, and understanding.

Device Physics of Organic Field Effect Transistors and Organic Photovoltaic Devices

Publication No._____

Lawrence Robert Dunn, Ph.D.

The University of Texas at Austin, 2008

Supervisors: Ananth Dodabalapur, Zhen Yao

In this dissertation novel work is presented showing the performance and device physics of Organic Field Effect Transistors (OFETs) and bulk heterojunction Organic Photovoltaic (OPV) devices fabricated using novel acceptor small molecules. Pentacene and *N,N'*-bis(n-octyl)-dicyanoperylene-3,4:9,10-bis(dicarboximide) (PDI-8CN_2) were used as the active layer in p-channel and n-channel Organic Field Effect Transistors (OFETs), respectively, and novel pulsed voltage transient measurements were developed in order to extract transient mobilities and carrier velocities from the transistor response of the device, which were well correlated with the corresponding DC OFET characteristics. A distributed RC network was used to model the OFET's channel and the transient and DC characteristics of the devices were successfully reproduced. Temperature dependent studies of the DC field effect mobilities and transient mobilities of these two materials were carried out and the results used to extract information on charge carrier transport in the materials at varying time scales.

Open-circuit voltages of the OPV devices are correlated with the Highest Occupied Molecular Orbital (HOMO) and Lowest Unoccupied Molecular Orbital

(LUMO) levels various acceptor small molecules and donor polymers comprising the active layers of the devices.

Table of Contents

List of Figures

Chapter 1: Introduction to Organic Semiconductors

1.1: History, Background, and Motivation.

Photoconductivity in Organic crystals was first observed in anthracene in 1906 by Pochettino[1]. Early studies of organic semiconductors were concentrated on anthracene in single crystal form, although in the decades that followed experimental work on thin films of dye molecules such as metal-phthalocyanines and perylene derivatives were carried out that lead to their use as the photoconductive thin films coating the drums found in all xerographic devices[2]. This was the first major commercial success for organic semiconductors.

Polymeric semiconductors were discovered by accident in 1976 by Alan MacDiarmid, Hideki, and Alan Heeger, when a graduate student mistakenly introduced an amount of catalyst to induce a polymerization reaction that was several orders of magnitude to great. Instead of the dull black polymer they were expecting, they observed a shiny silvery material that was the world's first conductive polymer. MacDiarmid, Hideki, and Heeger were awarded the Nobel Prize in Chemistry for their discovery in 2000.

It turns out that energy gap separating the *2s* orbital from the three *2p* orbitals in Carbon is small compared to the binding energy of chemical bonds (*e.g.,* the $2s2p^3$ excited state is separated from the $2s^22p^2$ ground state by only 4.18 eV[3]), and so the wave functions of the electrons in the *2s* and *2p* orbitals easily mix to form hybrid orbitals in cases where the total energy of the molecule being formed is lowered by doing so.

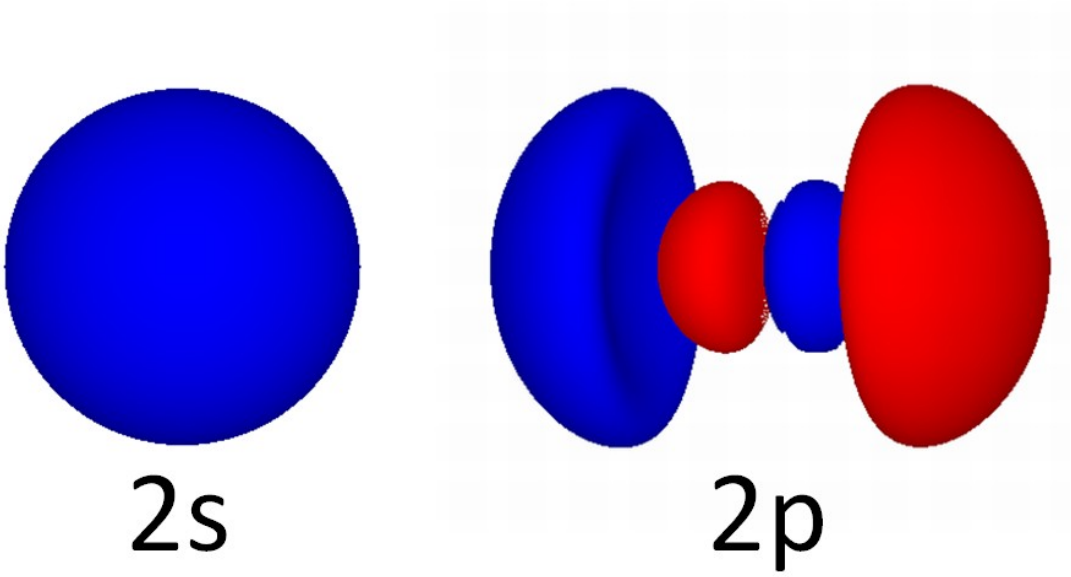

Figure 1.1: 2s and 2p orbitals of an individual carbon atom.

If the single *2s* orbital hybridizes with a single *2p* orbital, the resulting two orbitals are labeled *sp* orbitals. Methane, a tetrahedral molecule consisting of one Carbon at the center and 4 hydrogens in a pyramidal structure around the Carbon, is an example of sp^3 hybridization, in which all three *2p* orbitals hybridize with the *2s* orbital. A methane molecule is depicted in Figure 1.2 for illustrative purposes. Incidentally, the sp^3 hybridization configuration of carbon is the most common type of bonding for the vast majority of plastics. In these materials, each carbon atom is linked to its four neighbors via the four strong σ bonds. Because these σ bonds are so strong, the distance between highest and lowest occupied molecular electronic orbitals is very large, which explains why most plastics are both transparent to light and are insulating materials[4].

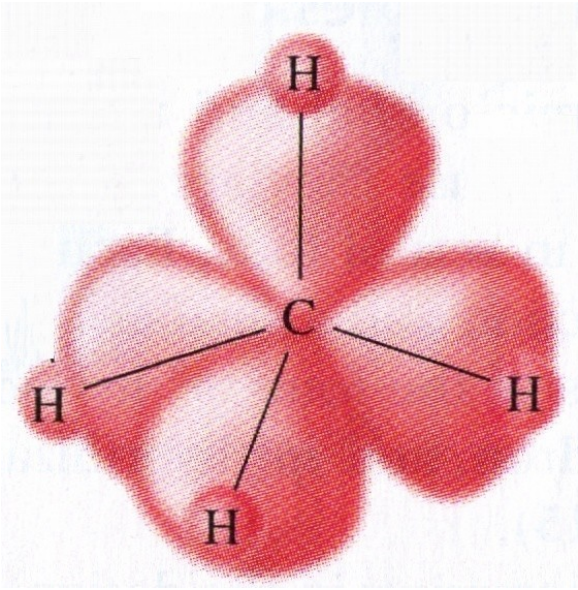

Figure 1.2: a drawing of a methane molecule illustrating the formation of four sp^3 hybrid bonds. From BROWN/FOOTE. *ORGANIC CHEMISTRY 2E*, 2E[5]. © 1998 Brooks/Cole, a part of Cengage Learning, Inc. Reproduced by permission. www.cengage.com/permissions

The type of hybridization which is of greatest interest to us, which occurs in all organic semiconductors, is sp^2 hybridization, where the *2s* orbital combines with what are conventionally labeled the $2p_x$ and $2p_y$ to form three co-planar "σ-bonding" orbitals with an angle of 120 degrees between neighboring bonds.

Following Saito *et. al*.[3], we may express the sp^2 orbitals mathematically as a linear combination of the *2s*, $2p_x$, and $2p_y$ orbitals. Since we know the angle between each σ bond originating from a Carbon atom is 120 degrees, if we take the plane of the σ bonds to be the *xy* plane, and a Carbon atom at the origin, the directions of the three σ bonds may be expressed $(0,-1,0)$, $\left(\frac{\sqrt{3}}{2},\frac{1}{2},0\right)$, and $\left(-\frac{\sqrt{3}}{2},\frac{1}{2},0\right)$. The three σ-bonding ($sp^2$) orbitals may therefore be expressed:

$$
\begin{aligned}
\left|sp_a^2\right\rangle &= C_1\left|2s\right\rangle - \sqrt{1-C_1^2}\left|2p_y\right\rangle \\
\left|sp_b^2\right\rangle &= C_2\left|2s\right\rangle - \sqrt{1-C_2^2}\left[\frac{\sqrt{3}}{2}\left|2p_x\right\rangle + \frac{1}{2}\left|2p_y\right\rangle\right] \\
\left|sp_c^2\right\rangle &= C_3\left|2s\right\rangle - \sqrt{1-C_3^2}\left[-\frac{\sqrt{3}}{2}\left|2p_x\right\rangle + \frac{1}{2}\left|2p_y\right\rangle\right]
\end{aligned}
\tag{1.1}
$$

where the notation designating the *2s*, *2p*, and sp^2 orbitals is self explanatory. From the orthonormality requirements of these three states we may obtain the following three relationships shown below.

$$
\begin{aligned}
&C_1^2 + C_2^2 + C_3^2 = 1 \\
&C_1C_2 - \frac{1}{2}\sqrt{1-C_1^2}\sqrt{1-C_2^2} = 0 \\
&C_1C_3 - \frac{1}{2}\sqrt{1-C_1^2}\sqrt{1-C_3^2} = 0
\end{aligned}
\tag{1.2}
$$

The solution to the system of equations shown in equation 1.2 are given by $C_1 = C_2 = 1/\sqrt{3}$, and $C_3 = -1/\sqrt{3}$.

The electrons in the unaltered $2p_z$ orbitals participate in what are generally referred to as "π-bonds" that are delocalized above and below the plane of the molecule. The simplest example of this sp^2 hybridization is the molecule ethylene, which is shown in Figure 1.3.

Because the wave functions of the two electrons in ethylene's π orbitals have virtually no overlap with the electrons in the σ orbitals, the π orbital may essentially be thought of as a two-electron system. And since electrons are fermions, the two electron wave function of the electrons in the π orbital must be antisymmetric under exchange[6].

The total state of an electron may be specified by the product of its position wave function, and a spinor describing the orientation of its spin:

$$\Psi(\boldsymbol{r},\boldsymbol{s}) = \psi(\boldsymbol{r})\chi(\boldsymbol{s}) \tag{1.3}$$

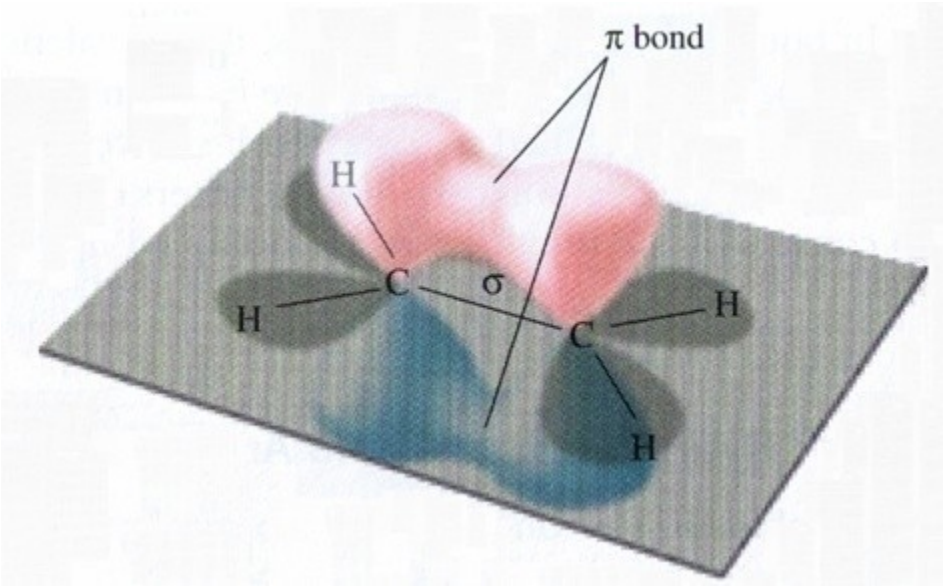

Figure 1.3: A drawing of an Ethylene (C_2H_4) molecule illustrating the formation of σ bond in the molecular plane and π bond above and below molecule. From BROWN/FOOTE. *ORGANIC CHEMISTRY 2E*, 2E[5]. © 1998 Brooks/Cole, a part of Cengage Learning, Inc. Reproduced by permission. www.cengage.com/permissions

For a two electron system, there are four possible spin configurations: three "triplet" (spin = 1) states and one "singlet (spin = 0) state. Using the notation $|s\, m_s\rangle$ to denote the spin state of a two electron system with spin s and a spin projection quantum number m_s, the singlet state is:

$$|00\rangle = \frac{1}{\sqrt{2}}\left(\psi_{\uparrow}(s_1)\psi_{\downarrow}(s_2) - \psi_{\uparrow}(s_2)\psi_{\downarrow}(s_1)\right) \tag{1.4}$$

and the three triplet states are:

$$
\begin{aligned}
|11\rangle &= \psi_{\uparrow}(s_1)\psi_{\uparrow}(s_2) \\
|10\rangle &= \frac{1}{\sqrt{2}}\left(\psi_{\uparrow}(s_1)\psi_{\downarrow}(s_2) + \psi_{\uparrow}(s_2)\psi_{\downarrow}(s_1)\right) \\
|1-1\rangle &= \psi_{\downarrow}(s_1)\psi_{\downarrow}(s_2)
\end{aligned}
\tag{1.5}
$$

It is clear that the composite singlet spin state is already antisymmetric under exchange, while the three composite triplet spin states are symmetric. Therefore in order to satisfy our basic antisymmetric requirement for a fermionic two-particle system, the singlet spin state must be combined with a symmetric spatial wave function, while the three triplet spin states have to be combined with antisymmetric spatial wave functions. Because of these spatial wave function symmetry requirements, singlet (spin = 0) states are referred to as "bonding", while triplet (spin = 1) are referred to as "antibonding". In the context of an ethylene molecule exhibiting sp^2 hybridization (and for organic semiconductors more generally), the bonding (singlet) configuration corresponds to the Highest Occupied Molecular Orbital (HOMO) of the π electrons, and the first excited state of the π electrons is called the Lowest Unoccupied Molecular Orbital (LUMO).

If we imagine two superimposed ethylene molecules, one over the other, it is instructive to investigate the interactions of the π-electrons of the two molecules. In this case the HOMO of the molecule is spatially symmetric, resulting in a lack of a node of the electronic wave function in the center of the molecule, where as the LUMO of the molecule is spatially antisymmetric. As two molecules are brought together resulting in a splitting of the HOMO and LUMO levels, the bonding nature of the HOMO level interaction results in a very large splitting of that level (0.539 eV for an intermolecular distance of 4 Å), while the LUMO level splitting (0.148 eV at the same intermolecular

distance) is much smaller due to the antibonding interaction of the orbital nodes from neighboring molecules[7]. This interaction, and the corresponding extension to extended "band" states as the number of interacting molecules increases, is illustrated in Figure 1.4.

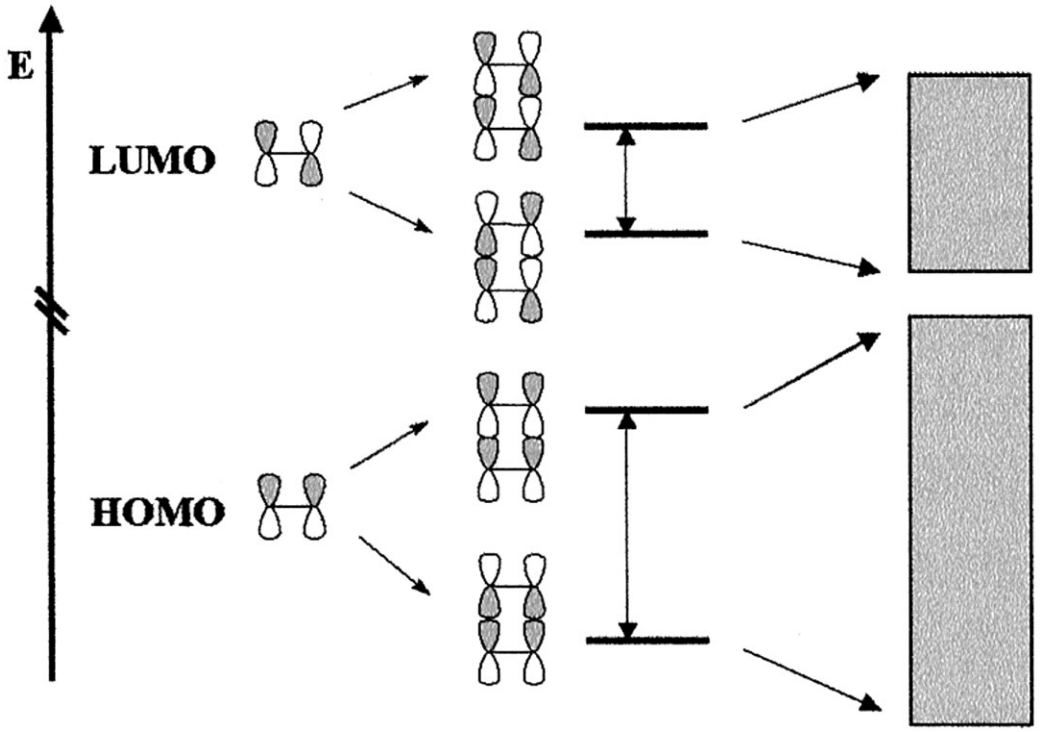

Figure 1.4: Bonding and Antibonding interaction electrons in the $2p_z$ orbitals of two cofacial ethylene molecules stacked on top of one another. The transition to extended HOMO and LUMO "bands" is also illustrated as the number of ethylene molecules stacked on top of one another increases. Figure reproduced with permission from Brédas *et. al.*[7]

It is these delocalized π-electrons that are responsible for the electronic behavior of organic semiconductors. The extent to which π-electrons of neighboring molecules interact determines the interchain transfer integral, *t*, which in turn determines the ease of

transferring a charge between neighboring molecules or segments of a polymer or small molecule.

1.2: CONJUGATION AND PEIERL'S DISTORTION IN POLYACETYLENE

Arguably the simplest organic solid exhibiting sp^2 hybridization is the polymer Polyacetylene. *Trans*-Polyacetylene is depicted in Figure 1.5.

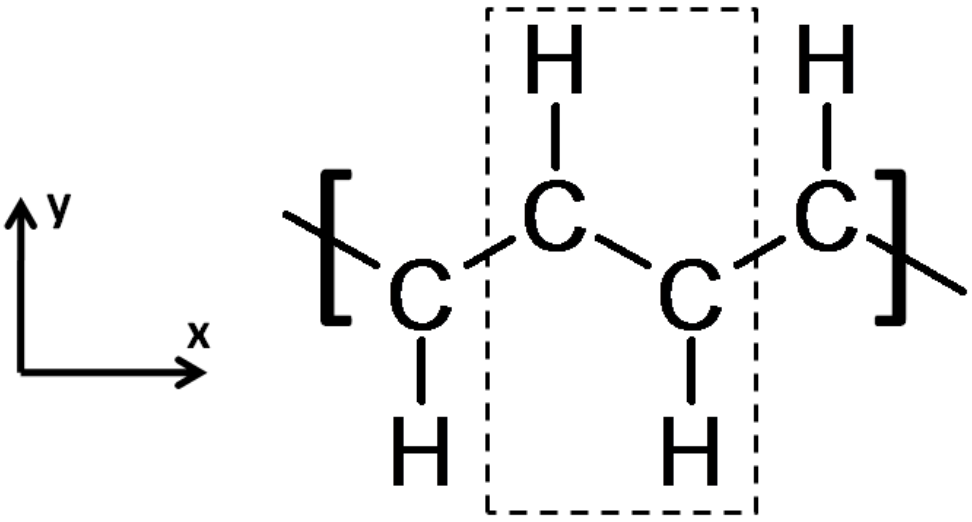

Figure 1.5: Chemical diagram of Polyacetylene. The dashed box contains a single unit cell of the polymer. The fourth valence electron of each Carbon atom is delocalized in the $2p_z$ orbitals above and below the polymer chain.

In Figure 1.5 the fourth valence electron of every Carbon atom occupies that atom's unaltered $2p_z$ orbital, which in this context is generally referred to as a π-orbital. The π-orbitals of neighboring Carbon atoms in an organic semiconductor are typically delocalized over a few dozen atoms forming a "π-band" over that portion of the molecule. As this π-band is only half filled, an initial analysis would suggest that Polyacetylene should possess the electronic and physical properties of a metal.

Indeed, if we assume that each Carbon atom is equidistant from its nearest neighbor and is separated by a distance *a*, the unit cell of Polyacetylene would contain only one Carbon and one hydrogen, and the basic cell in reciprocal space would be

$$-\frac{\pi}{a} < k < \frac{\pi}{a} \tag{1.6}$$

so that electrons occupying the π-band would experience a period potential which would yield a dispersion relation that might look something like Figure 1.6.

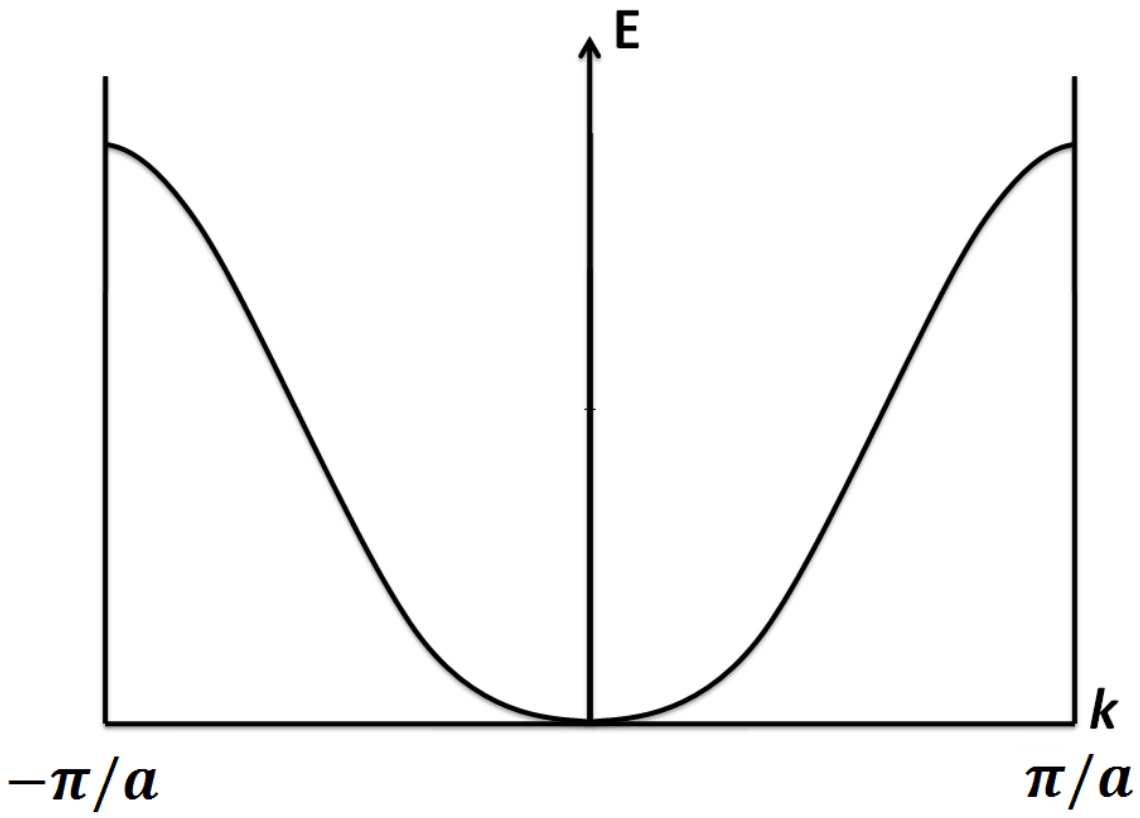

Figure 1.6: Band diagram of a hypothetical 1-D metal with no distortion in the linear chain.

However if every second Carbon atom is slightly displaced, the unit cell would then be as it appears in Figure 1.5: it would contain two Carbon atoms, and only

multiples of *2a* would now be lattice vectors. The basic cell in reciprocal space would now be

$$-\frac{\pi}{2a} < k < \frac{\pi}{2a} \tag{1.7}$$

and the dispersion relation would now possess two separate bands. Following the derivation in Peierls[8], the affect of the altered periodic potential would be produce a discontinuity at the dispersion relation at

$$k_\rho = \pm\frac{\pi}{2a} \tag{1.8}$$

with a magnitude

$$\Delta E = 2\int \psi^*_{k_\rho}(x)(\delta V)\,\psi^*_{-k_\rho}(x)dx \tag{1.9}$$

where ψ is the wave function of the π-electron in the undistorted chain, and δV is the change in the period potential due to the physical displacement of every second Carbon atom. This energy gap, ΔE, is analogous to the gap between the valence and conduction bands of inorganic semiconductors, and is responsible for the semiconducting nature of these materials. In general the magnitude of ΔE in most organic semiconductors is on the order of 1 eV.

Because the energy of the completely filled (π or HOMO) band near the edges of the Brillouin zone will be lowered, and the excited (π^* or LUMO) band is empty, the total energy of Polyacetylene chain is lowered by slightly displacing every second Carbon atom. In general, there will always be some lattice distortion in a one-dimensional lattice that will produce discontinuities in the dispersion relation precisely at or near the edge of the Fermi distribution, and in doing so will lower the total energy of the solid. This is

referred to as Peierl's distortion, and in the case of Polyacetylene is the justification for depicting alternating single and double bonds in its chemical structure.

1.3: CHARGE TRANSPORT IN ORGANIC SEMICONDUCTORS: BAND LIKE VS. LOCALIZED TRANSPORT

In highly purified molecular crystals, so many neighboring molecules interact electronically that the HOMO and LUMO level splitting results in energy levels can support true band-like transport of electrons and/or holes. In the 1980s and 1990s Karl and his coworkers performed many of the seminal time of flight (TOF) mobility studies on single crystals of naphthalene, anthracene, and perylene, proving that at low temperatures charge transport in these materials exhibited the hall marks of bandlike transport[9-11]. These hallmarks include a relatively high mobility, μ, (greater than 1 cm^2/Vs), an increase of mobility with decreasing temperature ($\mu \propto T^n,\ n < -1$) due to the reduced disruption of the HOMO and LUMO bands from phonon interactions, and a decreasing mobility with increasing electric field due to velocity saturation of charges resulting from phonon scattering[10,12]. In general, bandwidths of at least 0.1 eV are required to support bandlike transport[4], and the mobilities of holes or electrons are related to the widths of the HOMO or LUMO bands, respectively. Because the HOMO and LUMO bandwidths are directly related to the transfer integral of the electronic wave functions between neighboring molecules, charge carrier mobility can vary dramatically with crystallographic direction.

It is important to note that unlike conventional atomic crystalline semiconductors, which are typically covalent solids, organic molecular semiconductors (molecular crystals, polymers, vapor-deposited molecular glasses, etc.) are held together by relatively weak Van der Waals forces[12]. The relatively weak nature of these intermolecular bonds means that a free charge carrier located on a molecule will cause both a polarization of the charge carriers of the surrounding molecules, and also a distortion of the lattice itself. The electronic polarization of the neighboring molecules may be thought of as a local cloud of excitons (bound electron-hole pairs) on neighboring molecules surrounding the charge carrier, and the lattice distortion may be viewed as a cloud of phonons surrounding the charge carrier as it moves. Another polarization that manifests itself with the appearance of a free charge carrier is the molecular polarization, which involves a distortion of the nuclei of the charged molecule. This lattice distortion and electronic polarization can involve as many as 10^4 molecules or more (corresponding to a radius of approximately 150 Å), and together with the free charge carrier is called a polaron[12].

The order of magnitude of electronic polarization time (τ_{EP}), lattice distortion time (τ_{LD}), molecular polarization time (τ_{MP}), and carrier residence time (τ_{RES}), may all be estimated from the Heisenberg uncertainty relation:

$$\tau \lesssim \frac{\hbar}{\Delta E} \tag{1.10}$$

where ΔE for the carrier residence time is the HOMO or LUMO bandwidth for holes or electrons, respectively, typically on the order of 0.1 eV in organic semiconductors,

resulting in an estimated carrier residence time of ~10^{-14}s. This is about two orders of magnitude longer than the corresponding carrier residence time in inorganic semiconductors, where typically bandwidths are on the order of 10 eV. The energy gap between the HOMO and LUMO (~1 eV) may be used to place the electronic polarization time at about 10^{-15}s for both inorganic and organic semiconductors. Finally the order of magnitude of the molecular and lattice polarization times may be estimated from molecular and lattice vibration energies, respectively. The molecular vibration energy is typically on the order of 0.1 eV, while the lattice vibration energy is typically less than .01 eV, resulting in a characteristic molecular polarization time of 10^{-14} s, and a lattice distortion time greater than ~10^{13}s[4].

These figures may be contrasted with the figures provided by Pope and Swenberg for the specific case of anthracene[12]. In that system the electronic polarization reorganization time is ~2 x 10^{-16}s, the lattice reorganization time is ~10^{-16} to 10^{-14}s, and the charge carrier residence time is ~10^{-14} to 10^{-13}s. Although there is some conflict in these figures, it is clear that the carrier residence time for inorganic semiconductors is so small the various polarization effects do not have as large an effect on carrier transport as is the case in organic semiconductors, where polarization effects significantly affect the energy levels of charged versus uncharged molecules.

Band like transport where charge carriers travel as delocalized Bloch-waves in the lattice can occur if the carrier "residence time" on a molecule is less than the lattice reorganization time, which can occur at low temperatures in organic semiconductors[13]. As temperature increases the delocalized Bloch waves of charge carriers in the lattice are

increasingly scattered by phonons, causing mobility to fall. If the mobility falls enough to allow the charge carrier to fall into the potential well of its own lattice distortion, the charge carrier will become localized and charge transport will become polaronic in nature. In that case the charge carrier can only move if it is able to tunnel (or in the parlance of the organic semiconducting community, "hop") to a neighboring lattice site with an appropriate energy level, a process which is critically dependent on lattice vibration and dynamic disorder in the lattice in general. Therefore increased lattice vibration will result in a higher probability of a successful tunneling event, so that charge carrier transport in this regime is a thermally activated process. In that case, $\mu \ll 1 \frac{cm^2}{Vs}$, and $\mu \propto e^{-E/k_B T}$, where E is the magnitude of the electric field[12].

Because polarization effects are so important in the polaronic charge transport regime where charge carriers are so localized, an alternative formulation that may be used is Marcus's electron transfer (ET) theory, which was originally developed to describe the electron transfer between a donor and acceptor molecule in solution[14]:

$$D + A \rightarrow D^+ + A^- . \tag{1.11}$$

In order for a polaron to hop from one molecule to another, the molecular orientation of the initial and final states need to first reach a common configuration with an equal amount of molecular distortion at both sites. Therefore an ET reaction requires that a reorganization energy of the conformation of the two molecules, λ, be overcome, even in a perfect organic crystal. This reaction is usually represented graphically be two parabolic energies: V_R (the energy of the two reactants), and V_P (the energies of the two

products) along a generalized spatial coordinate, q. This is illustrated below in Figure 1.7.

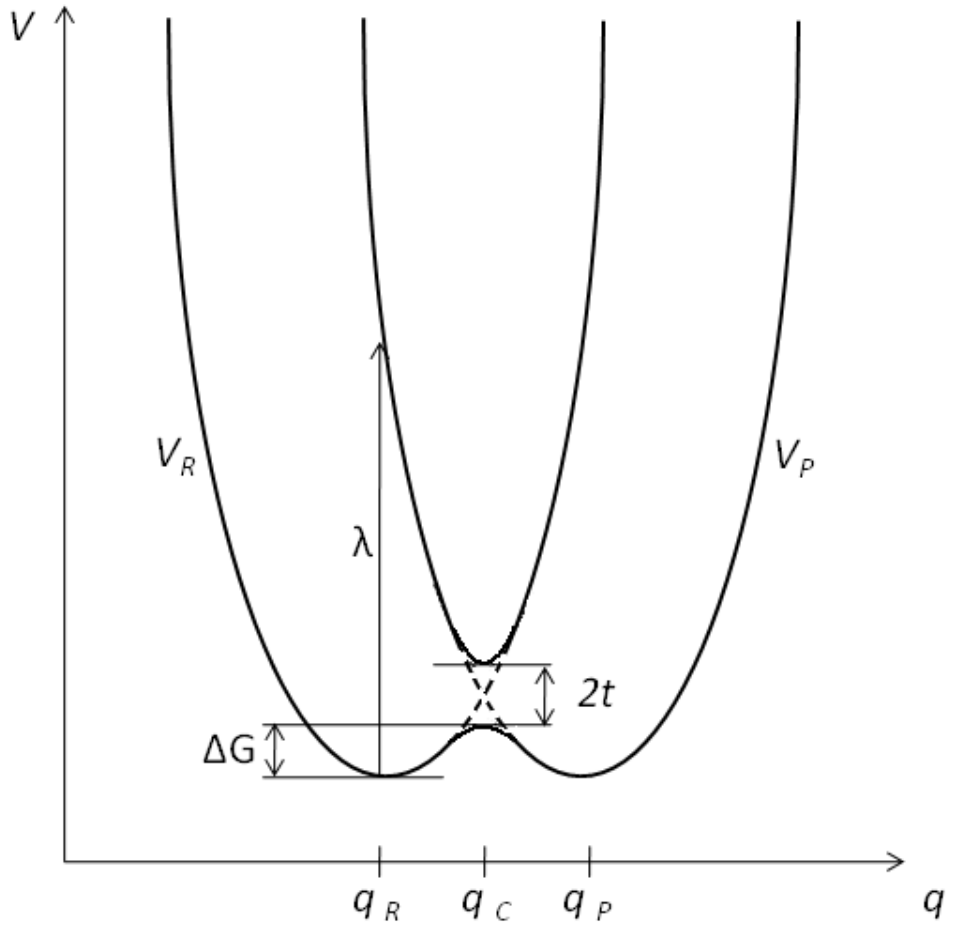

Figure 1.7: Graphical representation of the two parabolic potential energy curves of an Electron Transfer (ET) reaction. Here V_R is the energy curve of the two reactant molecules, V_P is the energy curve of the two product molecules, q is a generalized coordinate, t is the transfer integral, ΔG is the energy barrier height, and λ is the reorganization energy.

In the ET theory represented in Figure 1.7, the electron transfer is faster than the molecular reorganization, and so the reaction is nonadiabatic. Under those circumstances the reaction consists of a vertical transfer from the energetic minimum of V_R to the V_P

energy curve, followed by a relaxation along the spatial coordinate q to the energetic minimum of V_P. The equations describing V_P and V_R are:

$$V_R = \frac{p}{2}(q - q_R)^2$$
$$V_P = \frac{p}{2}(q - q_p)^2 \quad (1.12)$$

and the reorganization energy, λ, first introduced by Marcus in his electron transfer theory[14,15], is:

$$\lambda = \frac{f}{2}\ q_R - q_P)^2, \quad (1.13)$$

Where f is the reduced force constant for the parabolas[16]. If we define the transfer integral, t, to be the quantity shown in Figure 1.7, which physically represents the degree of overlap between the π orbital wave functions of neighboring molecules, than the barrier height of the reaction, ΔG, is given by:

$$\Delta G = \frac{(\lambda - 2t)^2}{4\lambda} \cong \frac{\lambda}{4} - t, \quad t < \lambda \quad (1.14)$$

Using a semiclassical approach Marcus derives an electron transfer rate based on a simple Arrhenius temperature dependent behavior that takes into account electron tunneling at low temperature[14]:

$$k_{ET} = \frac{2\pi}{\hbar}\frac{t^2}{\sqrt{4\pi\lambda k_B T}}\exp\left[-\frac{\lambda/4 - t}{k_B T}\right] \quad (1.15)$$

where $\hbar$ is Plank's constant, k_B is the Boltzmann constant, and T is the temperature in Kelvin. The mobility is connected to the electron transfer rate via the expression:

$$\mu = \frac{qa^2}{k_B T} k_{ET} \tag{1.16}$$

where a is the lattice constant of the molecular crystal. In general band-like transport is expected if $2t > \lambda$, while temperature-activated localized transport is expected if $2t < \lambda$. As the transfer integral, t, is related to the carrier residence time on a molecule, τ_{RES}, and the reorganization energy, λ, is related to the molecular polarization time, τ_{MP}, the inequalities stated above are equivalent to stating that bandlike transport is expected if $\tau_{RES} < \tau_{MP}$, and that temperature-activated localized transport is expected if $\tau_{RES} > \tau_{MP}$[4].

Temperature-activated localized transport has generally been referred to as "hopping transport" in the literature, of which many competing models have been developed, based on varying physical models and assumptions. The most noteworthy is the Gaussian Disorder Model (GDM) proposed by Bassler[17-19]. Because the optical absorption spectra of the materials modeled by the GDM have a Gaussian distribution, the energetic sites that can be occupied by charge carriers in a disordered solid are assumed to have a Gaussian Density of States (DOS) energetic distribution:

$$\rho(E) = \left(2\pi\sigma^2\right)^{-1/2} \exp\left(\frac{-\varepsilon^2}{2\sigma^2}\right) \tag{1.17}$$

where the energy, ε, is measured relative to the center of the DOS, and σ is the standard deviation of the distribution. The hopping rate from site to site is assumed to take on a Miller-Abrahams form:

$$\nu_{ij} = \nu_0 \exp\left(-2\gamma R_{ij}\right)\begin{cases}\exp\left\{-\left(\varepsilon_j - \varepsilon_i\right)/\left(k_B T\right)\right\}, & \varepsilon_j > \varepsilon_i \\ 1, & \varepsilon_j < \varepsilon_i\end{cases} \qquad (1.18)$$

where R_{ij} is the intersite hopping distance, ε_i is the energy of site i, and 2γ is an overlap parameter that allows that allows geometric disorder to be taken into account by subjecting that parameter to a Gaussian distribution with a standard distribution Σ. This allows thermal (random) variations in molecular position and orientation to be included in the GDM[19].

Using the model described above in Monte Carlo simulations, Bässler was able to show that the mobility takes on the form:

$$\mu = \mu_0 \exp\left[-\left(\frac{2}{3}\frac{\sigma}{k_B T}\right)^2\right]\exp\left\{C\left[\left(\frac{\sigma}{k_B T}\right)^2 - \Sigma^2\right]\sqrt{E}\right\} \qquad (1.19)$$

where E is the magnitude of the electric field and C is an empirical constant. In general, charge carrier mobility is said to exhibit a Poole-Frenkel dependence on the electric field when $\mu \propto \sqrt{E}$. In his Monte Carlo simulations Bässler also showed that an injected carrier hopping through a DOS with a standard deviation of σ relaxes to an equilibrium energy at a distance of

$$\left\langle \varepsilon_\infty \right\rangle = \frac{-\sigma^2}{k_B T} \qquad (1.20)$$

below the center of the DOS. Nobikov and others later expanded on Bässler's work, performing Monte Carlo simulations of 3D correlated disorder model of charge transport in disordered organic semiconductors that included charge-dipole interactions[20]. From

their work they proposed the following empirically based expression describing charge carrier mobilities in these systems:

$$\mu = \mu_0 \exp\left[-\left(\frac{3\sigma}{5k_B T} \right) + 0.78\left(\left(\frac{\sigma}{k_B T} \right)^{3/2} - 2 \right) \sqrt{\frac{eaE}{\sigma}} \right] \qquad (1.21)$$

where σ is the width of the Gaussian DOS used in the simulation.

1.4: TIME OF FLIGHT STUDIES OF BAND LIKE TRANSPORT IN SINGLE CRYSTAL ORGANIC SEMICONDUCTORS

Time of flight studies are typically carried out on single crystals with thicknesses on the order of 100 μm to 1000 μm. A diode is usually constructed by placing the organic crystals between two metals, at least one of which is typically a transparent conducting oxide, and a constant bias is applied between the two electrodes. A key requirement is that the organic semiconducting layer has a sufficiently low dark conductivity (or equivalently a sufficiently long dielectric relaxation time). A sharp light pulse at a wavelength with a large extinction coefficient in the semiconductor and a pulse width much less than transit time of photogenerated charges across the sample is applied to the semitransparent contact, creating a sheet of photogenerated bound electron-hole pairs (excitons) in the semiconductor near one end of the sample.

Excitons are typically formed in organic semiconductors for a few reasons. Here by "exciton" we mean a bound electron and hole on the same molecular unit (either a single molecule or a segment of a polymer chain over which charges are delocalized) that

are in the same Coulombic potential well. Other types of bound electron-hole excitations can, and do, occur. Excimers are bound electron-hole pairs where the electron and hole reside on identical neighboring molecules. An exciplex is a bound electron-hole pair where the electron and hole reside on neighboring donor and acceptor molecules or polymeric segments with distinct HOMO and LUMO energetic levels[12].

Excitons, and the other species of bound states mentioned above, form in organic semiconductors for a few reasons. First, the natural amount of disorder in the materials results in electron wave functions that are much more localized than they are in inorganic crystalline metals or semiconductors. Second, the low dielectric constant in these materials ($\varepsilon_r \sim 3$) means that Coulombic forces are not screened effectively. The result is typical excitonic binding energies on the order of 300-500 meV[21], much larger than $k_B T$ (~25 meV at room temperature). In order for excitons in organic materials to disassociate, they typically have to diffuse to a semiconductor/metal or semiconductor/semiconductor heterojunction with one or both energy level offsets greater than the exciton binding energy[22].

Therefore, in a TOF experiment, only those excitons are able to disassociate at the semitransparent metal/semiconductor junction result in a sheet of free charge carriers that can travel the length of the device. If the number of charge carriers generated is small enough that the field distortions in the device is undistorted by those mobile charges, they travel the length of the sample with a constant average drift velocity, v. When the sheet of charges reaches the opposite contact the signal is observed and the transit time is

recorded. Because the charge carrier mobility is related to the electric field by the following relation:

$$\mu_{perp} = \frac{v_{perp}}{|\vec{E}|} = \frac{L^2}{\tau V} \tag{1.22}$$

where the "*perp*" subscript indicates direction the charge carriers are moving for this particular measurement, L is the thickness of the device, τ is the transit time of charge carriers across the device, and V is the voltage across the device. A typical schematic of a TOF experiment is shown in Figure 1.8.

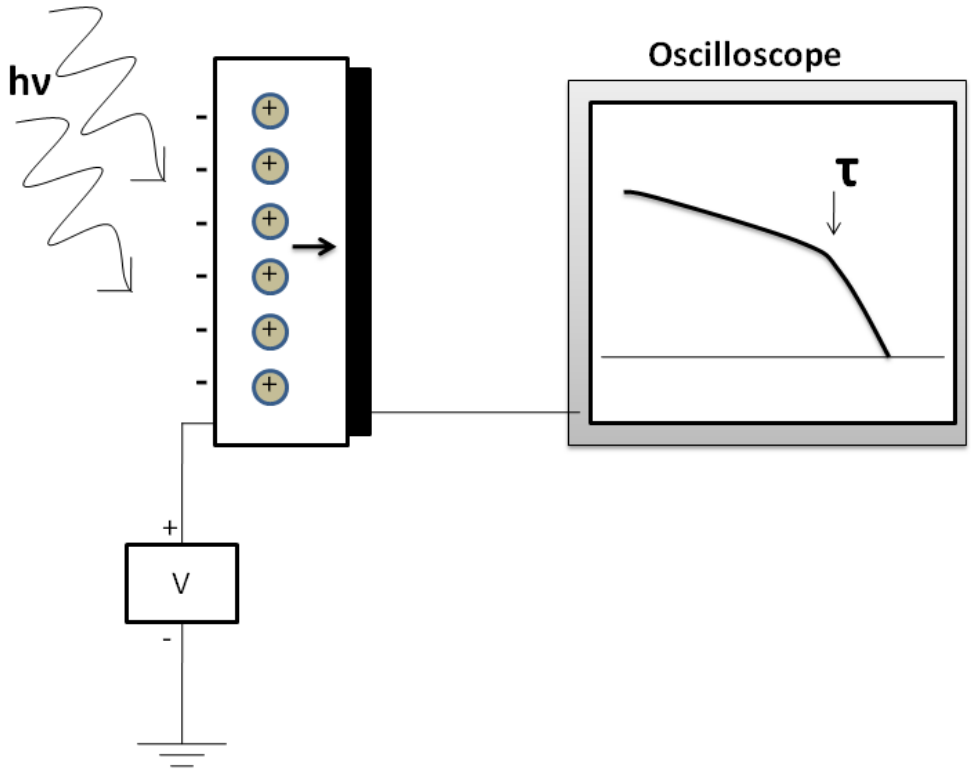

Figure 1.8: Typical schematic of a Time of Flight (TOF) experiment measuring the mobility of charge carriers in an organic semiconducting crystal with a thickness on the order of 100 to 1000 μm.

The experimental TOF mobility data shown below in Figure 1.9 produced by Karl and his coworkers demonstrates clear evidence of band-like transport in the *a*-direction of a highly purified single crystal of naphthalene. The magnitude of both the hole and electron mobilities reaches extremely high values for organic semiconductors, especially at low temperatures. Also evident is the inverse power low dependence of both hole and electron mobilities: $\mu \propto T^n \ \ (n < -1)$, and a marked dependence of the hole mobilities on electric field below about 40 K.

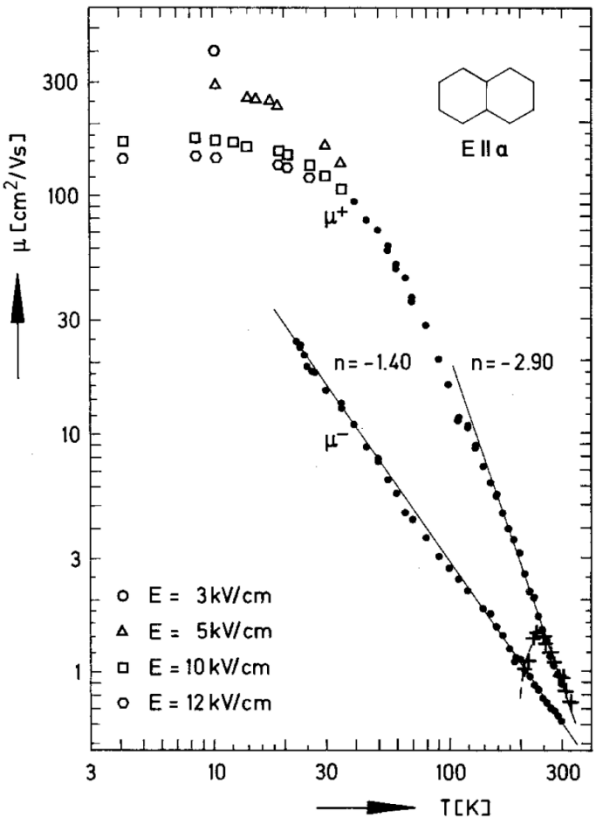

Figure 1.9: Experimental Low temperature TOF mobility data for holes and electrons in the *a* crystallographic direction. Both hole and electron mobilities exhibit the hallmark of band like transport: an inverse power low dependence of the mobility on temperature ($\mu \propto T^n$, where the value of *n* is indicated in the figure above). Figure reproduced with kind permission of Springer Science+Business Media from "Ultrapure, High Mobility Organic Photoconductors" by W. Warta, R. Stehle, and N. Karl. Appl. Phys. A., **36**,163-170.

It turns out that at low fields the Schottky model of acoustic deformation potential scattering of hot charge carriers can be used to accurately describe the dependence of velocity (and therefore mobility) on electric field. This model assumes a charge carrier gas that that exists in a band with a width that is at least several multiples of k_BT which is "heated" by absorbing energy from an applied electric field[10]. The expression Schottky derived for the velocity of charges in that model is

$$v(E) = \frac{\mu_0 \sqrt{2}}{\left\{1 + \left[1 + \frac{3\pi}{8}\left[\frac{\mu_0 E}{u_L}\right]^2\right]^{1/2}\right\}^{1/2}} \cdot E \qquad (1.23)$$

where μ_0 is the zero field mobility, u_L is the speed of sound in the semiconductor, and E is the magnitude of the electric field.

Figure 1.10 shows the electric field dependence of holes in naphthalene, again in the crystallographic *a* direction. Note the deviation of the mobility from the behavior predicted by equation (1.23). This is due to velocity saturation of charge carriers in the crystal. The higher the mobility of charge carriers in the crystal, the faster they move under the influence of a given electric field. Even at low temperatures, there are still lattice vibrations (phonons) present in the crystal that can scatter the delocalized Bloch wave functions of the travelling charge carriers. As the magnitude of the applied electric field increases, the charge carrier velocity increases until it is dominated by these scattering processes.

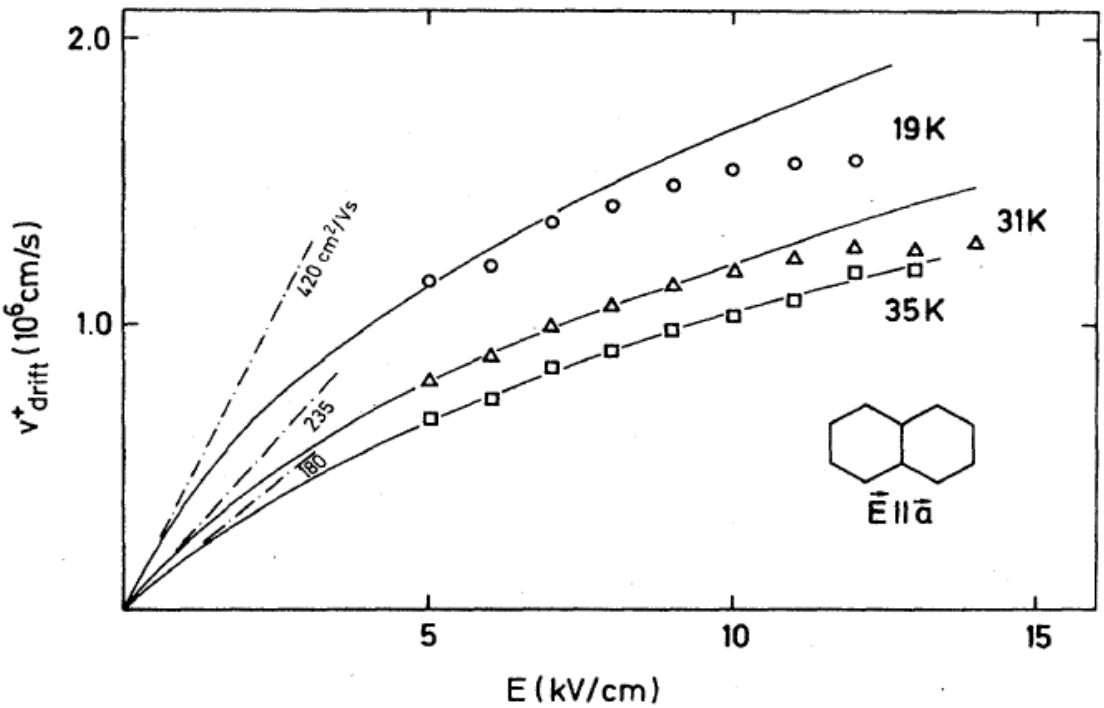

Figure 1.10: Hole drift velocity in the crystallographic *a* direction plotted as a function of electric field at temperatures of 19, 31, and 35 K. Note the deviation from equation (1.23) at high fields due to velocity saturation from phonon scattering. Reprinted from "Hot Holes in Naphthalene: High Electric-Field-Dependent Mobilities" by W. Warta and N. Karl. Phys. Rev. B. Vol. 32, No.2. p. 1172 (1985). Copyright (1985) by the American Physical Society.

In this chapter we have provided an introduction to the physics of charge transport in well ordered organic semiconductors. In the next chapter we move into the field which has the most direct applicability to the work of this dissertation: Organic Field Effect Transistors.

Chapter 2: Introduction to OFETs: Standard Measurements and the Pulsed Transient "Time of Flight" Method

2.1: BACKGROUND

A transistor is a three terminal device that is basically a capacitor where one plate is a conducting channel in a semiconductor between two ohmic contacts[23]. The Field Effect Transistor was first proposed by Lilienfeld in 1926 (although his patent was not granted until 1930)[24], and it wasn't until 1947 that Bardeen and Brattain working under Shockley actually demonstrated the first working semiconductor-based transistor[25]. Silicon transistors are, of course, now ubiquitous in modern life.

Organic Field Effect Transistors (OFETs) work on a principle analogous to accumulation mode inorganic transistors: through the application of a voltage to the gate contact, an accumulation layer of charge is induced in the organic semiconducting active layer. As the charge density in the semiconductor increases, the channel conductivity increases dramatically, and charges can flow between the source and drain contacts. A schematic of an OFET is shown in Figure 2.1.

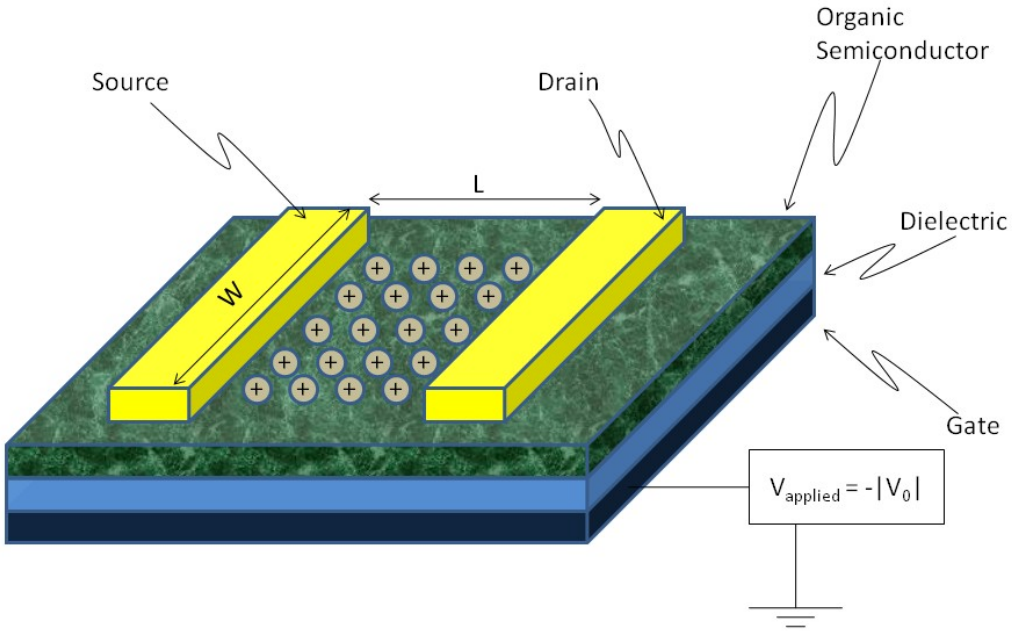

Figure 2.1: A schematic of a basic top-contact OFET. The gate is typically heavily doped Silicon, the dielectric is typically SiO_2, and typical organic semiconductors used in OFETs are pentacene or poly(3-hexylthiophene-2,5-diyl). Here the "top contact" configuration is shown in which the (Au) source and drain contacts are vacuum deposited directly onto the organic semiconductors, as opposed to "bottom contact" devices, in which the source and drain contacts are buried beneath the semiconductor. Note the applied negative voltage to the gate dielectric and the induced positive channel of accumulated charge between the source and drain contacts.

In general it is possible to model the steady state drain current of an OFET using the following expressions:

$$I_d = \begin{cases} \mu_{eff} C_{INS} \dfrac{W}{L}\left(V_{gs} - V_t\right) \cdot V_{ds}, & V_{ds} < V_{gs} - V_t \\ \mu_{eff} C_{INS} \dfrac{W}{2L}\left(V_{gs} - V_t\right)^2, & V_{ds} > V_{gs} - V \end{cases} \qquad (2.1)$$

Where I_d is the drain current, μ_{eff} is the effective mobility, W is the channel width, L is the channel length (both indicated schematically in Figure 2.1), C_{INS} is the capacitance of the gate dielectric, $V_{gs} = V_{gate} - V_{source}$, $V_{ds} = V_{drain} - V_{source}$, and V_t is

the threshold voltage of the device, which is the gate voltage at which charge conduction becomes possible across the channel. There are two major regimes of device operation, the linear regime (which occurs when $V_{ds} < V_{gs} - V_t$), where the drain current increases linearly with increasing V_{ds} and for which V_{ds} drops linearly across the channel between the source and the drain, and the saturation regime (which occurs when $V_{ds} > V_{gs} - V_t$), where the drain current is independent of the applied V_{ds}, and for which V_{ds} drops linearly from the drain contact to some point in the channel, known as the pinch-off point, beyond which V_{ds} changes sign and there is no charge accumulation region.

The lower portion of Figure 2.2 shows a an I_d-V_{ds} plot of typical organic transistor with an active layer of sublimed pentacene, a heavily doped Si gate, a gate dielectric of 1030 Å of SiO_2, and Au source and drain contacts with a channel length and width of 50 μm and 500 μm, respectively. In this measurement the gate voltage is held constant while V_{ds} is swept from zero to some maximum value, and I_d is recorded. This measurement is repeated for various gate voltages above and below the threshold voltage. The approximate crossover from the linear regime at low V_{ds} to the saturation regime at higher V_{ds} is indicated by the dashed curved line, and the diagrams above and below the plot show the behavior of the accumulation channel in both regimes.

In the linear regime V_{gs} is much larger than V_{ds}, so the voltage at the source and drain should be very similar, and the charge carrier density should therefore be nearly uniform across the channel. In the saturation regime V_{ds} should be much larger than V_{gs}, so that at the drain the voltage should be nearly zero (or even the opposite polarity of V_{gs}), and therefore the charge carrier density at the drain should be nearly zero. Note

here that the thickness in the vertical direction of the drawn channel is meant to indicate charge carrier density.

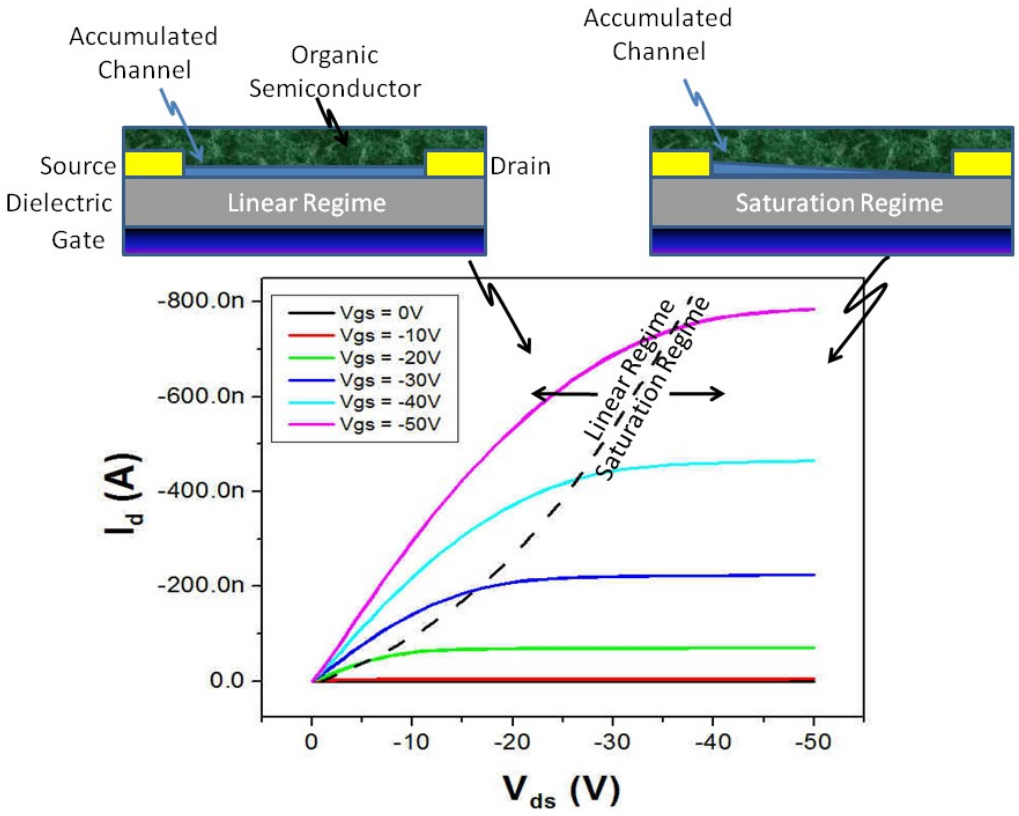

Figure 2.2: A typical I_d-V_{ds} plot of an OFET where the transition between the linear and saturation regimes at various gate voltages is indicated by the dashed line. The schematics of the OFET above the plot give the relative charge carrier concentration distributions of the channel in the linear and saturation regimes. Note that the vertical thickness of the indicated channel corresponds to charge carrier concentration.

Although much work has been focused on single-crystal OFETs[26,27], the work in this dissertation has focused on sublimed polycrystalline films of small molecule organic semiconductors, where charge transport is dominated by the structural disorder of the film. In these films an extremely useful model which has been devised to model charge transport is the Multiple Trap and Release (MTR) model[28], which applies to well ordered

films where thermally activated charge transport is observed such as sublimed thin films of pentacene and sexithiophene. The basic assumption is that there exists in the DOS two distinct regions: a region of facile transport, above which charges can move easily with a high mobility, a region of discrete trapping states due to disorder in the system, and a "band-edge" separating the two. As charge carriers move through the system in the high mobility states, they encounter discrete trapping states below the band edge and are only released when thermally activated[4]. Experiments on pentacene and sexithiophene OFETs with a single grain boundary in the channel have shown that transport across the grain boundary is indeed thermally activated[29,30]. The mobility of charge carriers in the MTR model is given by:

$$\mu_{eff} = \mu_0 \alpha \exp\left(-\frac{E_C - E_t}{k_B T}\right) \tag{2.2}$$

where μ_0 is the mobility in the absence of trapping effects, E_c is the energy of the band edge, E_t is the characteristic energy of the distribution of trap states, and α is a proportionality constant related to the ratio of free charge carriers and trapped charge carriers at the band edge. The most common trap distribution used in the MTR model is an exponential "band tail" of trapping states descending from the band edge. This concept is illustrated in Figure 2.3. Note that because charge carriers are released from trapped states via thermal activation, and applying a gate voltage brings the Fermi energy of the charge carrier distribution closer to the band edge, the effective mobility is dependent on the applied gate voltage (*i.e.*, the charge carrier concentration).

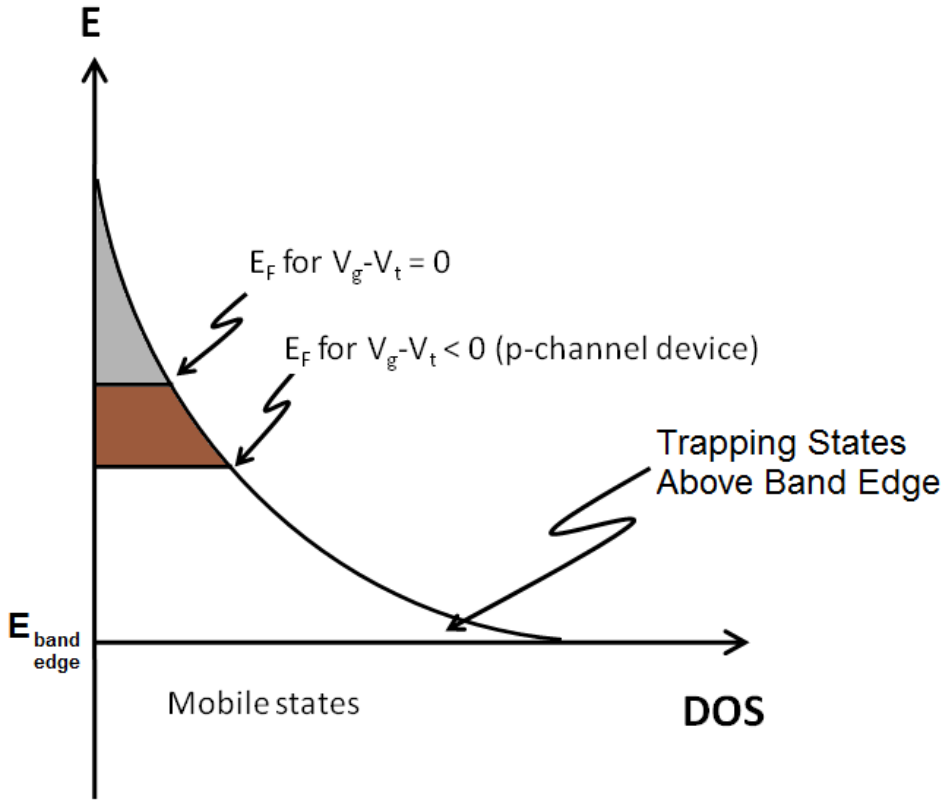

Figure 2.3: Multiple Trapping and Release DOS illustration for a polycrystalline thin film showing an exponential tail of trapping states descending from the band edge for a p-channel device. Also indicated are the Fermi energies of the hole distribution for $V_g - V_t = 0$, and for $V_g - V_t < 0$. Because charge carriers are released from trapped states via thermal activation, mobility increases with applied gate voltage.

Equation 1.21 accurately describes mobilities in devices with low charge carrier concentrations (10^{14}-10^{15} cm^{-3}), but not in situations where charge carrier densities approach those known to occur in OFETs under operation (~10^{19} cm^{-3}). Vissenberg and Matters proposed a Variable Range Hopping (VRH) model of charge carrier percolation in disordered materials that yielded the following charge carrier density-dependent expression for the field-effect mobility[31]:

$$\mu_{FE} = \frac{\sigma_0}{e}\left(\frac{\left(\frac{T_0}{T}\right)^4 \sin\left(\pi\frac{T_0}{T}\right)}{(2\alpha)^3 B_C}\right) p^{\frac{T_0}{T}-1} \qquad (2.3)$$

where p is the charge carrier density, σ_0 is the prefactor of the conductivity, T_0 is a measure of the width of the exponential DOS in the model, α^{-1} is the effective overlap parameter between localized states, and B_C is the critical number for the onset of percolation. This model has successfully been used to unify the largely varying the charge carrier mobilities observed in OFETs and organic diodes fabricated from the same organic semiconductors by Tanase and her coworkers[32].

2.2: PULSED TRANSIENT VOLTAGE MEASUREMENTS

As we have shown in previous work[33], and as Dost *et. al.* have shown recently[34], the application of a square wave voltage pulse to the source contact of an OFET produces a current at the drain contact after a delay τ which is inversely proportional to the charge carrier mobility in the device. We had previously hypothesized that the holes (for a p-channel device) injected at the source by a voltage pulse with an infinitesimally small rise time were transported across the channel by an electric field of magnitude V_{ds}/L, and that given this simplistic picture μ would be given by

$$\mu = \frac{L^2}{\tau V_{ds}} \qquad (2.4)$$

However if one examines the Electric field distribution of an OFET undergoing our pulsed TOF experiment, with a channel length of 7.5 μm and a gate dielectric thickness of 300 nm where the drain and gate are both approximately grounded and a voltage pulse of 50 V is applied to the source contact, it can easily be seen that the magnitude of the lateral electric field between the source and drain ($E_{\parallel}$) is 6.67x10^4 V/cm, while the magnitude of the perpendicular electric field between the source and the gate ($E_{\perp}$) is 1.67x10^6 V/cm. Therefore the first holes which are injected at the source are effectively immobilized at the organic/dielectric interface immediately adjacent to the source contact, and subsequent holes which are injected similarly serve to build up an accumulation region near the source contact. This process continues until there are enough charges at the organic/dielectric interface in the neighborhood of the source to effectively shield injected holes from $E_{\perp}$. At this point mobile charges with an energy ε_0 hop into a region of the organic semiconductor (driven by $E_{\parallel}$) where the states with lower energy are largely unoccupied. Charge carriers under these circumstances are now subject to two competing processes: trapping (*i.e.*, contribution to the channel formation process), to which we assign a characteristic carrier residence time of τ_{trap}, and hopping (*i.e.*, lateral transport), to which we assign a characteristic time of τ_{mobile}.

Recent electric-field-dependent charge transport studies of pentacene OFETs of varying channel lengths in our group[35] have shown that at room temperature electric field dependent dependence of the field-effect (FE) mobility of a pentacene OFET does follow a Poole-Frenkel dependence:

$$\mu = \mu_0 \exp\left(\frac{\beta\sqrt{|\vec{E}|}}{k_B T}\right) \tag{2.5}$$

and β is a field dependent coefficient originally proposed by Gill in an empirical relation describing charge transport in charge-transfer complexes[36]. However the electric field dependence on the mobility was found to be more pronounced at high fields ($\sim 10^6\ V/cm$) and at very low temperatures.

In Chapter 3 we present data which suggest that over the range of lateral electric fields applied in this work ($2.5x10^4 \frac{V}{cm} \lesssim |E_{\parallel}| \lesssim 1x10^5\ \frac{V}{cm}$), the primary variable responsible for changes in both the μ_{FE} and $\mu_{dynamic}$ is the charge carrier density, p, and therefore indirectly the effective gate voltage (V_{gs}-V_t). This agrees with the work of Vissenberg and Matters[31], who derived the density dependent expression for the FE mobility in an OFET given in equation (2.3). Our findings of density dependent transient mobility measurements are also compatible with work by Tanase *et. al.*, who explain variations in μ_{FE} of approximately 3 orders of magnitude between space charge limited current (SCLC) measurements in organic diodes and FE μ measurements in OFETs fabricated from the same organic semiconductors (poly(3-hexyl thiophene) and a poly phenylene vinylene derivative) by the widely varying charge carrier densities that are induced by the two techniques[32].

The origin of V_t in OFETs is thought to be due to the existence of deep trapping states in the semiconductor that must first be filled in order for charge transport to occur. At applied gate voltages where $|V_G| < |V_T|$, very little charge transport is possible

because all of the charges accumulated in are very likely to fall into deep trapping states. We have argued above and present data below which supports the conclusion that over the range of $E_{\|}$ explored in this work, the charge carrier density excited at the source/organic interface is the determining factor which dictates τ. Therefore the quantity of interest which relates τ and L to μ is not V_{ds}, but is instead V_{gs}-V_t, which is the voltage responsible for generating the accumulation region in the channel. We note here that Dost *et. al.* have arrived at this result independently by plotting $1/\tau$ as a function of the magnitude of V_s (equivalent to our notation of V_{gs}), and noting that $\frac{1}{\tau} \rightarrow 0$ (that is, $\tau \rightarrow \infty$) as $V_s = \rightarrow V_t$[34].

To our knowledge the first person to mathematically formalize the response of a FET to a large voltage pulse applied to the source was J. R. Burns in 1969[37], who in his seminal work concentrated on the transient response of Si FETs. Burns took a transmission line approach by dividing the channel into N segments, each with a corresponding resistance (serially connecting each channel segment) and capacitance (between each section of the channel and the gate). This model approximates a device with a charge carrier density-dependent mobility and distribution of trapping states below the mobile states that allow charge transport. Therefore the model reproduces the response of an actual OFET to a voltage step applied to the source because mobile charges in channel segment i must first charge the i^{th} capacitor before they can move through the i^{th} resistor to channel segment $i+1$. A variation of the RC network which includes source and drain contact resistances, as well as a load resistor at the drain contact, is shown below in Figure 2.4.

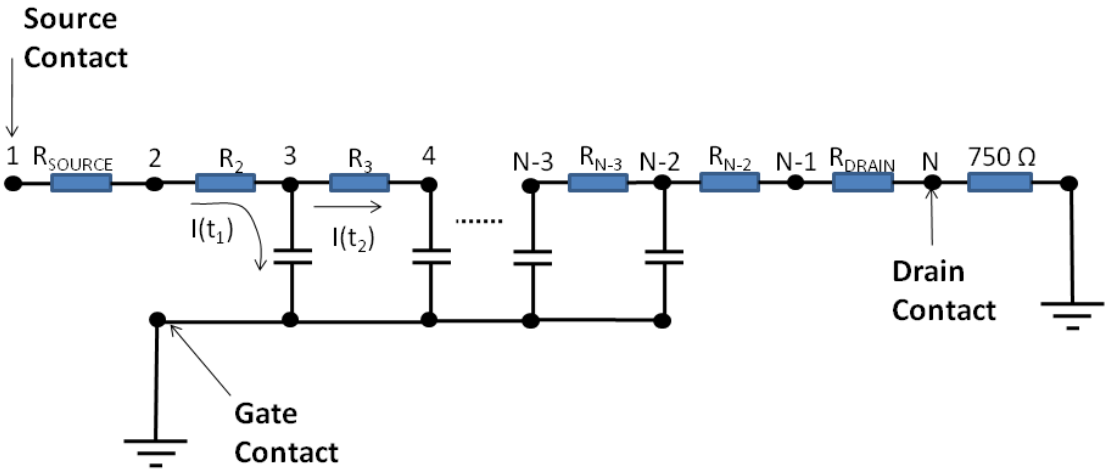

Figure 2.4: Distributed RC network used to model the behavior of the OFET to a large square wave voltage pulse at the source. R_{SOURCE} and R_{DRAIN} are the source and drain contact resistances, respectively. The value of each capacitor was taken to be the dielectric capacitance per unit length in the channel.

Pesavento *et. al.* have shown that typical normalized contact resistance values for bottom contact Au/pentacene OFETs are on the order of $5x10^4$ Ω-cm[38]. For a 2000 µm channel the estimated contact resistances for both the source and drain contacts using this value would be 250 kΩ. However, simulations carried out in our group have shown that the estimated contact resistances for a device with those dimensions at high gate voltages to be as low as ~70 kΩ. The source and drain contact resistances in Figure 2.4 were calculated by using this figure for the source and drain contact resistances.

Using the transmission line approach described above to simulate the channel, the time evolution of the voltage (and therefore current) in the channel is given by[37]:

$$\frac{\partial}{\partial x}\left[\frac{\mu}{2}\frac{\partial}{\partial x}[\bar{V}(x,t)]^2\right] = \frac{\partial}{\partial t}[\bar{V}(x,t)] \qquad (2.6)$$

where $\bar{V}(x,t) = V_{gs} - V_t - V(x,t)$, and μ is the effective mobility of charge carriers (in this case holes) in the channel. Using a finite difference approach to create a discrete

version of equation (2.6), and a custom MATLAB program to numerically solve for $\bar{V}(x,t)$ (and therefore the charge density and current in the channel), we are able to visualize the evolution of the voltage and current across the channel as a function of time. The program is included as an appendix to this dissertation.

In order to compare the simulation to experimental data, we chose a channel length of 7.5 µm, a source voltage pulse magnitude of ~20 V (with no threshold voltage). The simulated time evolution of the voltage (which is proportional to the charge density) across the channel shown is shown in Figure 2.5.

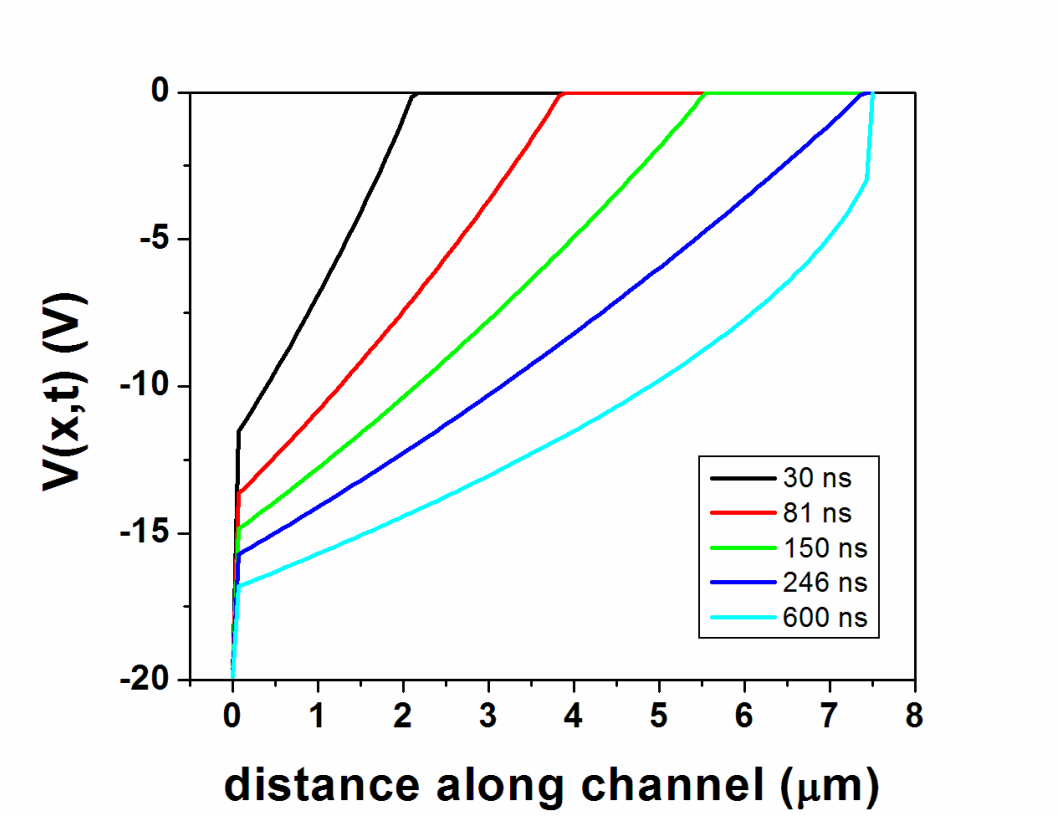

Figure 2.5: Simulated evolution of the voltage (proportional to the charge density) across the channel as a function of distance across the source contact and time. Note the voltage drops at the source and drain contacts (at 0 and 7.5 µm, respectively) due to the contact resistance at the metal/semiconductor heterojunction.

From this figure it is obvious that the OFET pulsed transient measurement is not producing a true single wave of charge carriers which move across the channel. Instead, the turn-on time is a measure of the dynamic channel formation process. Near the source contact, but in the channel, the voltage with respect to ground at long times differs from the applied source voltage pulse magnitude only by the value of the voltage drop across the metal/semiconductor heterojunction. The voltage at the drain contact differs from zero only by the voltage drop across the 750 Ω load resistor.

The current across the channel as a function of distance from the source contact and time is shown in Figure 2.6. Note at long times, as expected, the current is uniform everywhere in the channel.

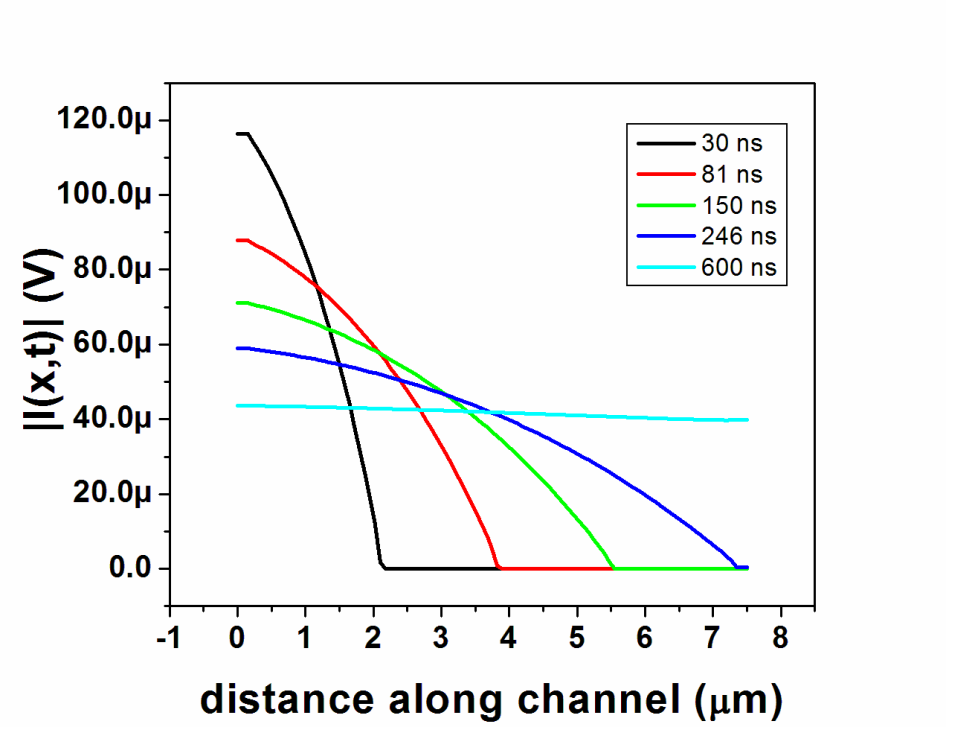

Figure 2.6: Simulated evolution of the current across the channel as a function of distance across the source contact and time.

Burns showed analytically that the effective mobility of the charges in the channel may be extracted from the turn-on time using the following expression:

$$\mu_{dynamic} = 0.38 \frac{L^2}{\tau\left(V_{gs} - V_t\right)} \tag{2.7}$$

where the prefactor of 0.38 reflects the process of channel formation as the channel evolves. By recording the current at the drain at each time step in our MATLAB simulation, we are able to reproduce the types of drain current vs. time plots that we record during our transient measurements. The results are shown below in Figure 2.7. The experimental data was taken at 300 K for the transient response of a pentacene OFET with a threshold voltage of ~-13.9V, an applied source voltage pulse of ~33 V (so that Vgs-Vt was on the order of -20 V) and a mobility extracted from the transient experimental data using equation (2.7) of ~0.67 cm^2/Vs. The simulation was performed on an equivalent device. We can see that qualitatively there is a fairly good agreement between the experimental and simulated turn on times, but the simulated behavior of the drain current ramping from 0 to full scale is notably faster than the equivalent process in the actual device. We attribute this to the presence of charge trapping in the OFET channel that is not accurately simulated in the first-order simulation results shown in the figure. Also the charge carrier mobility in the simulation is charge carrier density-independent. Nevertheless, we believe that the simulation results provide a convincing picture of what is actually happening in the OFET channel during the pulsed voltage OFET TOF experiment.

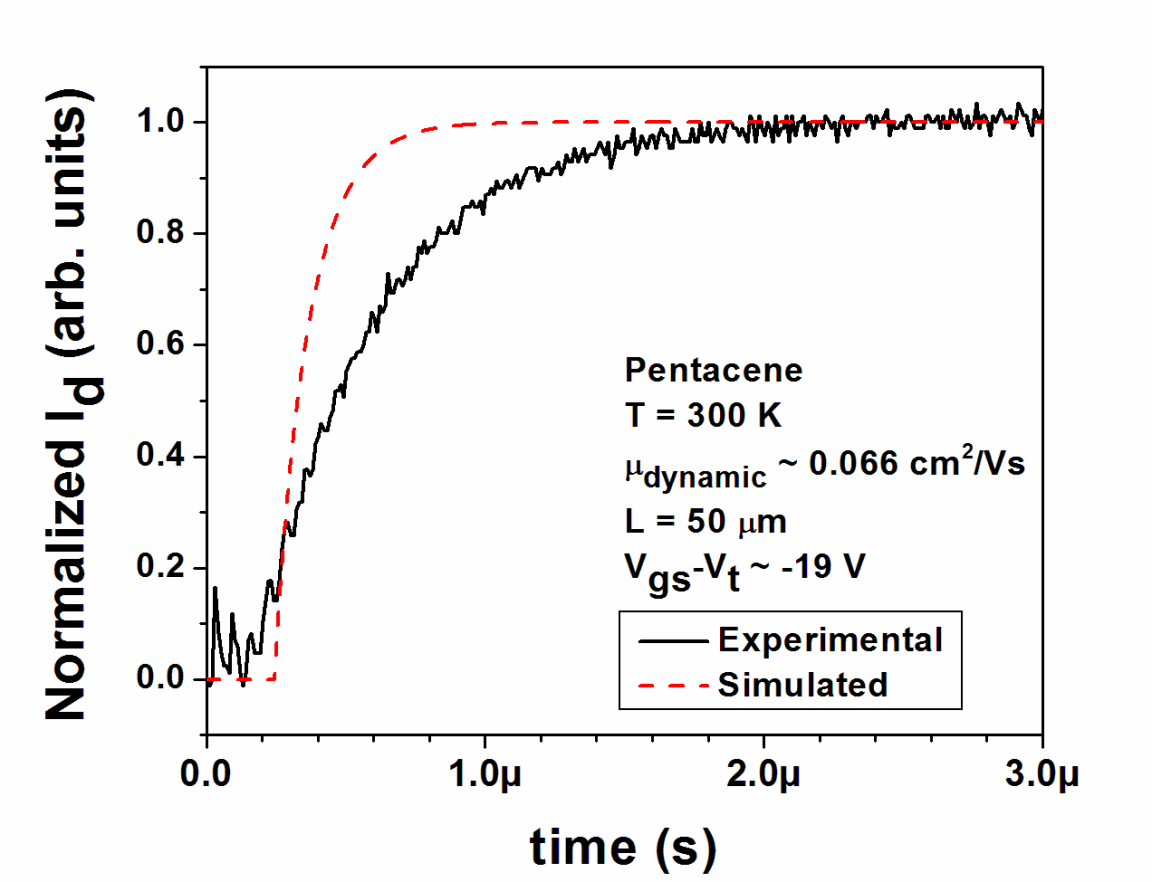

Figure 2.7: Typical experimental drain current transient (solid black line) as a function of time for a bottom contact pentacene OFET. The dashed red line shows the corresponding plot of the simulated results.

Chapter 3: Temperature Dependence of Transient Charge Transport Measurements in a Pentacene Based OFET

3.1: INTRODUCTION

Our work in this chapter focuses on the pulsed voltage transient technique previously introduced that can be used to extract mobilities that was first introduced by our group[33,39]. Since then the technique has been used by Dost *et. al.,* who have developed their own low-cost measurement circuit based on the technique[40] and applied it to extract mobilities from poly(triaryl amine) devices of varying channel length[34]. Here we extend our earlier work on transient mobility measurements in a pentacene based OFET to measurements at varying temperatures, directly extracting both transient mobilities and charge carrier velocities via the application of a sharp voltage pulse to the source contact and measuring the response of the OFET at the drain. We compare those extracted transient mobilities and velocities to the corresponding figures extracted from DC measurements and discuss the origins of discrepancies where they appear. We show that the dynamic mobilities extracted from the transient measurement ($\mu_{dynamic}$) correspond well with the DC field-effect mobilities (μ_{FE}) measured at varying temperatures, and exhibit a higher Activation Energy (E_a), which we discuss in terms of the Multiple Trap and Release (MTR) model. This leads to important insights into the nature of the transient pulse voltage measurement technique, as well as the physical significance of $\mu_{dynamic}$ at temperature between 117 K and 300 K.

3.2: EXPERIMENTAL DETAILS

Figure 3.1 below gives a circuit diagram illustrating the experimental setup used to make transient measurements.

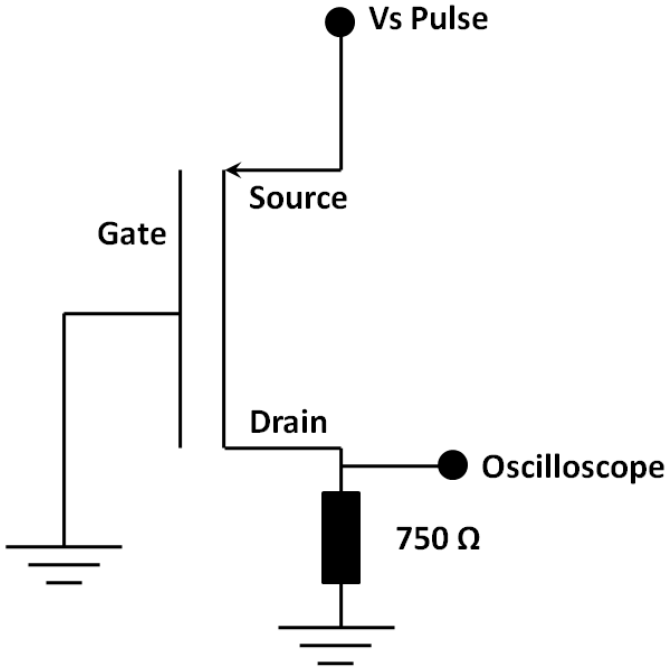

Figure 3.1: The circuit diagram used to perform the pulsed voltage transient mobility measurement.

The OFET gate was a heavily n-doped Si wafer which also served as the device substrate. The gate dielectric isolating the gate contact from the pentacene layer consisted of 200 nm of Si_3N_4 under 100 nm of SiO_2. The capacitance per unit area of a parallel plate capacitor is given by $C = \frac{\varepsilon_0 \varepsilon_r}{t}$, where t is the thickness of the dielectric, ε_0 is the permittivity of free space, ε_r is the relative permittivity of the dielectric. In the case of OFET structure investigated in this work, the two dielectric layers stacked on top of one another gave an effective capacitance, C_{eff}, given by the expression: $\frac{1}{C_{eff}} = \frac{1}{C_{SiO_2}} + \frac{1}{C_{Si_3N_4}}$, resulting in a value of C_{eff} of 16.9 nF/cm^2. Two interdigitated Au electrodes formed the

source and drain with a channel length and width of 7.5 μm and 2000 μm, respectively. It is well known that Silanes such as Octadecyltrichlorosilane (OTS) can chemically react with the OH groups on an SiO_2 surface to form a self-assembled monolayer (SAM) that is hydrophobic in nature and therefore amenable to deposition of most organic semiconductors, and that thiols can be used to chemically modify the surface of Au contacts to improve charge injection into organic semiconductors[41]. Therefore prior to the deposition of pentacene, the SiO_2 surface was treated with a 10 mM solution of dissolved in toluene for 50 m, and the Au contacts were treated with a 10 mM solution of nitrobenzenethiol dissolved in acetonitrile for 1 hour[33]. The pentacene (obtained from Sigma-Aldrich) was first purified via vacuum sublimation, and then sublimed from a thermal boat in a vacuum better than $4x10^{-7}$ torr at 0.3 Å/s for the first 50 Å, and then at a rate of 1 Å/s for the remaining approximately 400 Å.

Temperature dependent measurements were carried in a desert cryogenics cryo-probe station in a vacuum better than $3x10^{-3}$ torr. Care was taken to ensure thermal equilibrium between the OFET and the cooled chuck of the probe station by using Apiezon N Cryogenic High Vacuum Thermal Grease (purchased from Desert Cryogenics) to secure the OFET to the probe station chuck. After heating or cooling the OFET from one temperature to the next, care was taken to ensure that the device had reached thermal equilibrium with its surroundings before proceedings with testing. Following these procedures, both transient TOF measurements and DC I_d-V_{ds} and I_d-V_{gs} measurements (made using an HP/Agilent 4145B semiconductor parameter analyzer) were carried out at nine temperatures between 300 K and 117 K.

During each transient "time of flight" (TOF) measurement, the gate contact of the OFET was grounded, and the drain was connected to ground across a small 750 Ω resistor. The transient response of the OFET was measured by first applying positive square-wave voltage pulses with magnitudes between 20 V and 80 V from an HP/Agilent 214B pulse generator to the source contact (so that V_{gs} and V_{ds} were both < 0 and the p-channel device was therefore turned on), and measuring both the applied V_s at the drain output with a LeCroy 6030A Oscilloscope with DC 1 MΩ input impedance. When the circuit was complete the rise time of the voltage pulses at the source was approximately ~60 ns.

Because the largest currents supplied by the device were on the order of a few hundred μA, the drain node deviated from ground by a most a few tenths of a volt. Therefore during the transient measurements, $V_{gs} \approx V_{ds}$, and the device was operated in the saturation regime ($V_{ds} > V_{gs}-V_t$). The transient drain currents were recorded with the oscilloscope, and later analyzed in a custom MATLAB program that smoothed the data, corrected for displacement currents present at the onset of the square wave voltage pulse and extracted a turn-on time (τ), which was taken to be interval between the midpoint of the rise time of the applied voltage pulse and the time at which the drain current first reached 2% of full scale.

The applied voltage was then taken to be the average voltage recorded at the source contact during that interval. The uncertainties in both the applied voltage and τ were calculated by taking a window of 30 ns before and after τ (a time interval equal to the rise time of the pulse), and calculating the corresponding average applied source

voltage, V_s, between those initial times and τ. These uncertainties in τ were used to calculate corresponding uncertainties in both the $\mu_{dynamic}$ and the corresponding hole velocity ($v_{dynamic}$), and is explained in further detail below.

3.3: RESULTS AND DISCUSSION

Figure 3.2 shows the Id-Vds characteristics of the pentacene OFET used for both DC and transient testing with a saturation regime FE mobility of ~0.1 cm^2/Vs , and the inset shows a plot of $\sqrt{|I_d|}\ vs. V_{ds}$ in the saturation regime (V_{ds} = -50 V) used to extract the threshold voltage.

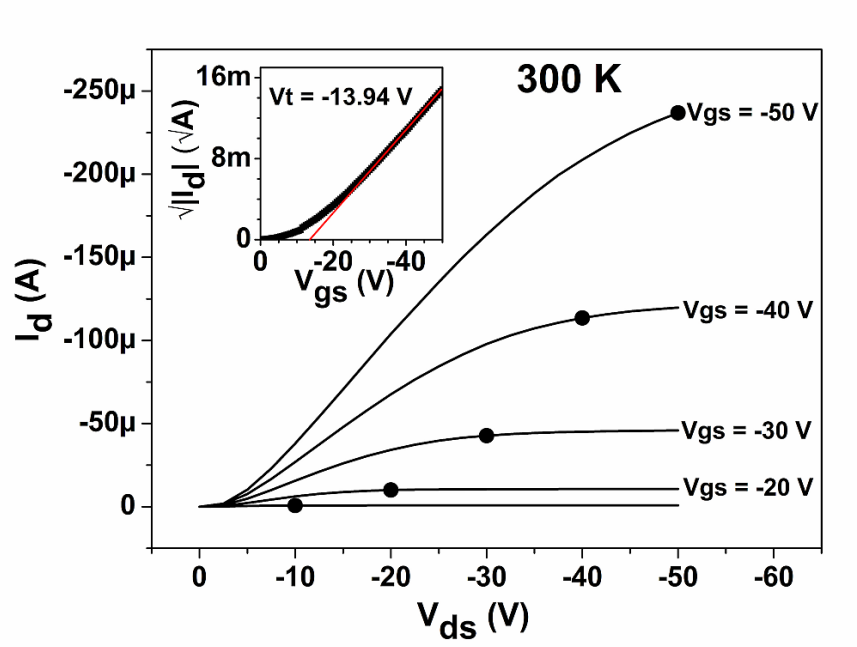

Figure 3.2: Field Effect DC Drain Current (I_d) vs. drain-source voltage (V_{ds}) characteristics of the pentacene OFET at 300 K and at varying gate voltages. The inset shows a plot of the square root of the absolute value of I_d plotted against the gate-source voltage (V_{gs}) at a single V_{ds} of -50 V from which a threshold voltage of -13.94 V was extracted, also at 300 K. The solid black circles indicate the I_d values for which $V_{ds} = V_{gs}$, equivalent to the voltages applied to the device during transient testing.

We chose a device with a relatively high threshold voltage because during the pulsed voltage transient testing, $V_{ds} = V_{gs}$, and with a relatively large threshold voltage we could ensure that the device was unambiguously operating in the saturation regime. We could therefore use equation 3.1 to unambiguously compare saturation regime field effect mobilities extracted from the DC data to the transient results. In the saturation regime I_d is to a good approximation given by:

$$I_d = \frac{W}{2L} C_{ins} \mu_{FE} \left(V_{gs} - V_t\right)^2 \tag{3.1}$$

where W is the channel width, L is the channel length, μ_{FE} is the field-effect mobility and C_{ins} is the capacitance per unit area of the dielectric insulator. We used the DC data to find two separate saturation-regime FE mobilities. In the first, we wanted to isolate the effects of increasing $E_{\|}$, so we held V_{ds} constant at -50 V, and swept V_{gs} from 0 V to -50 V. We then obtained the mobility from equation 3.1 using the following expression:

$$\mu_{FE} = \left[\frac{\left(\frac{\partial \sqrt{|I_d|}}{\partial V_{gs}} \right)^2 C_{ins}}{\left(\frac{W}{2L} \right)} \right] \tag{3.2}$$

where the derivative in equation (3.2) was calculated numerically. We next extracted the threshold voltage of the device at each temperature by performing a linear fit a plot of $\sqrt{|I_d|}$ *vs.* V_{gs}. From equation (3.1), the slope of that linear fit is equal to $\sqrt{\frac{W}{2L} c_{ins} \mu}$, and the y-intercept is equal to $(-V_t)\sqrt{\frac{W}{2L} c_{ins} \mu}$. Therefore V_t may be extracted from the ratio of those two quantities. After obtaining V_t at each temperature, the procedure for

extracting μ_{FE} was repeated for data selected from the I_d-V_{ds} sweeps for which $V_{ds} = V_{gs}$ (see Figure 3.2), reasoning that if there was an appreciable change in the mobility due to increasing $E_{\|}$ that there would be a noticeable difference between the μ_{FE} values where $V_{ds} = -50\ V$ and those μ_{FE} values where $V_{ds} = V_{gs}$.

In a polycrystalline organic semiconductor where charge transport is thermally activated, we would expect τ to increase with decreasing temperature. Figure 3.3 shows that this is indeed the case. Note that all of the drain current transients in Figure 3.3 were taken at $V_{gs} - V_t = -20 \pm 2V$. After examining Figure 3.3 it is obvious that the dynamic transport in the polycrystalline FET has a charge carrier mobility that is thermally activated, and decreases with decreasing temperature. The next step was to examine the transient behavior of the OFET at a single temperature but at varying values of V_{gs}-V_t. The results at a single temperature (169 K) are shown in Figure 3.4.

Note that in both Figures 3.3 and 3.4 the displacement currents of the signals with the greatest τ near the neighborhood of $t = 0$ were a large fraction of (and in some cases greater than) the portion of interest of the transient I_d signal. These displacement current transients were therefore removed so they would not obstruct the other transient signals near the neighborhood of $t = 0$.

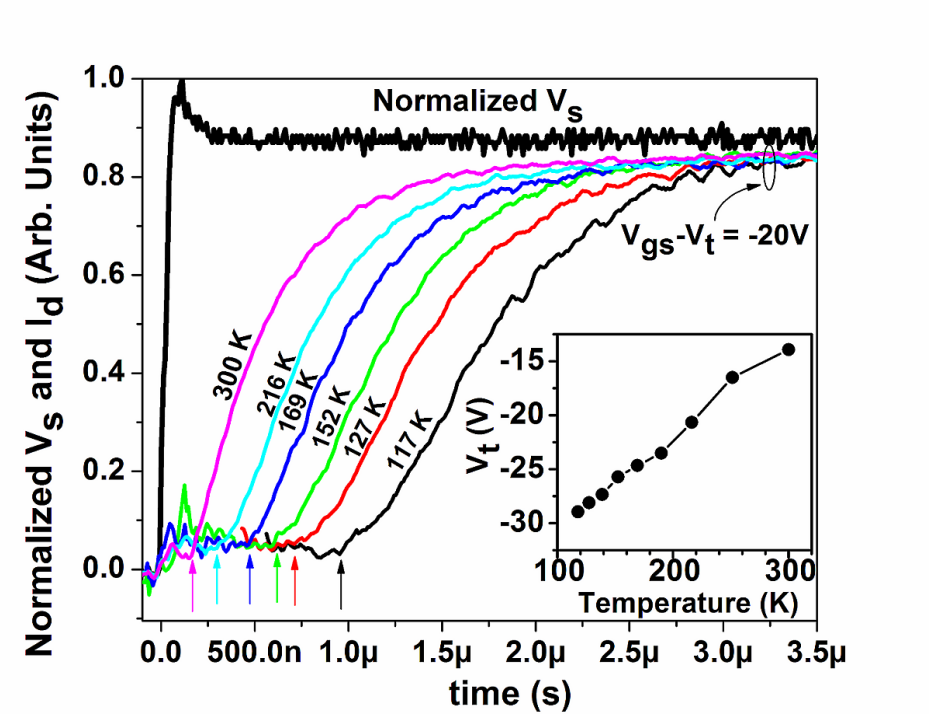

Figure 3.3: Transient applied source pulses and normalized I_d responses of a polycrystalline pentacene OFET at a single value of V_{gs}-V_t = *-20V+/-2V* at several temperatures between 300K and 117K. Note the linear time scale. The turn on time of each transient is indicated by an arrow below the trace of the transient corresponding to each turn-on time, τ. The inset shows V_t as a function of temperature extracted from DC saturation mobility measurements.

In addition to extracting dynamic μ values from the transient data, it is straightforward to extract a dynamic velocity, $v_{dynamic}$, by simply dividing the channel length, L, by τ. Physically, $v_{dynamic}$, represents the average velocity of the fastest edge of charge carriers that drift across the channel during the process of channel formation. Figure 3.5 shows the extracted velocities at multiple temperatures as a function of V_{gs}-V_t on both a log (Figure 3.5a) and linear (Figure 3.5b) scale.

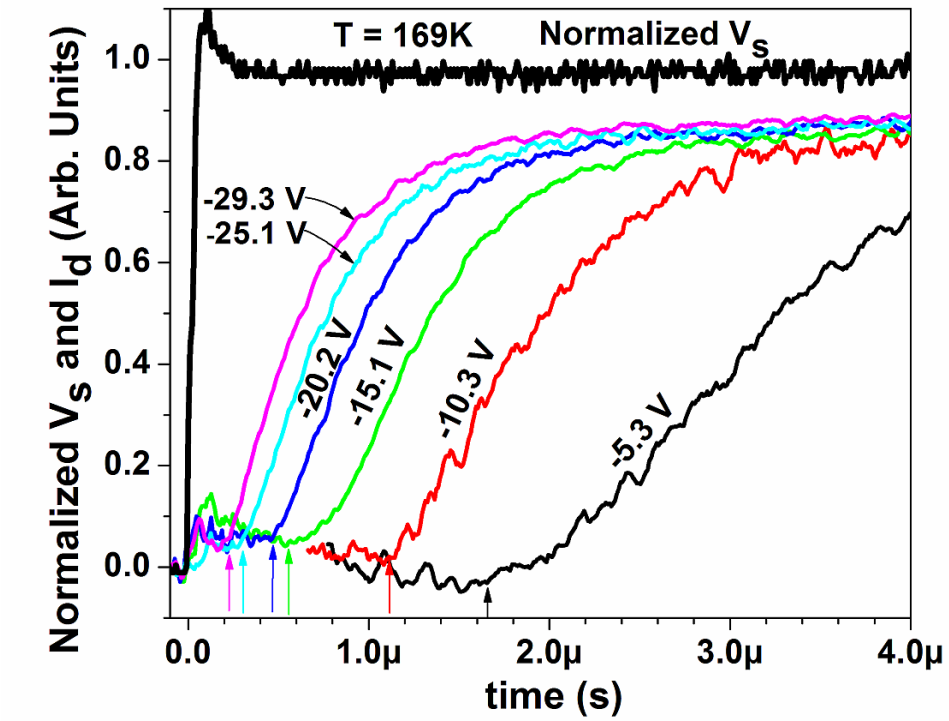

Figure 3.4: the normalized response of the OFET at a single temperature and at varying values of V_{gs}-V_t. Note that the voltages labeling each transient signal indicate a value of V_{gs}-V_t and not V_{ds}. The turn-on time of each transient I_d is indicated by a corresponding arrow below each transient signal.

In order to compare these values to the DC data which was taken on the same device, we used the saturation regime mobilities obtained in the manner described above at all data points where $V_{ds} = V_{gs}$, and assumed a lateral electric field value across the channel of V_{ds}/L to extract a "field-effect velocity", from the definition of the mobility which relates charge carrier velocity to the magnitude of an electric field: $v_{FE} = \mu_{FE}E$. Physically, v_{FE} represents an average velocity of mobile charge carriers traversing the channel once it has been formed and the OFET has been turned on.

In both plots we include for the 300K and 117K data error bars reflecting the uncertainties in τ and *Vgs* which originate from the finite (~60ns) rise time of the pulse in order to give the reader an idea of the uncertainties involved in the transient measurements. Note that these uncertainties increase with increasing V_{gs}-V_t and increasing temperature, due to the fact that under those circumstances the finite rise time of the pulse (60 ns) becomes comparable to the values of τ. The error bars were not included for all data because they would have rendered the plots extremely difficult to read. A similar approach was used to include error bars in the transient vs. dynamic mobility data, which is shown below.

Note that in both plots shown in Figure 3.5 it is evident that at high temperatures the dynamic values of the carrier velocity are greater than the field-effect values, and that this situation is reversed at low temperatures. In order to compare these results to the dynamic and field-effect mobility values, we created analogous plots which are shown in Figure 3.6.

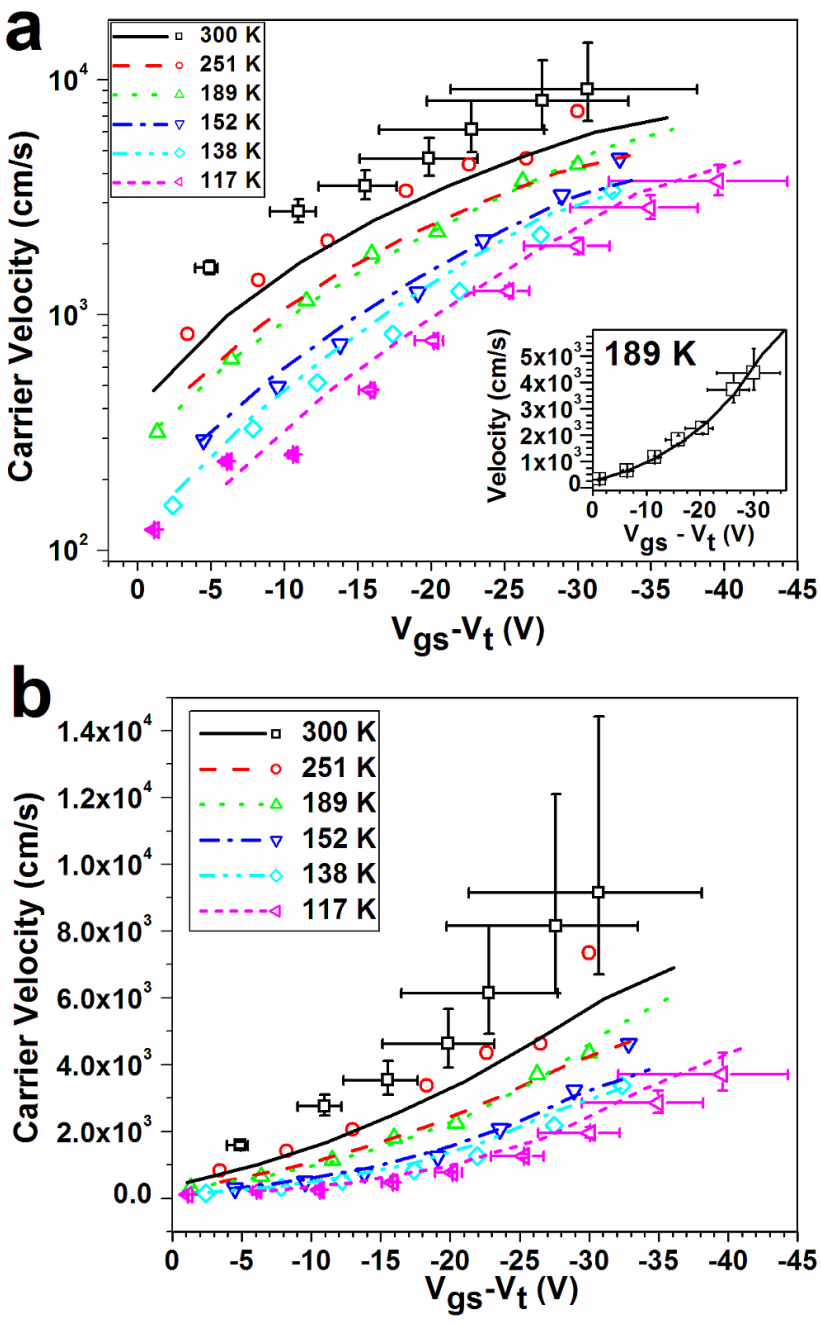

Figure 3.5: Log-linear and linear-linear plots comparing $v_{dynamic}$ to v_{FE} as a function of V_{gs}-V_t at various temperatures between 300K and 117K. The inset of Figure 3.5a shows a plot of $v_{dynamic}$ (open squares) and v_{FE} (solid line) on a linear scale vs. V_{gs}-V_t at 189K, the temperature at which there was the best agreement between these two quantities.

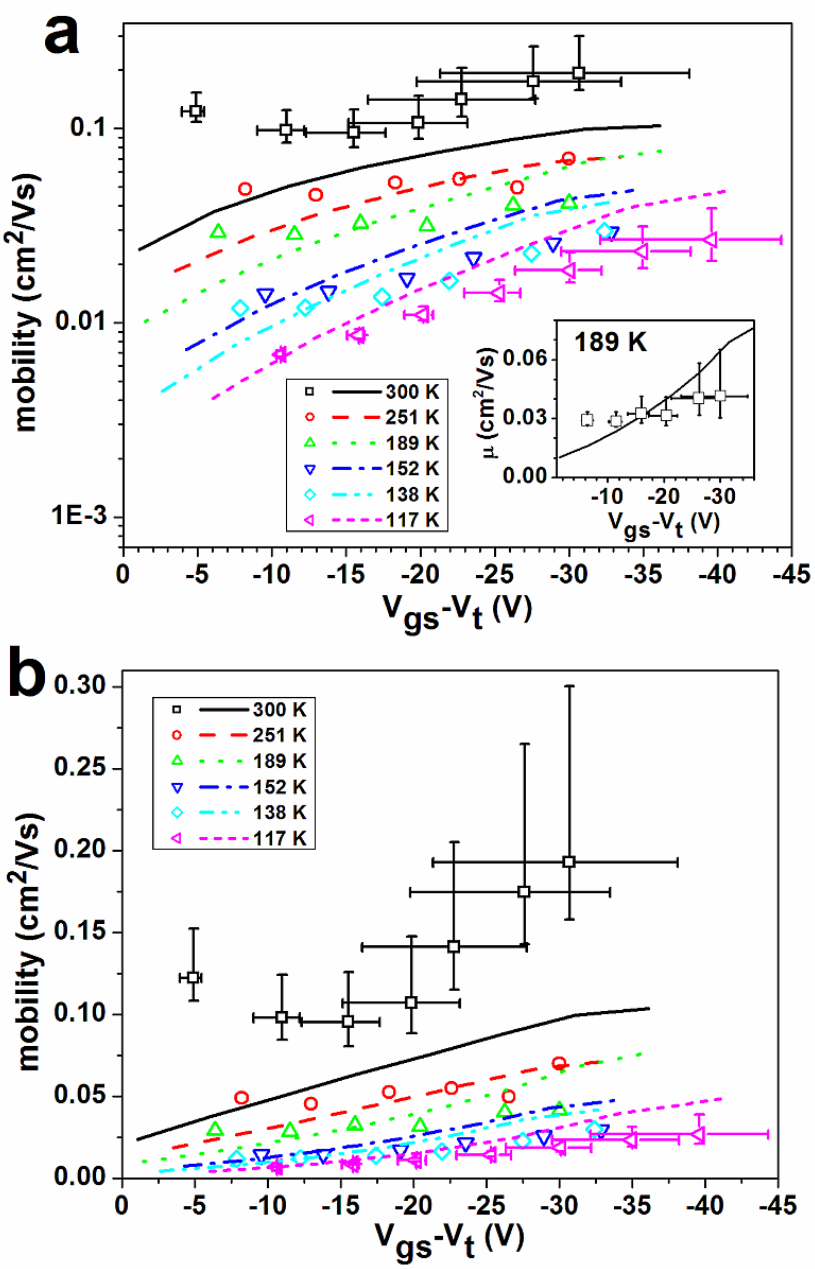

Figure 3.6: Log-linear and linear-linear plots comparing $\mu_{dynamic}$ to μ_{FE} as a function of V_{gs}-V_t at various temperatures between 300K and 117K. The inset of Figure 3.6a shows a plot of $\mu_{dynamic}$ (open squares) and μ_{FE} (solid line) on a linear scale vs. V_{gs}-V_t at 189K, the temperature at which there was the best agreement between these two quantities.

The values of μ_{FE} and v_{FE} in Figure 3.5 and Figure 3.6 show a clear pattern of increasing μ_{FE} with increasing V_{gs}-V_t, which is one of the hallmarks of the Multiple Trap and Release (MTR) model[42,43]. The MTR model assumes a band edge (in this case the edge of the HOMO level) and an exponential density of states descending from the band edge into the forbidden gap which is due to structural, chemical, and/or dynamic disorder in the system. Charge transport occurs in extended states above the band edge, but most charges in the semiconductor are trapped in the exponential Density of States (DOS). The MTR model also predicts thermally activated transport of the form:

$$\mu = \mu_0 exp\left(\frac{-E_a}{k_B T}\right) \tag{3.3}$$

due to the fact that the term $\exp\left(\frac{\Delta}{k_B T}\right)$ is related to the probability that a charge carrier will gain enough energy from phonons in the system to hop up in energy by an amount Δ.

Therefore with respect to the MTR model, E_a is thought to give a measure of the difference between the Fermi Energy (E_f) of the charge carriers in the gap and the band edge. Minari *et. al.* have shown that in Pentacene OFETs an activation energy in the range of several tens of meV is due to the presence of structural disorder due to grain boundaries, and have proposed the magnitude of E_a to be an estimate of the depth of energetic traps in those disordered regions of the material[30,44].

We note that the relatively small increase of $\mu_{dynamic}$ with V_{gs}-V_t compared to μ_{FE} in the inset of Figure 3.6 may be due to the fact that the field effect mobilities have not

been corrected for contact resistances (because we were only able to make measurements of devices at a single channel length) and that the transient mobilities do not appear to be affected by contact effects[42].

From Figure 3.5 it is also evident that at low temperatures $v_{dynamic}$ tends to lag behind v_{FE}, while at higher temperatures it tends to exceed it. Similarly, in Figure 3.6 we see a similar pattern of the dynamic mobilities lagging behind the field-effect mobilities at low temperatures, and exceeding them as the measurements were carried out at higher temperatures. These observations hint at differing E_a values between the dynamic and FE values of v and μ for the same value of V_{gs}-$V_{t.}$

In order to better analyze this discrepancy between μ_{FE} and $\mu_{dynamic}$ (and therefore by extension the differences between v_{FE} and $v_{dynamic}$), we created three Arrhenius plots of $\mu_{dynamic}$, μ_{FE} for $V_{ds} = V_{gs}$ (again, to simulate voltages applied to the device during transient measurements), and μ_{FE} for Vds = -50 V at three separate of V_{gs}-V_t. The three Arrhenius plots are shown below in Figure 3.7. Because the μ_{FE} values for which $V_{ds} = V_{gs}$ were taken from the I_d-V_{ds} data where V_{ds} was swept at intervals of 1 V, but V_{gs} was only stepped at intervals of 5V, there were not enough data points to confidently apply a fit to that data. However qualitatively there appears to be an excellent agreement between the two sets of μ_{FE} data, implying that as we asserted above, the magnitude of the lateral electric field didn't strongly affect mobility values during this experiment. Because the transient measurements were carried out while stepping $V_{ds} = V_{gs}$ at

approximate 5V intervals, when grouping the $\mu_{dynamic}$ data points we allowed a window of +/- 2V around each V_{gs}-V_t value.

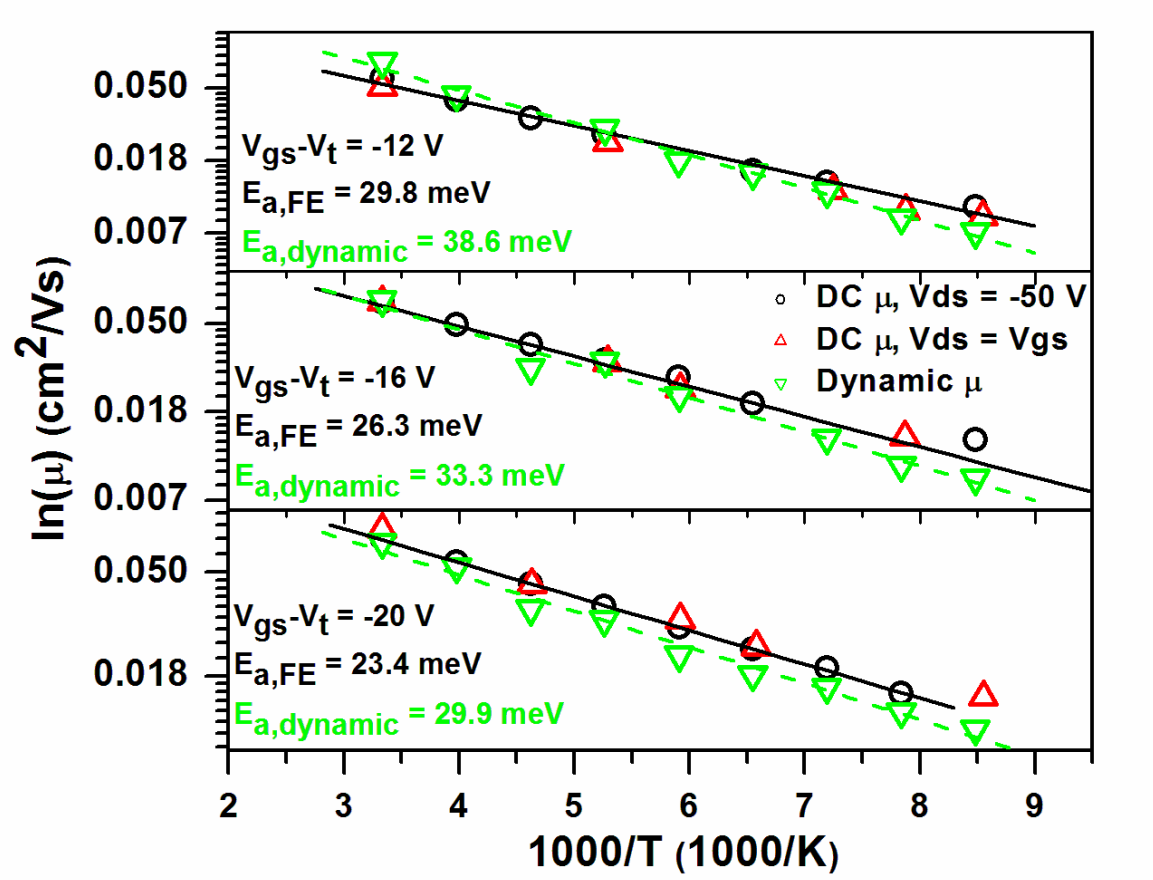

Figure 3.7: Three separate Arrhenius plots, each corresponding to different values of V_{gs}-V_t. In each plot μ_{FE} for V_{ds}=V_{ds} (open red triangles pointing up), μ_{FE} for V_{ds}=*-50V* (open black circles), and $\mu_{dynamic}$ (open green triangles pointing down) are shown and best fits are performed to the μ_{FE} for V_{ds}=*-50V* data (solid black line) and $\mu_{dynamic}$ data (dashed green line). These fits were used to extract the corresponding activation energies, $E_{a,FE}$ and $E_{a,dynamic}$. The values of those activation energies are indicated in the graph

Because μ is plotted on a natural log scale, and the mobility is related to inverse temperature by $\mu = \mu_0 exp\left(\frac{-E_a}{k_B T}\right)$, the slopes of these linear fits can be used to extract the values of E_a. It is obvious from the Arrhenius plots in Figure 3.7 that that the hole

mobilities measured for μ_{FE} and $\mu_{dynamic}$ are both thermally activated and are well described by equation 3.3. However, they are not thermally activated with the same E_a: we observe that the activation energies extracted from the dynamic mobility measurements ($E_{a,dynamic}$) are *ca.* 7 meV higher than the values of E_a extracted from the μ_{FE} measurements ($E_{a,FE}$) at the same V_{gs}-V_t. We explain this discrepancy by noting that the average charge carrier density, p, in the channel during the transient measurement is smaller than p in the channel during the FE measurements because the process of channel formation is occurring during the transient measurement. This will be discussed in more detail further below.

In order to have values of several $E_{a,FE}$ as a function of gate voltage, we also performed linear fits to Arrhenius plots of the field-effect mobility values which we extracted in the manner described above, and for V_{ds} = -50 V. An Arrhenius plot of the field-effect mobility values over a wide range of V_{gs}-V_t is shown below in Figure 3.8. Figure 3.9 shows a plot of all of the dynamic and field-effect activation energies extracted as a function of V_{gs}-V_t, with dashed lines added to guide the eye. As the data shown in Figure 3.5, Figure 3.6, and Figure 3.7 hinted, we can see a clear increase in the transient value of the activation energy of approximately 7 meV when compared to the field-effect value at the same V_{gs}-V_t.

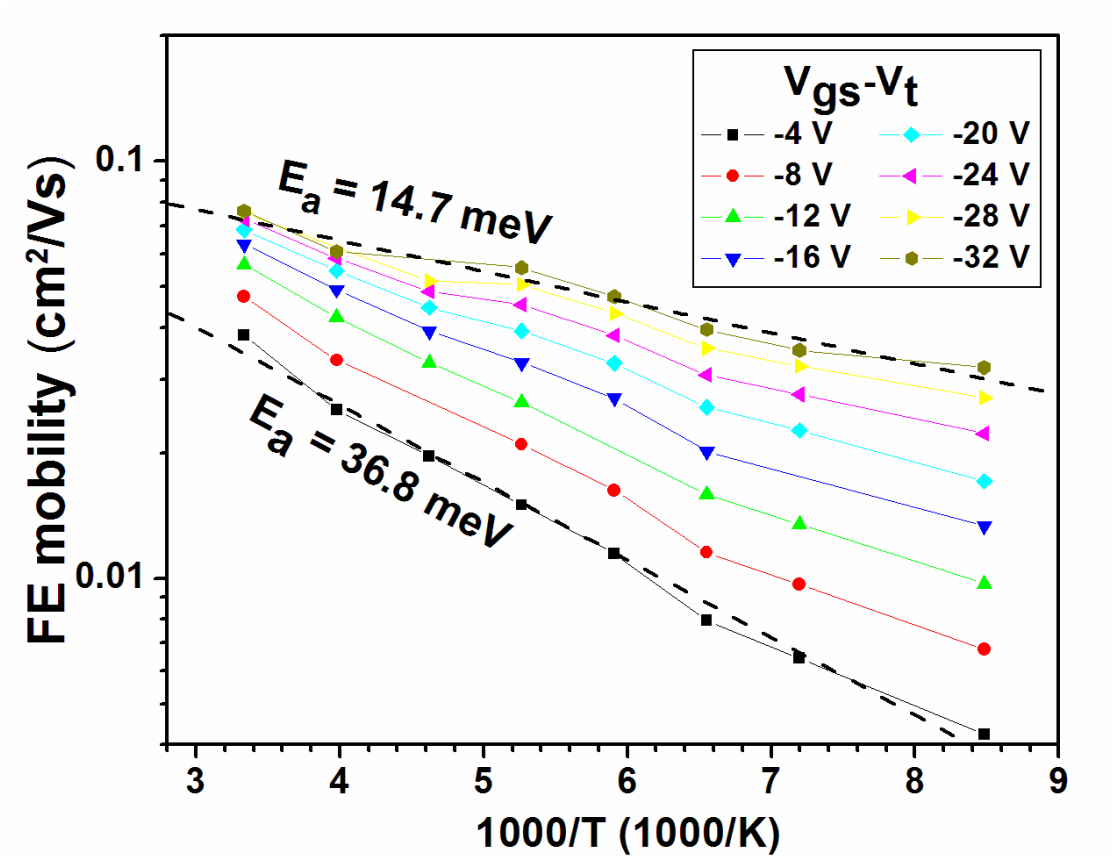

Figure 3.8: Arrhenius plot of the field effect mobility at V_{ds} = -50V for a wide range of V_{gs}-V_t, along with linear fits for the lowest and highest gate voltage values showing the highest and lowest field effect activation energies, respectively.

Equivalently, we can see that the transient mobility requires an additional effect gate voltage of approximately 8 V in order to reach the same activation energy we extract from field-dependent measurements. Since we know the capacitance per unit area of the device is 16.9 nF/cm^2, this corresponds to an additional 1.319x10^8 holes/cm^2. If we assume that that all the charges are confined to the first monolayer of the FET[45], and that the pentacene first monolayer thickness is 1.6 nm[46], than we arrive at an equivalent number of additional 8.24x10^{14} holes/cm^3.

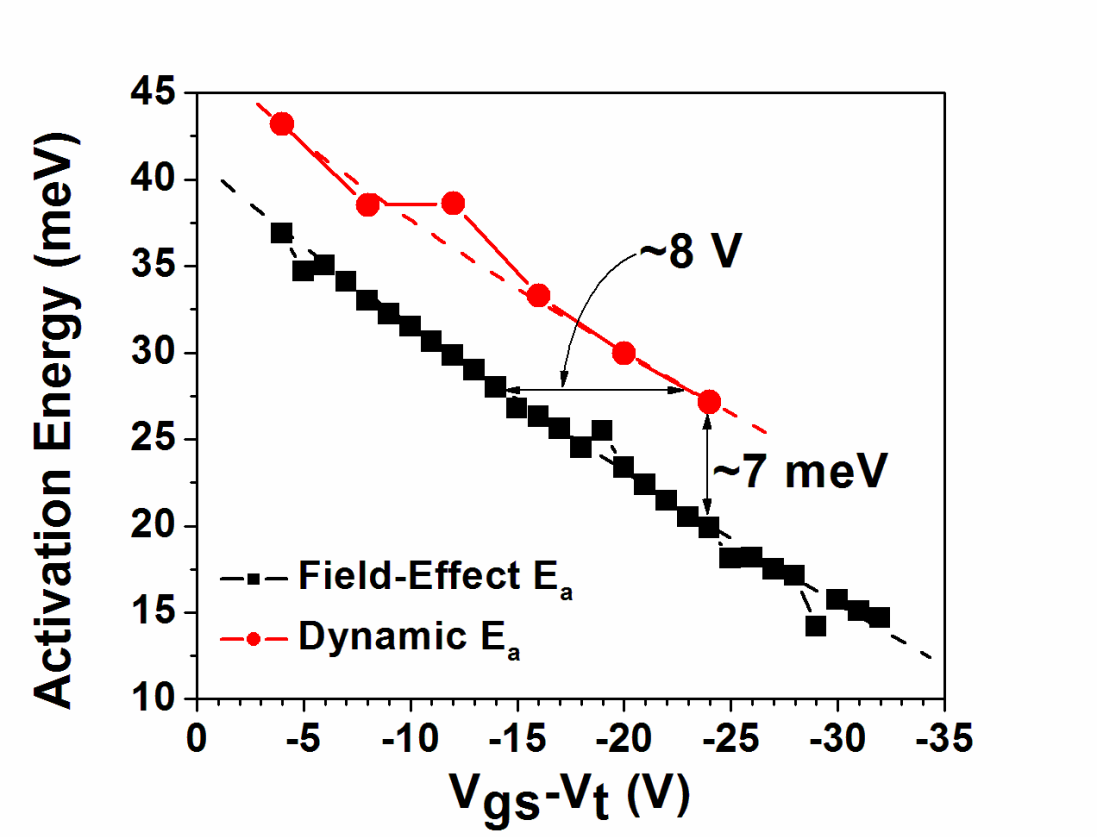

Figure 3.9: Plot of the activation energies extracted from the temperature-dependent field-effect mobilities (black squares), and temperature-dependent dynamic mobilities (red circles), as a function of V_{gs}-V_t. The dashed lines have been added to guide the eye.

$E_{a,FE}$ in Figure 3.9 ranges from 36.8 meV at V_{gs}-V_t = -4 V to 14.7 meV at V_{gs}-V_t = -32 V, while $E_{a,dynamic}$ decreases from 43.2 meV at V_{gs}-V_t = -4 V to 27.2 meV at V_{gs}-V_t = -24 V. We note that this gate-voltage dependent E_a is consistent with previous reports of transport in pentacene OFETs[47] and also that Vissenberg and Matters have successfully modeled such a dependence of E_a (again in a pentacene OFET) on the gate voltage using the density dependent expression for μ_{FE} given in Equation 2.3[31].

The decreasing magnitude of E_a with increasing V_{gs} is a direct result of the increasing occupation of lower lying, less mobile states, leaving charge carriers to occupy

energetic states where hopping from site to site is more likely[31]. When discussing the density dependent mobility in various disordered semiconducting polymers Tanase *et. al.* also showed a decrease of E_a with increasing V_{gs}[32]. This dependence of E_a on V_{gs}-V_t, the fact that V_t increases from -13.9 V at 300 K to -29 V at 117K (inset of Figure 3.3), and the relatively low mobility of the pentacene OFET tested (~0.1 cm^2/Vs) are all strongly indicative of a high density of traps in the material and therefore hole transport that is compatible with the MTR model.

3.4: CONCLUSION

If both $E_{a,dynamic}$ and $E_{a,FE}$ were quantities measured with the OFET in equilibrium, than it would be a contradiction for $E_{a,dynamic} > E_{a,FE}$ and yet at the same temperature and V_{gs}-V_t have $\mu_{dynamic} > \mu_{FE}$, as is the case at high temperatures. Similarly, it would not make sense for the corresponding FE and dynamic velocities to follow the same pattern. However, the transient experiment measures the velocities and mobilities of the first carriers to exit the device *during the process of channel formation*, which must necessarily belong to one extreme of the energetic distribution of all the charge carriers in the device, and which at high temperatures have not yet reached thermal equilibrium with their environment.

We propose as an explanation that at low temperatures $\tau_{trap} > \tau_{mobile}$, so that charge carriers which are hopping across the channel of the OFET during the transient experiment are very likely to be trapped at sites with energies that are lower than the

average E_f of charges once the channel has formed. Thus at low temperatures $\mu_{dynamic} < \mu_{FE}$ and $v_{dynamic} < v_{FE}$. However at higher temperatures the most energetic charge carriers seem to be able to access sites closer to the band edge for which $\tau_{trap} \lesssim \tau_{mobile}$. The energy of the sites which these more thermally energetic charge carriers must be able to access apparently are closer to the band edge than the corresponding average E_f of holes in the channel once the accumulation layer has been formed, allowing $\mu_{dynamic}$ to be greater than μ_{FE} and $v_{dynamic}$ to be greater than v_{FE} despite a lower local charge carrier concentration. The crossover temperature between these two regimes appears to occur in the neighborhood of 189 K, as the insets of Figures 3.5a and 3.6a indicate.

If the charge carrier density is lower, than the average E_f of the charge carriers in the gap during the transient measurement will be farther away from the band edge than the average E_f of charge carriers during field-effect (DC) measurements, when the channel formation process has already been completed. A schematic band diagram of pentacene consistent with the MTR model is shown below in Figure 3.10 to illustrate this point.

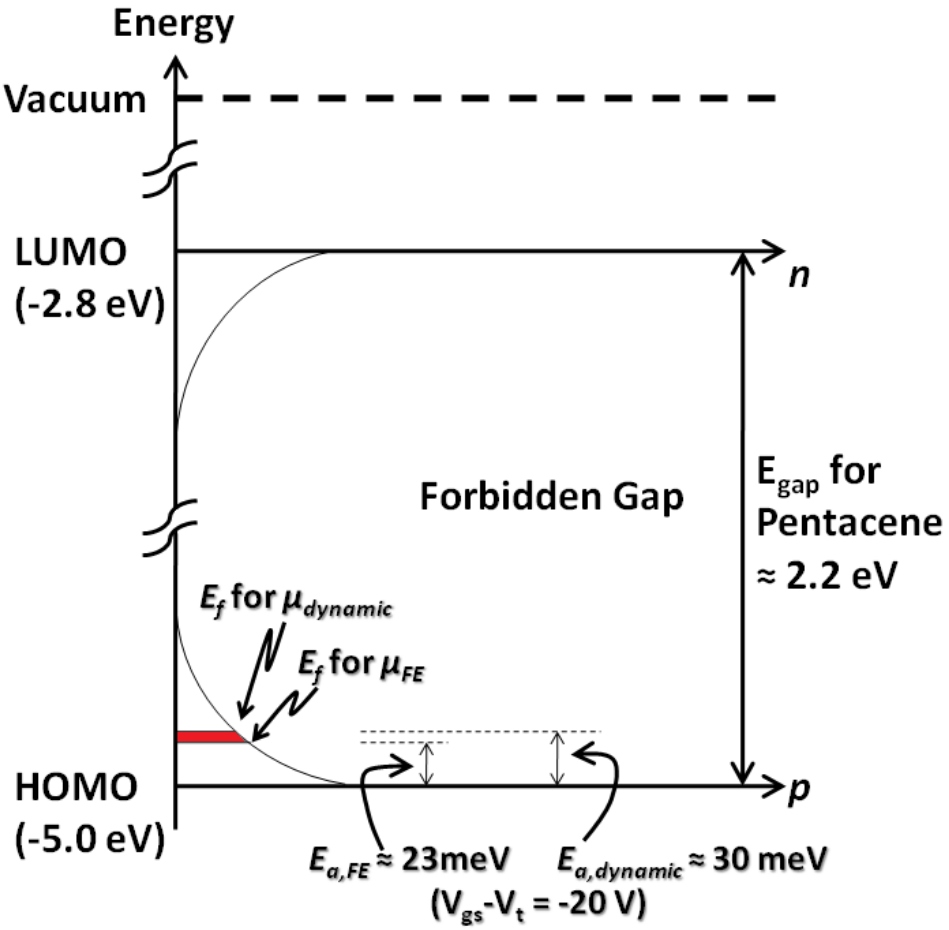

Figure 3.10: Energy diagram consistent with the MTR model of a polycrystalline pentacene thin film. The HOMO and LUMO levels are indicated as band edges, with exponential distributions of trapping states due to disorder at the grain boundaries in the pentacene thin film[30,44] descending from the LUMO and rising from HOMO. The average values of E_f of holes during the dynamic mobility measurement and during the field-effect mobility measurement are indicated, along with the corresponding values of the activation energies for both measurements at V_{gs}-V_t = -20 V.

As an interesting aside, we note that the LUMO level of Pentacene of approximately 2.8 eV below vacuum[48] corresponds the energy of photons with a wavelength of ~443 nm, well within the visible spectrum of blue light present under ambient conditions. Therefore ambient light is more than capable of removing electrons

in the LUMO of pentacene to vacuum. That, along with the high density of electron traps at the organic/SiO_2 interface (which we discuss thoroughly in Chapter 4) are two reasons why Pentacene has historically been a hole only transport material. However, we note that recently Ahles *et. al.* were able to show n-type conduction in a pentacene OFET by doping the pentacene/SiO_2 interface with ~0.6 nm of Ca (where the Ca acts as an electron donating material that can effectively fill the electron traps at that interface[49]) and by testing in a glovebox with an inert atmosphere to prevent oxidation of the material by atmospheric O_2.

As a check of the validity of our experimental methodology, we include in Figure 3.11 a plot comparing at several voltages the DC values of I_d extracted for $V_{ds} = V_{gs}$ to the transient I_d values averaged between 300 μs and 350 μs after the application of the voltage pulse to the source contact. As expected, the DC values of the drain current and values measured during the dynamic measurements agree well once the channel has been fully formed.

In conclusion, we have refined the pulsed voltage mobility measurement technique introduced in Dunn *et. al.*[33], and applied the measurement technique to a polycrystalline pentacene OFET over a wide range of temperatures. As was independently found by Dost *et. al.*[34] we found the mobility to be proportional to V_{gs}-V_t instead of V_{ds}. As an explanation we proposed that over the range of lateral electric fields explored in this work the hole mobility dependence is far more dependent on charge carrier density than lateral electric field.

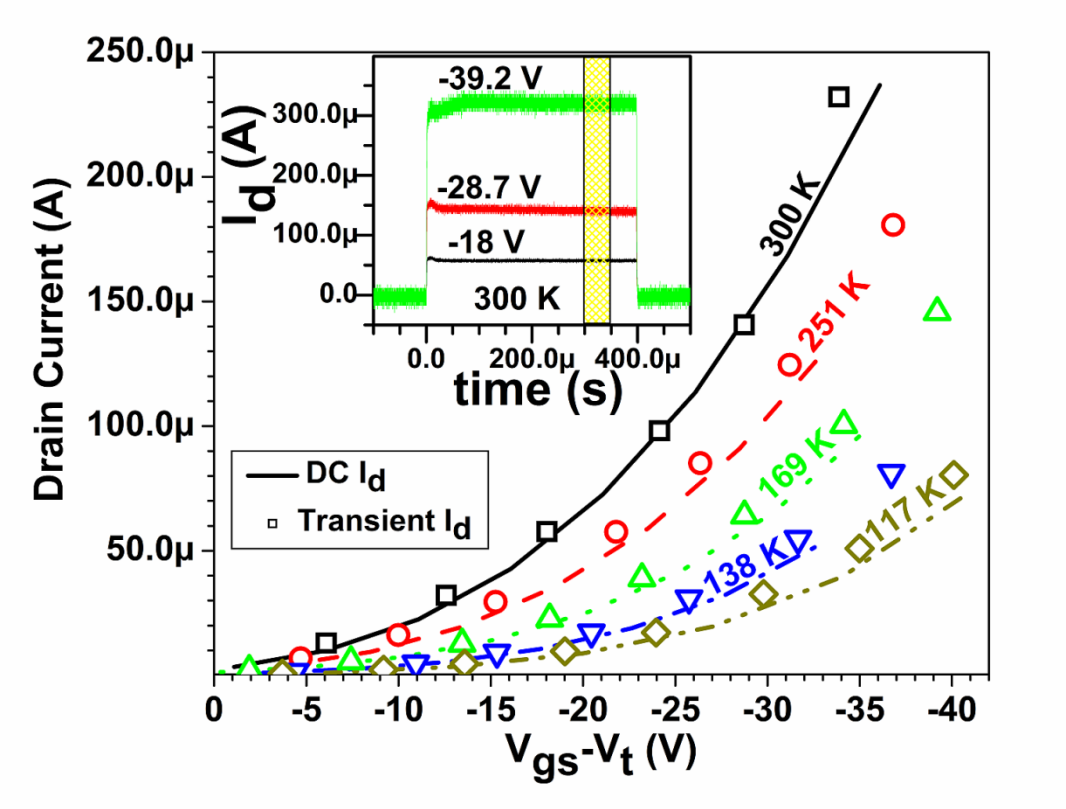

Figure 3.11: DC (lines) and transient (open symbols) drain currents at various temperatures as a function of V_{gs}-V_t, all taken at source, gate, and/or drain voltages for which $V_{ds} = V_{gs}$. The transient drain current data were obtained by averaging the drain current responses between 300 µs and 350 µs after the application of the voltage pulse to the source contact. The portion of the transient drain current signal averaged to obtain each data point is represented by the shaded portions of the three drain current transients shown in the inset plot, which were all taken at 300 K and at the values of V_{gs}-V_t which label each transient.

We found charge transport in the OFET investigated both by both conventional DC and dynamic measurements to be compatible with the MTR model. We found that both $\mu_{dynamic}$ and μ_{FE} exhibited the hallmarks of thermally activated hopping charge transport, and were both characterized by separate activation energies which are likely

related to the height of barriers that charge carriers need to overcome in order to reach mobile states. We found $E_{a,dynamic} > E_{a,FE}$ by *ca.* 7 meV, which we attributed to a lower charge carrier density in the channel during the transient measurement than is present during DC measurements. At high temperatures, we noted that $\mu_{dynamic} > \mu_{FE}$ and $v_{dynamic} > v_{FE}$, and proposed as an explanation that the most mobile charge carriers in the transient measurement at high temperatures are far from thermal equilibrium, and are therefore able to access more energetic sites with higher mobilities than they would be able to at the same charge carrier density in a DC field effect measurement.

Chapter 4: Temperature Dependent Transient Response in PDI-8CN_2 FETs

4.1: INTRODUCTION

In this chapter we focus on electron transport in an OFET based on the organic semiconductor *N,N'*-bis(n-octyl)-dicyanoperylene-3,4:9,10-bis(dicarboximide) (PDI-8CN_2), whose chemical structure is shown in the inset of Figure 4.2. We obtained the PDI-8CN_2 from the group of Prof. Tobin Marks and Dr. Antonio Facchetti at Northwestern University, who first synthesized the material as an air-stable electron-transporting organic semiconductor[50,51].

The study of electron transport in OFETs is extremely important for the eventual realization of organic complementary logic circuits[52]. However, for several reasons n-channel OFETs have historically been more difficult to fabricate, tend to have lower mobilities than their p-channel counterparts, and have been successfully demonstrated with fewer materials. First, as was mentioned in the first chapter, LUMO bands tend to be narrower than HOMO bands because the anti-bonding-type symmetry of the LUMO bands means that there is increased off-diagonal interaction of the p_z orbitals of neighboring carbon atoms[7]. This translates to a reduced transfer integral, t, between neighboring electronic wave functions in the LUMO band when compared to the HOMO. In semi-classical electron-transfer theory, the electron hopping rate, k_{ET}, is related to the square of the transfer integral[53]:

$$k_{ET} = \frac{4\pi^2}{h}\frac{1}{\sqrt{4\pi k_B T}}t^2 exp\left(-\frac{\lambda}{4k_B T}\right) \quad (4.1)$$

where T is the temperature, λ is the reorganization energy, h is Planck's constant, and k_B is the Boltzmann constant.

Second, on average organic semiconductors have a relatively wide gap between their HOMO and LUMO levels (typically greater than 1 eV, although in the last few years there has been much effort focused on novel "low bandgap" polymers for photovoltaic applications[54]). This means that the LUMO level can actually be within a few eV of vacuum, making the materials very vulnerable to O_2 induced photo-oxidation in atmosphere. Charge injection from the metal contacts into the organic semiconductor can also be a bottleneck for device performance. Although metal/organic semiconductor heterojunctions are not the focus of this dissertation, we note that typically devices perform well when the work functions of the metal contacts are well matched to the energy level at which charges are being injected or extracted. (*e.g.*, matching the HOMO level of ~-5.0 eV of Pentacene to the -5.1 eV work function of gold).

Although low work function metals such as Ca and Ba have been shown to function successfully as electron-injecting contacts metal/organic interfaces, they are difficult to work with, and require an inert atmosphere during testing. We note here that de Boer *et. al.* have shown that self-assembled monolayers (SAMs) may be used to adjust metal work functions by more than one eV[55].

Another points which helps to explain the general trend toward better performing p-channel OFETs, and the point which has the most bearing on the work shown in this

chapter, is that traditionally OFETs have been fabricated in Si substrates with a thermally grown SiO_2 oxide as the gate-dielectric. However SiO_2 dielectrics have been shown to be extremely efficient at trapping electrons due to the electrochemical process shown schematically below in Figure 4.1.

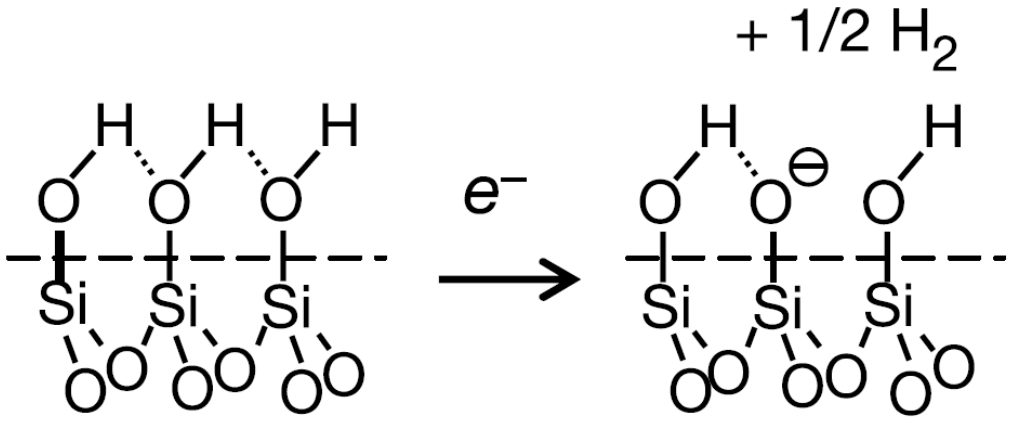

Figure 4.1: Schematic of the electron trapping process at the semiconductor/dielectric interface of an SiO_2 dielectric and an organic semiconductor. Figure reprinted by permission from Macmillian Publishers Ltd.: NATURE Vol. 434, 10 March 2005, pp. 194-199, copyright 2005[56].

This process of SiOH reduction creates a layer of trapped immobile electrons at the SiO_2/organic interface that shields the electric field between the gate and the channel and so raises the threshold voltage that one needs to overcome in order to form an accumulation region of electrons.

Perylene, a prototypical small molecule organic semiconductor used in n-channel OFETs, is the molecule on which PDI-8CN_2 is based. Because the Cyano (CN) groups present in the PDI-8CN_2 structure (not present in Perylene) are electron-withdrawing in nature, their presence lowers both the HOMO and LUMO values of PDI-8CN_2 farther from vacuum when compared to Perylene, therefore rendering PDI-8CN_2 more air stable.

When we compare the HOMO and LUMO levels of Perylene (-5.32 and -3.29 eV, respectively)[57] to the HOMO and LUMO levels of PDI-8CN_2 (-6.6 and -4.3 eV, respectively, obtained by Marks *et. al.* through a combination of optical absorption and electrochemical redox reaction data)[58], we see that this is indeed the case. The alkyl chains present in the PDI-8CN_2 molecule also render the molecule solution-processable, making it very attractive for applications requiring low-cost roll-to-roll or even ink-jet printing processing steps.

Chua *et. al.* have noted that n-channel FET operation seems possible in organic semiconductors on SiO_2 if the semiconductor has an Electron Affinity (EA), which in the context of organic semiconductors is equated with the LUMO level, of -3.85 eV or more below vacuum[56]. The estimated HOMO and LUMO levels for PDI-8CN_2 mentioned above compare favorably to this figure[58], and do indeed translate to a more air-stable electron-transporting material[52,59].

In the data below we use a combination of FE and transient mobility measurements to gain a rough idea of the shape of the energetic DOS of our device.

4.2: MATERIALS AND EXPERIMENTAL METHODS

The PDI-8CN_2 OFETs were fabricated on heavily doped Si wafers with 103 nm of thermally grown SiO_2 used as the gate dielectric, with a corresponding gate capacitance of $\frac{\varepsilon_0 \varepsilon_r}{t} = 33.5\, nF/cm^2$. The substrate was cleaned by sonicating in sequential baths of acetone, methanol, and dionized (DI) water for 2 minutes each. The

samples were then air dried with a Nitrogen gun, and treated in a UV-Ozone chamber (Novascan Technologies, Inc.) at room temperature for 3 minutes in order to remove any remaining organic contaminants on the SiO_2 surface. The substrate was then baked on a hotplate at 180 ºC for 10 minutes and allowed to cool to room temperature. The substrate was then isolated in a sealed container with a saturated atmosphere of hexamethyldisilazane (HMDS). The HMDS (and other silanes as well) react covalently with the SiO_2 dielectric to form a SAM on the SiO2 surface that encourages increased ordering and therefore higher mobility in deposited organic semiconductors. The SAM both reduces electron trapping due to the mechanism depicted above in Figure 4.1 and also to lower the surface energy of the SiO_2, possibly by removing any residual water molecules or other polar substances adhering to the substrate[60].

Prior to the deposition of PDI-8CN_2, the substrate was heated to 100 ºC at a pressure better than $3x10^{-7}$ torr. Both the pressure and substrate temperature were maintained during the organic semiconductor deposition. The PDI-8CN_2 layer was sublimed from a thermal boat at a rate of ~0.1 Å/s for the first 50 Å, and a rate of ~0.4 Å/s for an additional 350 Å. The sample was then allowed to cool to room temperature, and returned to atmosphere in order to apply a shadow mask prior to the deposition of the Au top contacts to form a channel with an effective width, *W*, of 750 μm and an effective length, *L*, of 50 μm. Following the application of the shadow mask to the sample it was returned to high vacuum, and 100 nm of Au was evaporated from a thermal boat in a vacuum better than $1x10^{-6}$ torr at a rate of ~0.5 Å/s. During the Au deposition the sample was kept at room temperature. The sample was stored overnight in a dark nitrogen

dessicator before being transported in the dark to a vacuum cryoprobe station (Desert Cryogenics) for testing.

For each transient measurement, a negative square wave voltage pulse with a magnitude between -5 V and -50 V was applied to the source contact. Voltages with a magnitude greater than |50 V| were not used due to the danger of dielectric breakdown because of the relatively thin gate dielectric. Where as previously a small, 750 Ω resistor was connected to ground at the drain output in order to generate a measureable voltage drop from the drain current, for these data a variable-gain high-speed current amplifier (Femto model DHPCA-100) with a maximum variable gain of 10^8 V/A was used in order to increase the current range of measureable drain current transients.

Both the source voltage input and output from the DHPCA-100 were measured with a LeCroy 6030A Oscilloscope with DC 1 MΩ input impedance. The signal from the DHPCA-100 was averaged between 50 and 500 times before recording, depending on the signal to noise ratio. At higher applied voltages and temperatures, the signal to noise ratio was quite good. At lower voltages and temperatures, we found the resolution of the measurement apparatus to be approximately 250 pA (*i.e.,* transient signals with corresponding drain currents ≥ 250 pA were resolvable) at amplifications of 10^8 and a corresponding bandwidth of the DHPCA-100 of 220 kHz. The turn-on times at these low temperatures and applied voltages were on the order of a millisecond.

Both transient and DC measurements were taken at 7 temperatures between 296K and 150 K. Apiezon N Cryogenic High Vacuum Thermal Grease (purchased from Desert Cryogenics) was used both to secure the OFET to the chilled probe station chuck and also

to ensure good thermal contact between the chuck and the sample. Care was taken to ensure the stability of the temperature of the sample by waiting at least an hour after each temperature step before taking data.

4.3: RESULTS AND DISCUSSION

Figure 4.2 shows the I_d-V_{ds} curves of the PDI-8CN_2 OFET tested at room temperature. A few characteristics of this plot are noteworthy. First, and most importantly, there is virtually no hysteresis visible in the forward and backward sweeps at a single gate voltage, which will contrast sharply with the I_d-V_{gs} curves of the same device that will be discussed below. The inset shows the chemical structure of PDI-8CN_2. We note here that because of its large EA and corresponding resistance to photo-oxidation in air, as well as its propensity to form well ordered films when sublimed in vacuum, perylene based molecules are one of only a few archetypal organic semiconductors used successfully in n-channel OFETs[61]. Also, Cyano (CN) groups are known to be electron-withdrawing in nature and therefore their inclusion in a molecule is expected to push both the HOMO and LUMO levels farther from vacuum, therefore rendering it more air-stable.

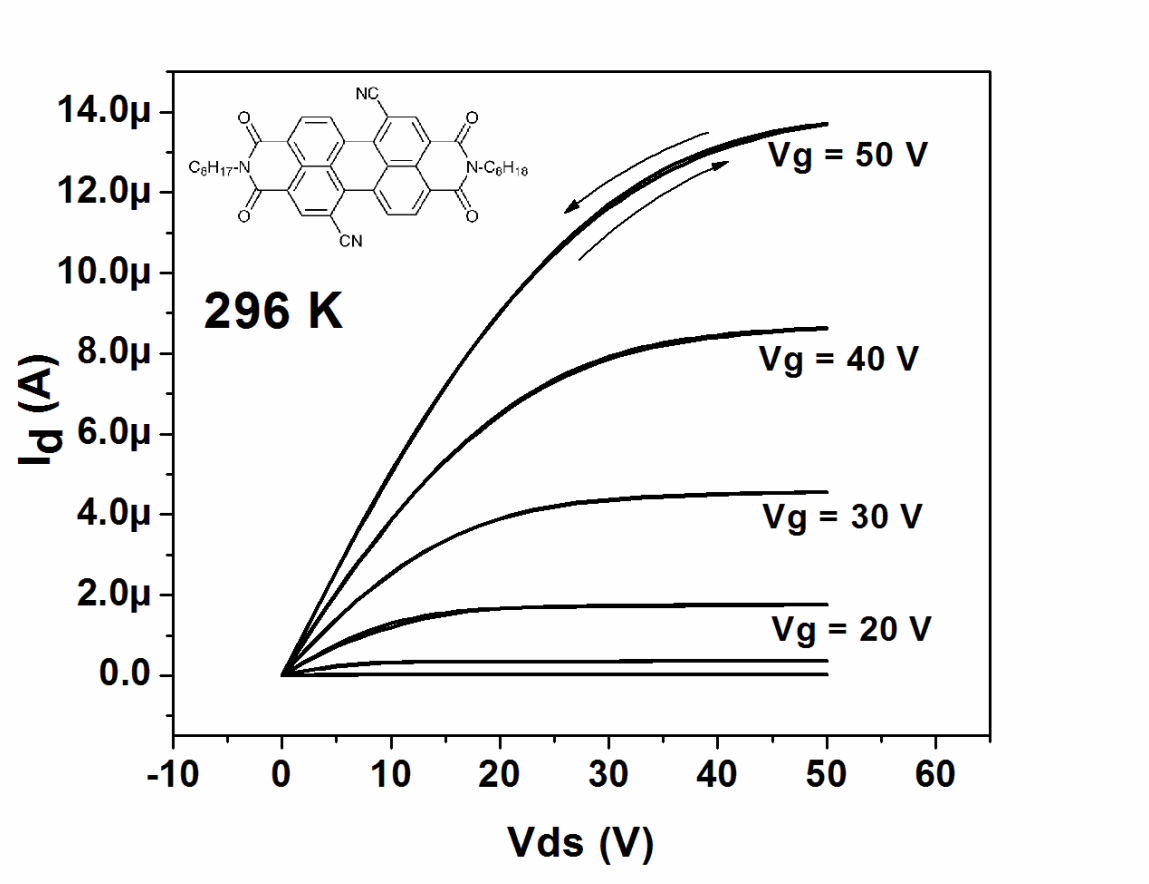

Figure 4.2: I_d-V_{ds} curves of a PDI-8CN$_2$ based n-channel OFET at room temperature. Note the lack of hysteresis of data when sweeping V_{ds}. Each curve is labeled with the appropriate gate voltage. The inset shows the chemical structure of PDI-8CN$_2$.

Finally, a clue to the nature of the contact between the metal and the semiconductor can be gained by analyzing the behavior of the I_d-V_{ds} at low V_{ds}. Poor contacts normally result in a superlinear dependence of I_d on V_{ds} in this region. High quality contacts which are ohmic or near-ohmic in nature produce resemble those I_d-V_{ds} curves at low V_{ds} resembling those seen in Figure 4.2. This is true despite the approximately 0.8 eV offset between the LUMO of PDI-8CN$_2$ (-4.3 eV) and the work function of Au (-5.1 eV). However the study of interfaces and the nature of contacts

between metals and organic semiconductors is nontrivial and there are many phenomena that could result a sharp reduction of what one would naïvely assume from classic metal/semiconductor junction theory. For example, it has been demonstrated that the interface dipole which forms at the C_{60}/Au interface decreases the electron injection barrier by 0.64 eV[62]. Electron tunneling from the metal into the semiconductor due to extremely sharp band bending from a large accumulation layer at the metal/organic interface may also play a role.

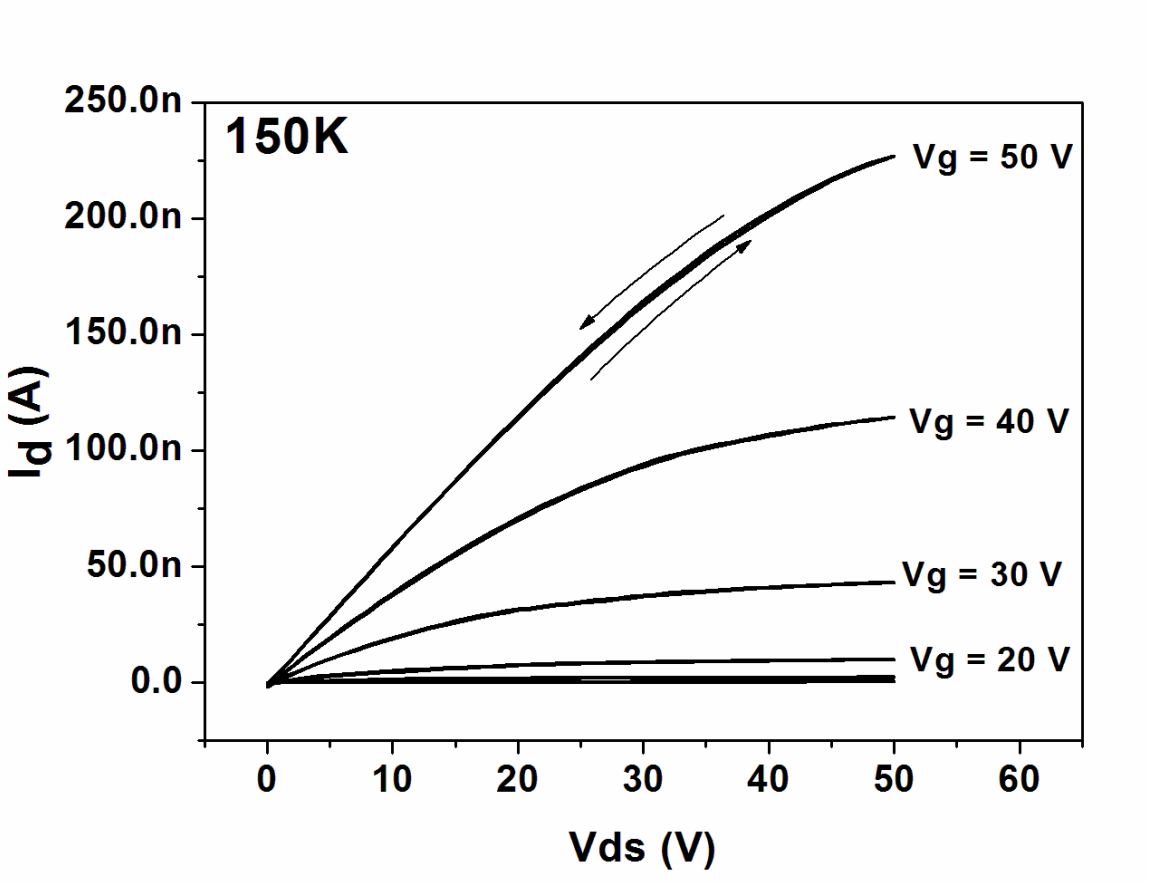

Figure 4.3: I_d-V_{ds} curves of a PDI-8CN_2 based n-channel OFET at 150 K. Note the marked decrease in the current from ~14 μA at 296 K to less than 250 nA here. The lack of hysteresis effects here and excellent metal/organic contacts are also noteworthy. Each curve is labeled with the appropriate gate voltage.

Figure 4.3 shows data analogous to those shown in Figure 4.2, although this I_d-V_{ds} plot was taken at 150 K, the lower limit of the temperature range explored in this chapter. Note first that the excellent contacts between the metal source and drain electrodes and the semiconductor persist even at this low temperature, lending more weight to the tunneling hypothesis mentioned above.

As in the previous chapter, the transient measurements here were carried out in the saturation regime ($V_{ds}>V_{gs}$-V_t). We therefore use equation (3.2) to extract field-effect mobilities as a function of gate voltage and a linear fit was performed to $\sqrt{|I_d|} = \left(\frac{W}{2L}\mu_{FE}\right)V_{gs} - \left[(V_t)\left(\frac{W}{2L}\mu_{FE}\right)\right]$ (taken from equation 3.1) to extract threshold voltages. The I_d-V_{gs} curves used to extract field effect mobilities are shown in Figure 4.4, where it is easy to see that unlike the I_d-V_{ds} curves shown above, there is a large hysteresis effect present in this data. Specifically, when sweeping the gate voltage from 0V to 50V, the drain current is lower than what we see when returning the device from 50V back to 0V. The origin of this behavior is that prior to extracting any current from the device, the channel is empty and therefore any low trying traps in the energetic DOS are unfilled. After sweeping from 0V to 50V, the channel has been formed and any traps that may be present below the band edge have been filled. In the context of the MTR model, any extra charges introduced into the channel have an average energy closer to the band edge, and therefore will have a higher mobility, which results in a higher drain current.

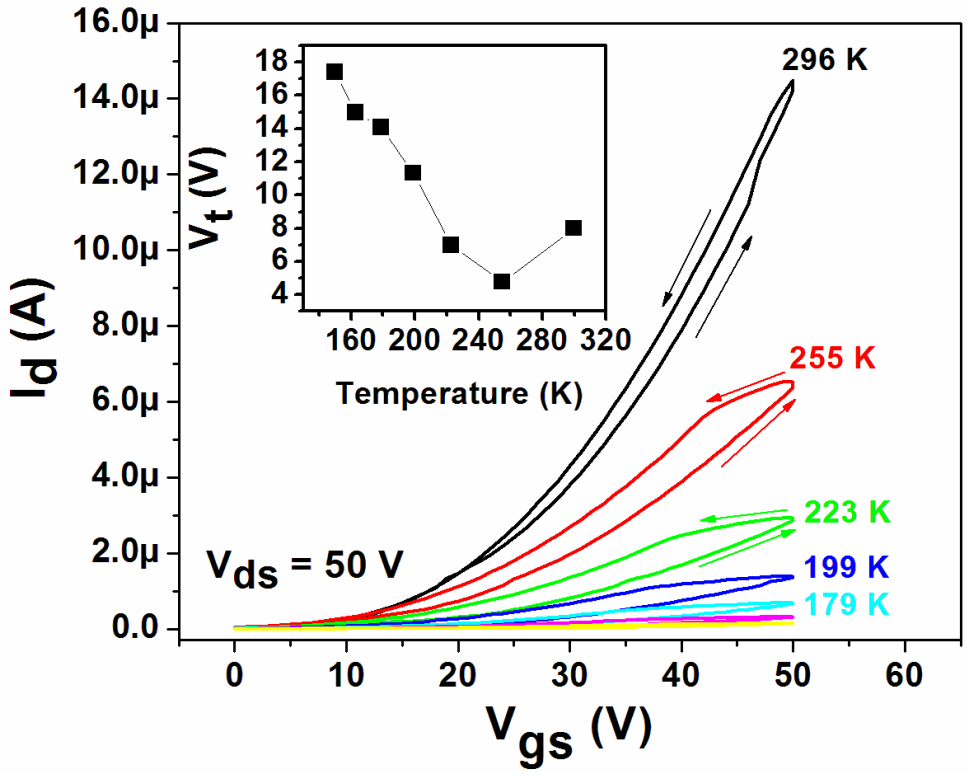

Figure 4.4: I_d-V_{gs} curves of the PDI-8CN$_2$ OFET for V_{ds} = *-50 V* at several temperatures. Inset shows threshold voltage as a function of temperature. The threshold voltages were also extracted in the saturation regime for V_{ds} = *-50 V*.

This hypothesis would be supported by an observation of an increased relative hysteresis effect with decreasing temperature. Figure 4.5 shows that this is indeed the case. At lower temperatures, charges which fill traps below the LUMO band edge are less likely to be thermally excited out of those traps, and so the relative difference between the forward sweep, where those traps are being filled, and the backward sweep, where those traps have already been filled, is more pronounced. This is indicative of a polycrystalline thin film with a high density of traps.

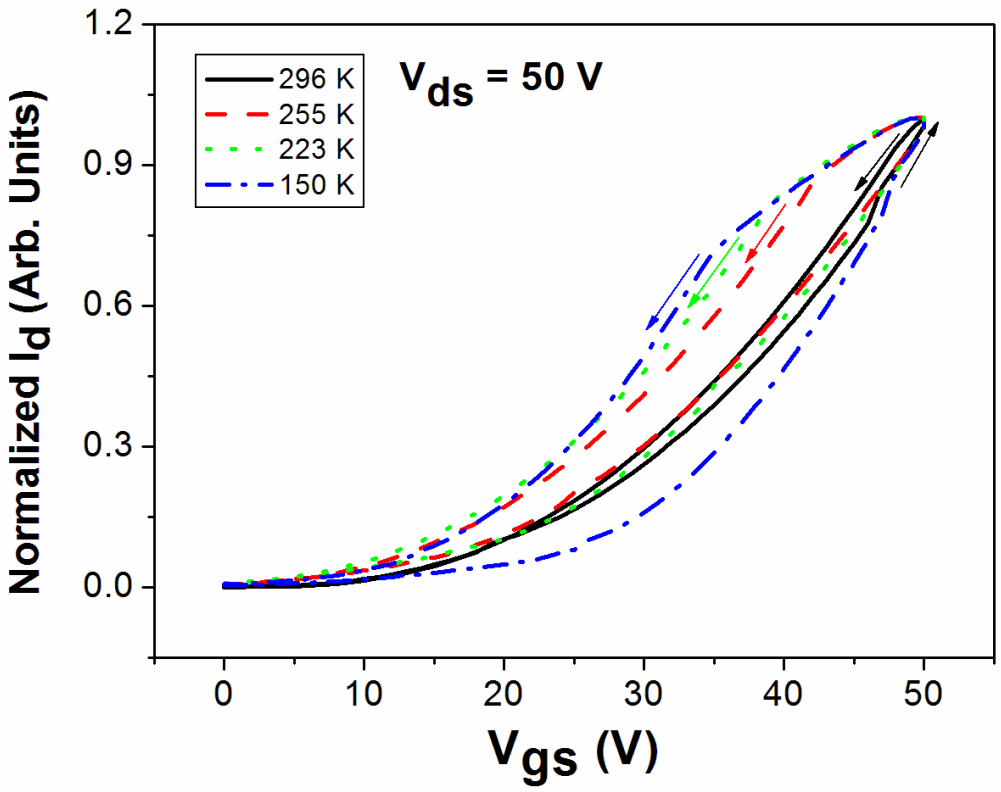

Figure 4.5: Normalized I_d-V_{gs} showing an increased relative hysteresis effect with decreasing temperatures. Each of the backward sweeps are indicated by an arrow.

Oscilloscope traces of the drain current transient response to the negative square wave source voltage pulse at room temperature and at varying values of V_{gs}-V_t are shown in Figure 4.6. The turn-on time of the OFET for each applied voltage value is indicated by the arrow above each trace. Note also in Figure 4.6 the ringing near the origin which is likely due to impedance mismatching in the circuit when using the DHPCA-100 current amplifier.

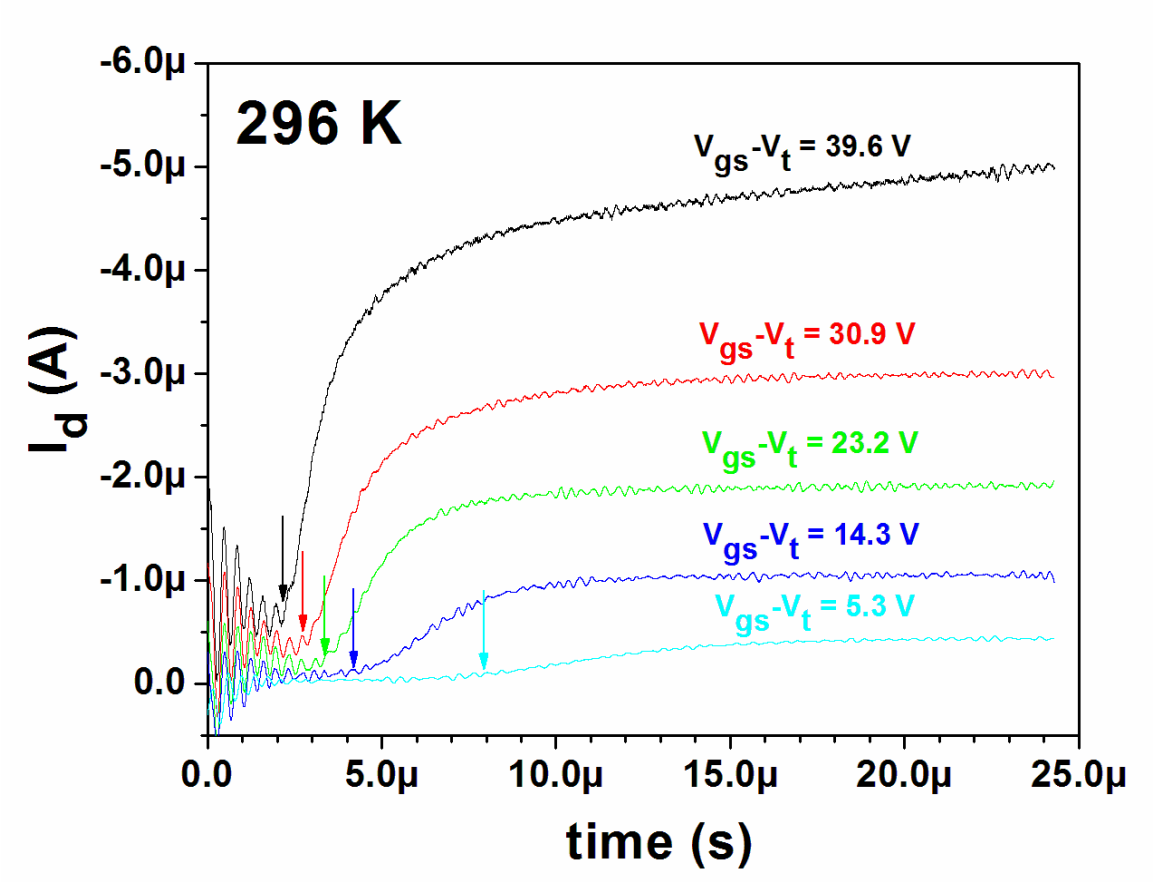

Figure 4.6: Oscilloscope traces of the drain current response to a negative square wave voltage pulse applied at the source contact as a function of V_{gs}-V_t. The turn on times of the OFET are indicated by the arrows above each trace.

These times were used along with the threshold voltages extracted at each temperature and the well known expression for the transient mobility extracted from the FET turn on time first derived by Burns[37]:

$$\mu_{dynamic} = 0.38\frac{L^2}{\tau(V_{gs} - V_t)}. \quad (4.2)$$

Because the channel length of this device was so large (50 μm), and because the largest amplitude of any voltage pulse applied to the source was 50 V (due to the relatively thin gate dielectric and fears of dielectric breakdown at higher voltages), the

largest magnitude of lateral electric field applied between the source and drain was $1x10^4$ V/cm, well below a reasonable threshold at which we can expect to see any dependence of the mobility in these materials on electric field[63]. Therefore the variations in both $\mu_{dynamic}$ and μ_{FE} are caused by changes in the charge carrier density in the device.

The dynamic mobilities extracted from the turn on times and the corresponding FE saturation mobilities are shown for four separate temperatures in Figure 4.7. Note that unlike the pentacene transient and field-effect mobilities shown in Chapter 3, the field effect mobilities do not seem to show any increase with increasing gate voltage. We discuss the physical significance of this observation below. Also, the dynamic mobilities are larger than the field effect mobilities, hinting at a large difference between the mobility of fastest edge of the charge carriers forming the channel and the average mobility of charge carriers in the channel once it has been formed. This, along with our earlier conclusion about the low magnitude of the lateral electric field in the device, gives us important clues about the shape of the DOS below the LUMO band edge of PDI-$8CN_2$ in this device. We elaborate further below.

From Figure 4.7 it is also evident that at low gate voltages the dynamic mobility seems to actually *increase* as the effective gate voltage goes to zero. This is an artifact of the fact that the effective gate voltage (V_{gs}-V_t) is used in the denominator of equation 4.2 to extract transient mobilities. From the inset of Figure 4.4, it is evident that V_t approaches 18 V as the temperature approaches 150 K. Equation 4.2 would predict a spuriously large dynamic mobility for applied source voltage pulses near 18 V at this temperature. Therefore, in the calculations of activation energies shown below, only

dynamic mobility values with a corresponding effective gate voltage greater than 12 V were used.

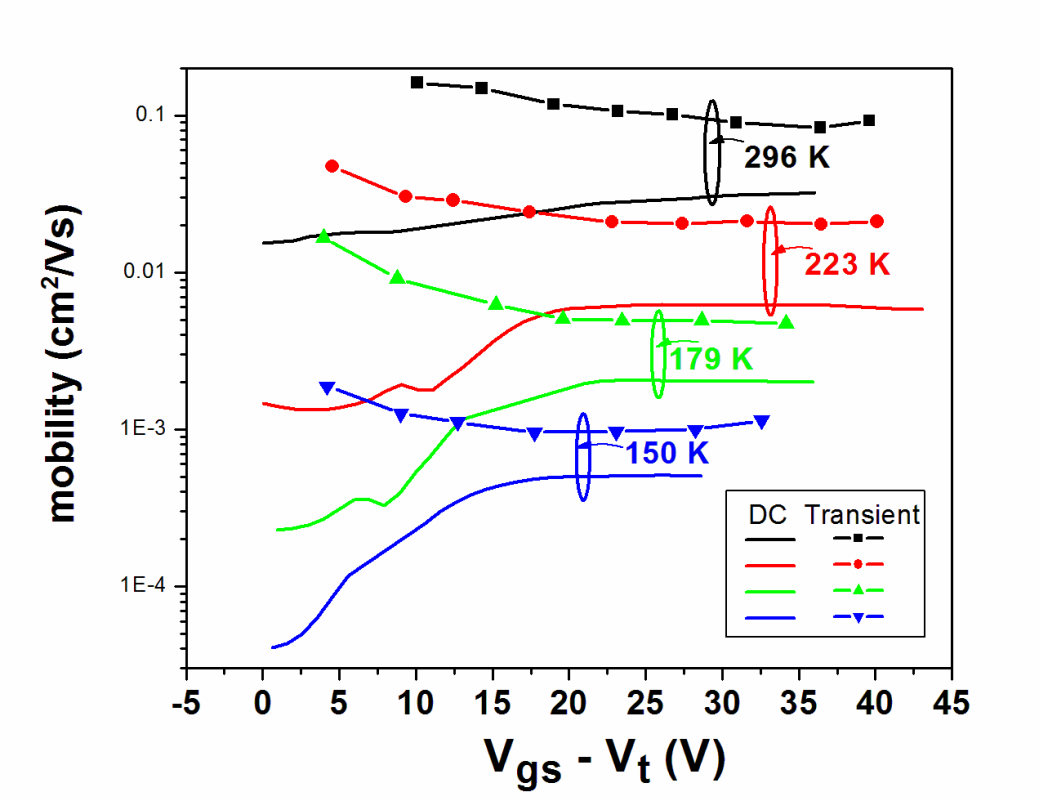

Figure 4.7: Comparison of field-effect and dynamic (or transient) mobilities as a function of effective gate voltage at four separate temperatures, showing clearly that the dynamic mobility values are about a factor of two higher than their field-effect counterparts. Note that the seeming rise in the transient mobility values as the effective gate voltage approaches zero is due to the fact that (V_{gs}-V_t) appears in the denominator of the expression used to calculate $\mu_{dynamic}$.

Because the transient velocities are extracted directly, there is no need to place an analogous restriction on a comparison of DC and transient electron velocities. Here we used the same approach which was described in Chapter 3: The transient velocities were extracted directly from the turn-on time, and are an average measure of the velocities of carriers during the process of channel formation. The DC velocities were extracted by

extracting the saturation regime mobilities in the manner described above (using equation 3.2) only for data points for which $V_{ds} = V_{gs}$ (in order to mimic the conditions in the channel present during the transient measurement). The velocities were then extracted from the simple relationship between the mobility, velocity and electric field: $v = \mu E$, where E is the lateral electric field given by V_{ds} divided by the channel Length. The results are shown below in Figure 4.8, where it is obvious that the transient velocities are almost an order of magnitude larger than the DC velocities. This hints at an especially broad DOS, which we will discuss further below.

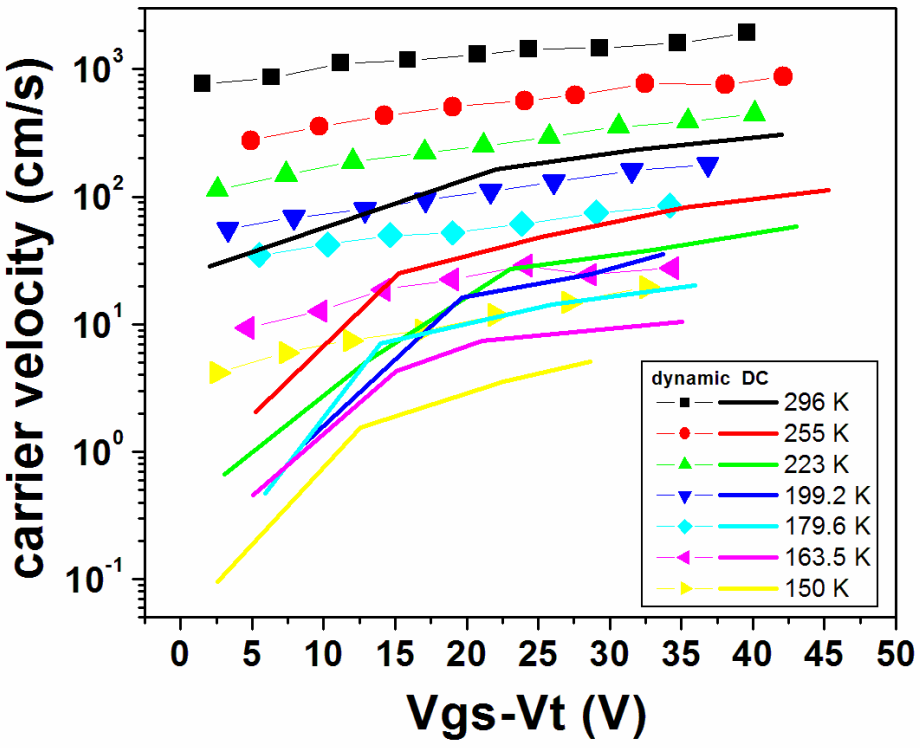

Figure 4.8: Comparison of transient carrier velocities (extracted directly from turn on times of the PDI-8CN$_2$ OFET) and DC velocities, estimated from the saturation regime mobilities for $V_{ds} = V_{gs}$ and lateral electric field.

In order to gain some insight into the nature of charge transport in this system during field-effect and dynamic measurements, the mobility values were sorted according to their value of effective gate voltage. As was the case with the pentacene data in chapter 3, because there was a finite number of current transients recorded, an allowance of +/- 2V around the desired (V_{gs}-V_t) was allowed in order to provide a window large enough to accommodate several mobility values at approximately the same charge carrier density over the range of temperatures over which measurements were made.

As in chapter 3, our strategy was to attempt to fit the data to the well known expression for the mobility consistent with the MTR model: $\mu = \mu_0 exp\left(-\frac{E_a}{k_B T}\right)$, where the activation energy, E_a, may be thought of as an estimate of the distance from the average energy of the trapped charge carriers in the channel to the band edge.

Figure 4.9 shows an Arrhenius plot of the dynamic and field effect mobilities at an effective gate voltage of -27 V, along with the fits used to extract the activation energies. Both mobilities are well described by the simple function relating the mobility to the exponential value of E_a and inverse temperature. As we expected in light of our findings in chapter 3, at the same effective gate voltage the dynamic mobility is characterized by a higher activation energy than the field effect mobility. Again, we attribute this to the lower charge density in the channel during the transient measurement.

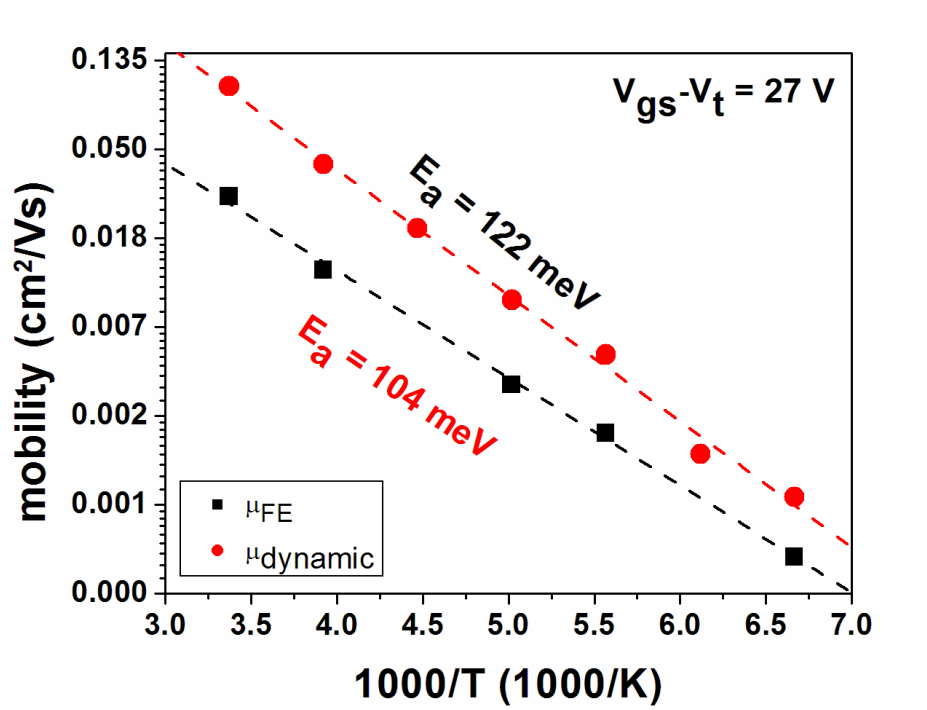

Figure 4.9: An Arrhenius plot of Field effect and dynamic mobilities extracted for an effective gate voltage of -27 V, along with the corresponding fits used to extract activation energies.

However, things get interesting when we attempt to perform a similar analysis at the lower gate voltage of 13 V. The results are shown in Figure 4.10, where the dynamic mobilities are quite well behaved and allow an extraction of a value of $E_{a,dynamic}$ of 127 meV with a high degree of confidence, but the field effect mobilities defy such a simple description. In order to gain a better understanding of the charge transport processes taking place in the channel during the field-effect (DC) mobility measurements, a series of field effect mobilities at increasing effective gate voltages were plotted as a function of inverse temperature. The extremely interesting results are shown in Figure 4.11.

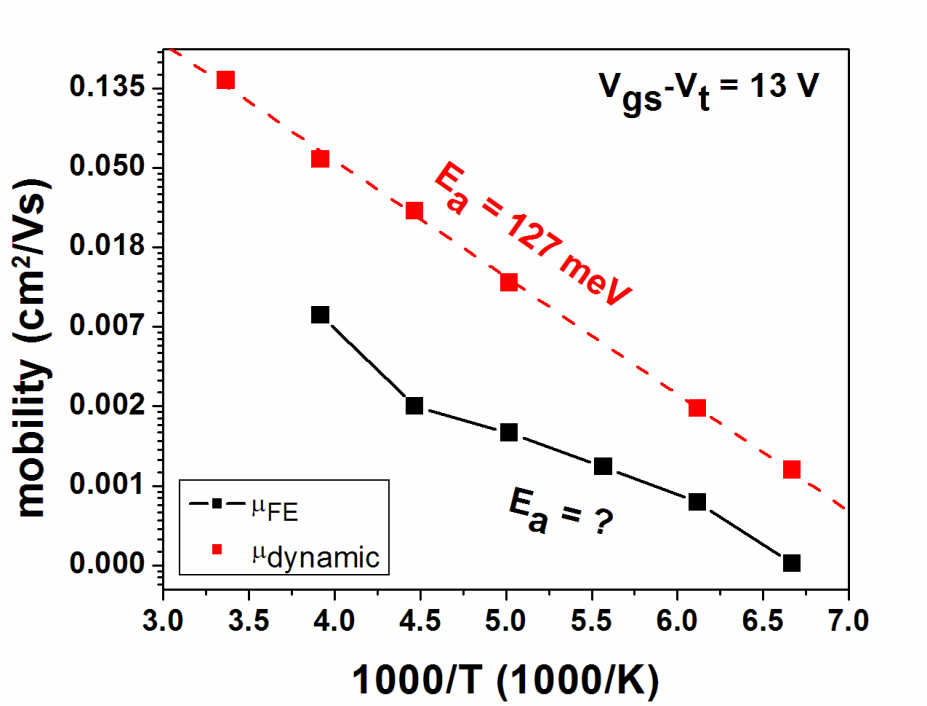

Figure 4.10: An Arrhenius plot of Field effect and dynamic mobilities extracted for an effective gate voltage of -13 V. Note that while the dynamic mobility is well described by $\mu = \mu_0 exp\left(-\frac{E_a}{k_B T}\right)$, the FE mobility exhibits a more complex behavior.

The Arrhenius plot of the field-effect mobility shown in Figure 4.11 may be divided into three distinct regions, characterized by different (or even undefined) activation energies. Region I corresponds to low effective gate voltages (V_{gs}-V_t<5 V) and a high activation energy that sharply decreases with increasing effective gate voltage from about 140 meV at V_{gs}-V_t = 2 V to about 110 meV at V_{gs}-V_t = 5 V. Region III corresponds to high effective gate voltages (V_{gs}-V_t>17 V), and is characterized by an almost unchanging activation energy on the order of 105 meV. This region of unchanging activation energy with increasing gate voltage corresponds to the almost totally flat field-effect mobility curves with increasing effective gate voltage in Figure

4.7. Region II corresponds to effective gate voltages which lie between these two regimes and defies any attempts at activation energy extraction.

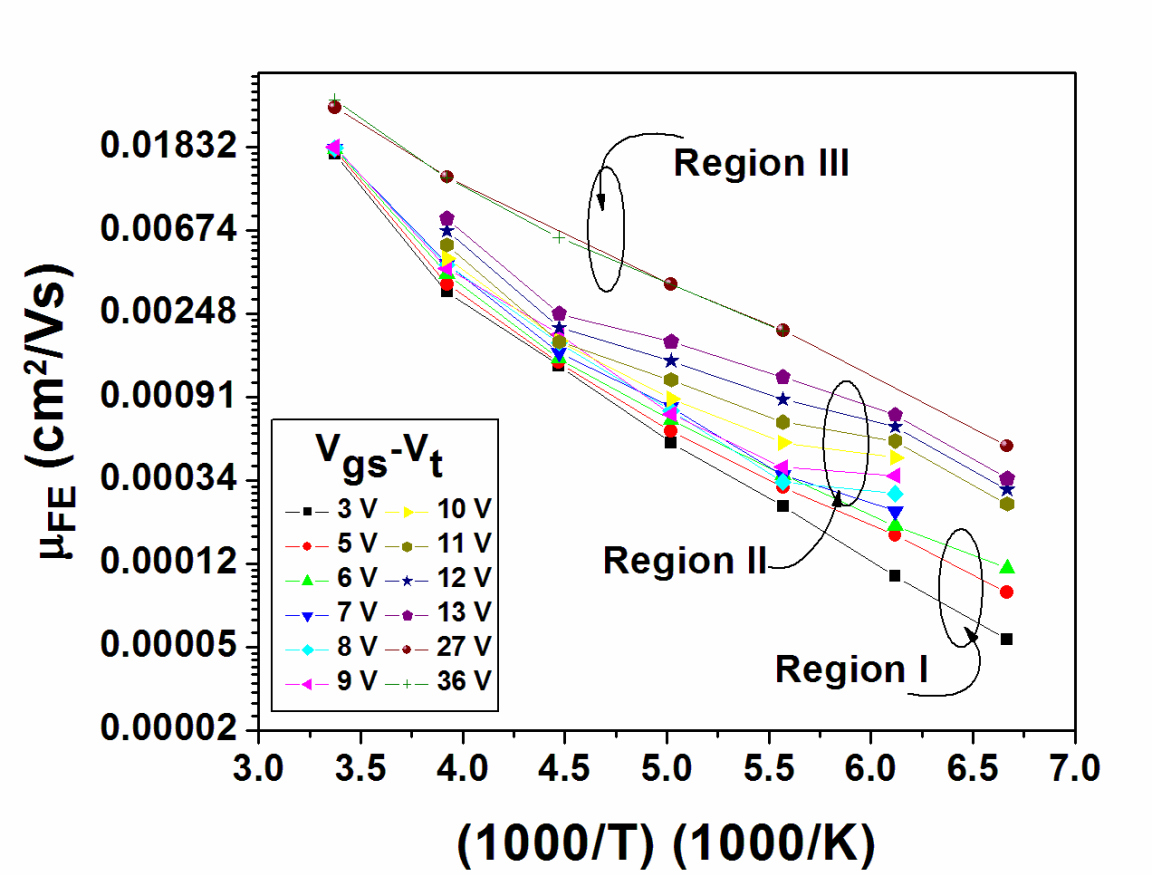

Figure 4.11: Arrhenius plot of a wide range of representative field effect mobility values at varying effective gate voltage values, which are indicated in the legend. There are three distinct regions of interest: Regions I, II, and III correspond to three distinct charge transport regimes which reveal interesting details about the DOS of the material, and are elaborated upon in the text.

The activation energies from the field effect mobility values and the dynamic mobility values are shown plotted together in Figure 4.12. The FE activation energies show a complex dependence on effective gate voltage. The sharp decrease in $E_{a,FE}$ with increasing gate voltage is consistent with the MTR model as was noted in Chapter 3, and is most likely due to the filling of trap states in a narrow exponential tail of trapping

states descending from the LUMO band edge. At intermediate effective gate voltages in Region II the complex behavior of the mobility shown in Figure 4.11 almost certainly reflects a complex feature of the DOS in that energetic region.

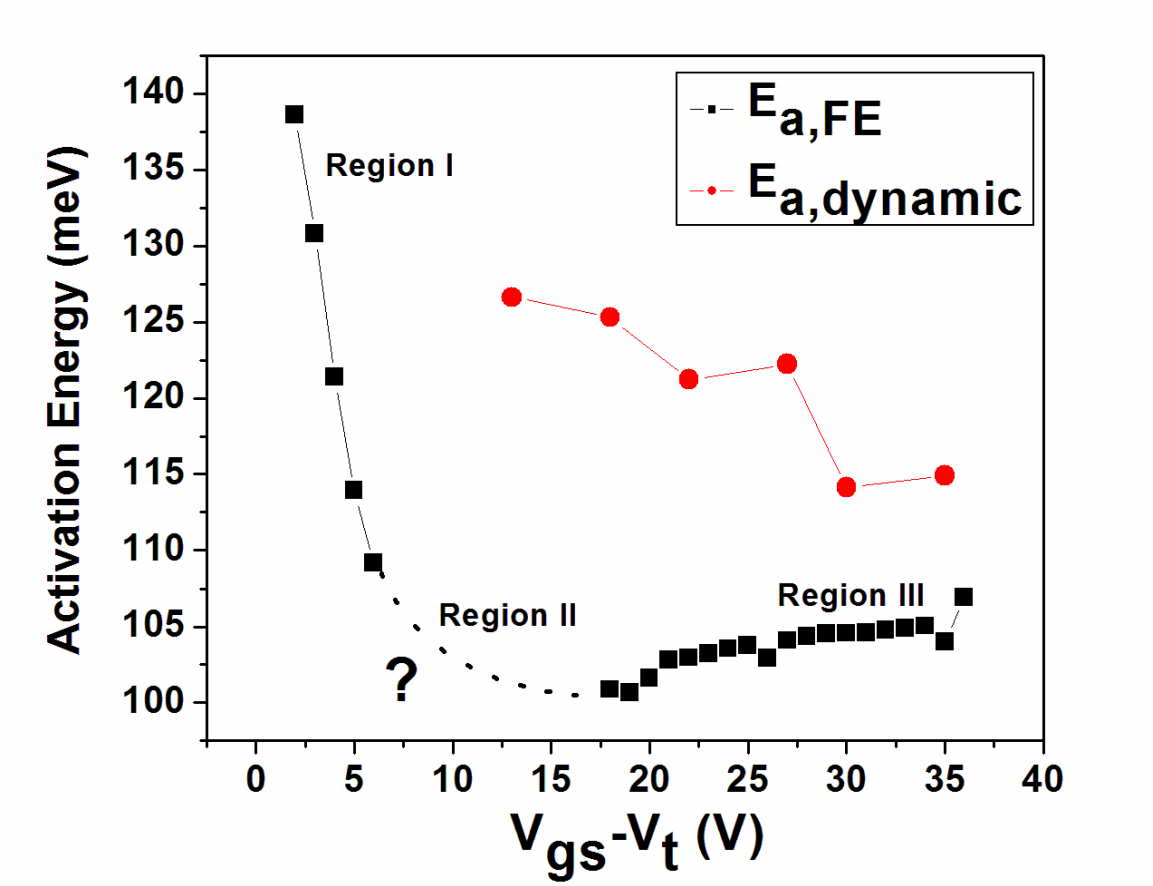

Figure 4.12: Dynamic and field-effect (FE) activation energies extracted from corresponding Arrhenius plots of mobility data. Note that for the field-effect data the dashed line in "Region II" does not correspond to any data, but is merely the author's conjecture at what the activation energy in this region might look like. Note the higher dynamic activation energy compared to the FE activation energy at the same gate voltage.

The plot of $E_{a,FE}$ shown in Figure 4.12 supports this hypothesis: Since for DC measurements the free charge carrier density in the channel is related to the gate voltage through the simple relationship $p = qC_{ins}(V_{gs} - V_t)$, we must conclude that $E_{a,FE}$ transitions from a regime where it is decreasing with increasing free charge carrier

density (as we expect from the MTR model), through a region where it is not well defined (region II) into region III, where it is actually *increasing* with increasing charge carrier density. Regions I and III clearly represent two distinct regions of the DOS distribution, and the behavior of the mobility seen in region II of Figure 4.11 (as well as the proposed behavior of $E_{a,FE}$ in region II of Figure 4.12) corresponds to the average energy of the charge carrier distribution of the OFET moving through the region of the DOS bordering regions I and III.

We note that the dynamic values of the activation energy explore a range of values of $E_{a,dynamic}$ that corresponds to region I of the field-effect activation energies, which also correspond to the lowest charge carrier densities seen in any of the field-effect mobility measurements and subsequent activation energy extractions. We have already concluded in chapter 3 that (at least for a pentacene OFET) the dynamic values of the activation energy mirror the field effect values, but at a higher effective gate voltage, because the same value of (V_{gs}-V_t) in the transient measurement corresponds to a lower charge carrier density than occurs in the device during DC measurements. We therefore propose that the dynamic activation energies would continue to mirror the field-effect activation energies if high enough values of the effective gate voltage could be reached without damaging the device.

We end this chapter by proposing a DOS distribution that could be responsible for the activation energy plot shown in Figure 4.13. We propose that that the sharp decrease of $E_{a,FE}$ with increasing effective gate voltage at low charge carrier densities (Region I) is due to the filling of a deep but narrow distribution of electron traps, possibly due the SiO_2

trapping mechanism illustrated schematically in Figure 4.1. We propose the behavior of $E_{a,FE}$ at high effective gate voltages and carrier densities (Region III) is due to the presence of a relatively shallow but very wide distribution of trapping states that occur at the grain boundaries between crystallites of PDI-8CN_2. The slight *increase* in the activation energy with increasing effective gate voltage could be due to the fact that an increasing gate voltage causes the free charge carriers to move closer to the organic/dielectric interface, where there are a large number of trapped electrons. Another possible explanation has to do with charge injection from the metal contacts into the LUMO level: If the width of the available density of states available for charge injection was relatively narrow, it's conceivable that by increasing the electric field at the metal organic interface, there would be fewer states available for charge carrier injection.

4.4: CONCLUSION

In conclusion, we have successfully measured the temperature dependent field-effect and dynamic mobilities via the "OFET TOF" method, and extracted activation energies from both sets of data, which give an estimate of the shape of the DOS of PDI-8CN_2 on HMDS treated SiO_2.

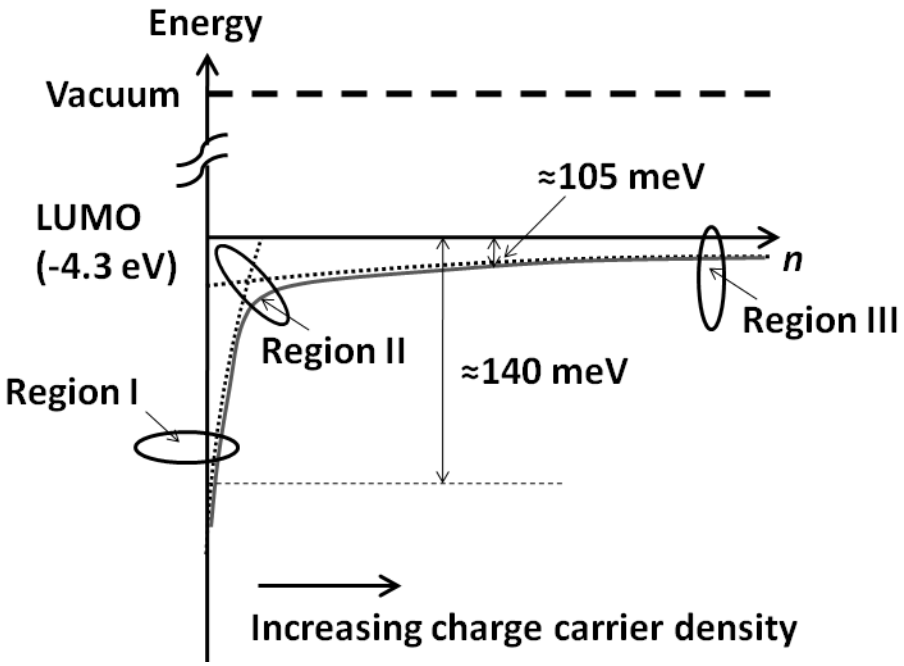

Figure 4.13: Proposed Density of States Distribution of PDI-8CN_2 on HMDS treated SiO2, deduced from the dependence of the field-effect activation energies on effective gate voltage.

Chapter 5: Correlation of Voc Energetic Levels of Organic Photovoltaic Devices Fabricated from Novel Electron Accepting Small Molecules

5.1: Introduction to Organic Photovoltaics and Motivation

Organic solar cells are currently attracting considerable attention due to their potential for low cost power generation and ease of fabrication. The majority of research in this field is currently focused on devices fabricated from blends of polymers such as poly(3-hexylthiophene-2,5-diyl) (P3HT) and functionalized fullerenes such as (6,6)-phenyl C_{61} butyric acid methyl ester (PCBM). However, this material system suffers from several problems including limited absorption in the visible spectrum and an open circuit voltage typically around ~0.6 V. Due to the low dielectric constant of organic semiconductors (~3-4), and localized nature of charges in these materials, when a photon is absorbed in the device a bound electron-hole pair called an exciton is created in either the donor (D) or acceptor (A) phase of the active layer[22]

If the exciton diffuses to the D/A interface from the donor side, it will disassociate if the offset between the two LUMO levels is greater than the binding energy of the exciton, leaving the electron in the lowest unoccupied molecular orbital (LUMO) of the acceptor and the hole in the highest occupied molecular orbital (HOMO) of the donor. The charge carriers are then moved to their respective electrodes due to a combination of drift and diffusion forces. The open circuit voltage (Voc) is the external voltage needed for the injected current to balance the photogenerated current, and along with the fill factor (FF) and short circuit current (Isc) are the key device parameters that govern power

conversion efficiency (η)[64]. The open circuit voltage depends on many factors, including the intensity of the light used for illumination[65], the electron affinity (EA) of the acceptor[66,67], the ionization potential (IP) of the donor[68], the morphology of the blend[69], and broadly, the nature of both the top and bottom metal-organic interfaces *(i.e.* the presence of interface dipoles for certain metal-organic combinations, band bending at ohmic contacts, and injection barriers at non-ohmic contacts)[70]

In the ideal case of a cathode with a work function perfectly matched to the LUMO of the acceptor and an anode with a work function perfectly matched to the HOMO of the acceptor (and no interface dipoles), the maximum obtainable Voc would be given by

$$V_{OC} = \frac{\left(HOMO_{donor} - LUMO_{acceptor}\right)}{q} \tag{5.1}$$

where q is the charge of an electron, and $HOMO_{donor}$ and $LUMO_{acceptor}$ are given in units of eV. Typically, however, if $EA_{cathode} < LUMO_{acceptor}$ (as is often the case for low work function cathodes such as LiF/Al, Ca, or Ba) there is some diffusion of electrons from the metal into the semiconductor, pinning the Fermi level of the cathode to the LUMO level of the acceptor and causing band bending in the semiconductor at the interface due to the build of electrons in that region. An analogous process typically occurs at the anode/organic interface as well. Equation (5.1) must therefore be modified:

$$V_{OC} = \frac{\left(HOMO_{donor} - LUMO_{acceptor}\right)}{q} - \Delta V_A - \Delta V_C \tag{5.2}$$

where ΔV_A and ΔV_C are the voltage drops at the anode and cathode due to the band bending in the semiconductor at those interfaces[64]. A typical value of the voltage drop at each interface under these conditions is ~0.2 V[70]. Although there has historically been controversy in the literature regarding both the HOMO/LUMO levels of commonly used polymers and small molecules, as well as the exciton binding energy, it is generally accepted that in bulk heterojunction organic photovoltaic (OPV) devices the exciton binding energy is on the order of 0.4 eV[71]. As long as the band offsets between the donor and acceptor energy levels remain larger than the exciton binding energy, it should be possible to increase the Voc of an operating device without affecting the exciton dissociation efficiency[72].

With regard to a possible alternative to P3HT as a donor polymer, we have considered poly(3,3’’’-didodecyl quarterthiophene) (PQT-12), which has been reported to have excellent lateral transistor mobilities on the order of 0.18 cm^2/Vs and to form highly ordered films with excellent π-π overlap of lamellar structures[73,74]. OFETs fabricated from PQT-12 have a much greater stability in air than OFETs fabricated from P3HT, which is attributed to the higher IP of PQT-12 resulting in reduced oxidation in ambient[75]. Recent reports in the literature have placed the HOMO level of P3HT at -4.85 eV (measured by ultraviolet photoemission spectroscopy in vacuum)[76] and -5.0 eV (measured by cyclic Voltammetry)[77]. The evidence of greater PQT-12 stability in air, coupled with the P3HT HOMO values from the literature, and the PQT-12 HOMO (LUMO) levels of -5.24 eV (-2.97eV) provided by the manufacturer[78] has led us to

identify PQT-12 as a potential donor polymer that would allow us to increase the Voc of our devices by approximately 0.25 V to 0.4V.

Our group has also previously reported the solution-processable small molecule acceptor 4,7-bis(2-(1-hexyl-4,5-dicyanoimidazol-2-yl)vinyl)benzo(c)1,2,5-thiadiazole (V-BT), as a promising alternative to functionalized fullerenes in OPV devices when blended with both P3HT[79] and a poly(phenylene vinylene) (PPV) derivative[80]. The molecular structures of P3HT, PQT-12, and V-BT are shown in Figure 5.1.

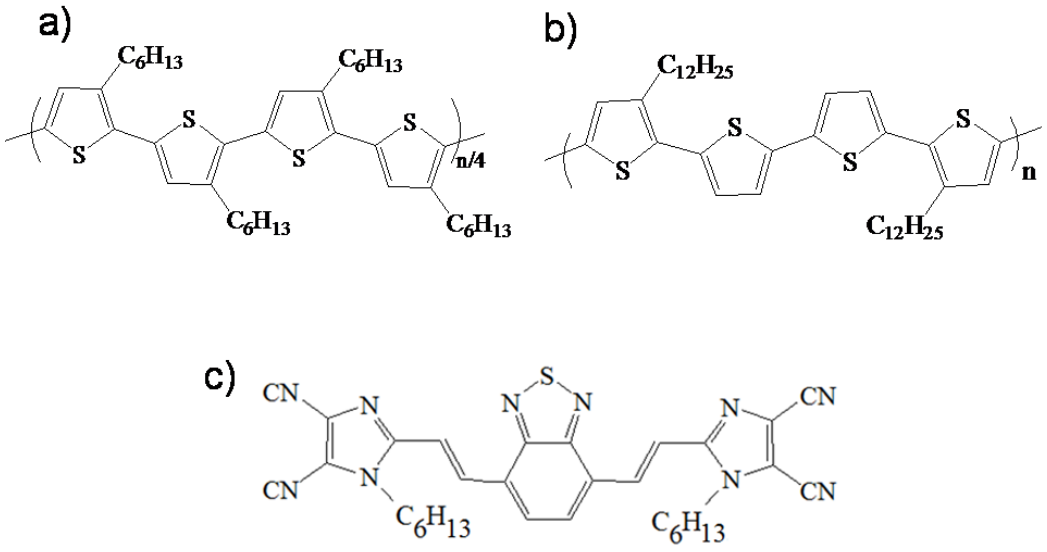

Figure 5.1: The molecular structures of a) P3HT, b) PQT-12, and c) V-BT

Cyclic Voltammetry and UV-Vis band-edge measurements performed by our group have indicated HOMO (LUMO) levels of V-BT to be -5.87 eV (-3.49 eV). These energy levels and the maximum open circuit voltages obtainable in these devices are indicated in Figure 5.2.

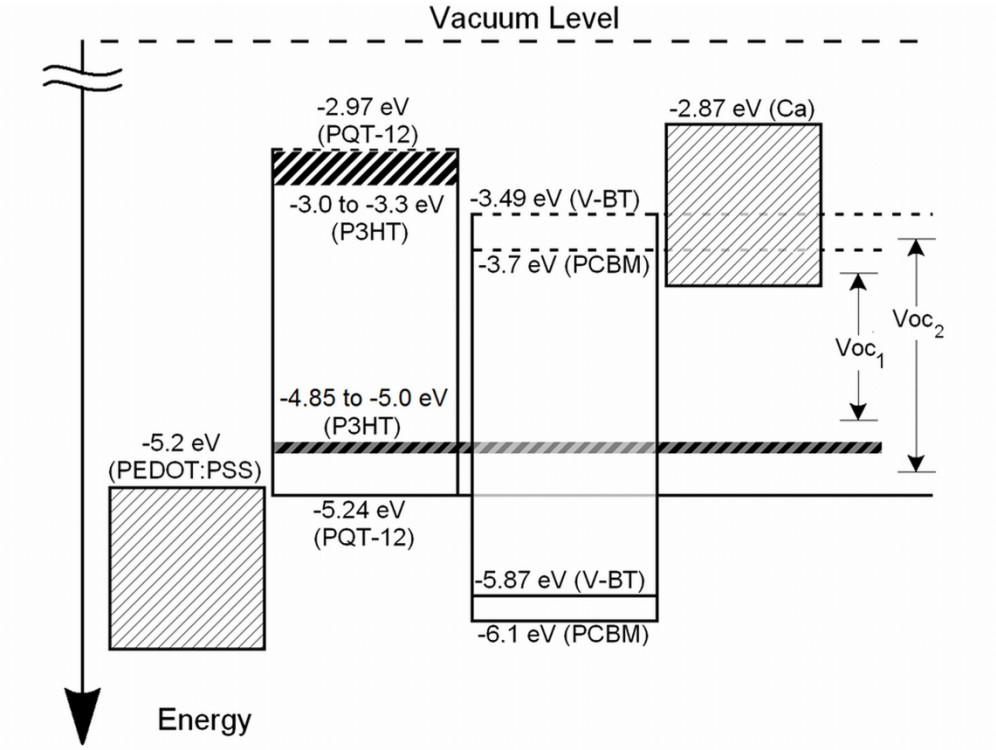

Figure 5.2: Energy level diagram showing the energy levels of P3HT, PQT-12, PCBM, and V-BT. Voc_1 and Voc_2 indicate the maximum obtainable open circuit voltage in a P3HT:PCBM and PQT:V-BT device, respectively.

5.2: ORGANIC PHOTOVOLTAIC DEVICE FABRICATION

We prepared blend devices from solutions of P3HT:V-BT and PQT-12:V-BT (D/A ratios were all 1:1 with solution concentrations of 7 mg/mL dissolved in chloroform). The P3HT had a regioregularity of 90-93%, molecular weight (Mw) 20800 g/mol, polydispersity (PDI) 1.20 as determined by GPC (Rieke Metals Inc., Lincoln, Nebraska), and the PQT-12 had a Mw of 15000-30000 g/mol (ADS Dyes, Quebec, Canada). The V-BT was synthesized in our lab and purified by column chromatography and recrystallization[79]. The P3HT and PQT-12 solutions were both stirred overnight at

50 ◦C, and the V-BT solution was stirred for at least 1 hour at 50 ◦C before the solutions were mixed to create the blends. All solutions were created and stirred in a nitrogen glove box (O_2 < 0.1 ppm, H_2O < 0.1 ppm). Despite the long stirring time at an elevated temperature the PQT-12 was still not completely dissolved in chloroform until the solution was heated to approximately 70 ◦C for a few minutes prior to creating the blend solutions. Indium-tin oxide (ITO) glass slides were carefully etched, rinsed, and cleaned by sonication in detergent, deionized (DI) water, acetone, and methanol, and again in DI water, followed by immersion in an isopropyl alcohol bath, drying with nitrogen, and a 20 minute surface treatment in a UV-Ozone chamber at 100 ◦C.

Poly(3,4-ethylenedioxythiophene):poly(styrenesulfonate) (PEDOT:PSS) (Baytron P standard grade, HC Stark) was spun onto the ITO coated glass at 1500 RPM for 60 seconds in ambient, and samples were immediately transferred to the nitrogen glove box and annealed at 140◦ C for 10 minutes.

All blend films were spun in the glove box at 2000 RPM for 60 s after passing the blend solution through a 0.22 μm-pore size PVDF syringe driven filter (Millipore). Film thicknesses were on the order of 70 nm. Samples were then annealed at temperatures between 60 ◦C and 120 ◦C for 10 minutes. Following spin coating and annealing, samples were transferred to an evaporation chamber without exposure to atmosphere, and *ca*. 15 to 20 nm of Ca and a 100 nm capping layer of Ag were evaporated at pressures below 7.5×10^{-6} torr without breaking the vacuum. Both incident photon conversion efficiency (IPCE) and white light efficiency (AM 1.5 spectrum, 115 mW/cm^2) were measured using a standard solar simulator, and an optically chopped light from a

monochromator coupled with a lock-in amplifier. Details of our measurement setup may be found in Kietzke *et. al.*[80].

5.3: RESULTS AND DISCUSSION

Figure 5.3 shows devices with the highest power conversion efficiencies fabricated from each blend combination. Note that the observed Voc of 0.73 V in the P3HT based devices is an increase of 0.13 V over the typical value of ~0.6 V of P3HT:PCBM based devices, which we attribute to the LUMO level of V-BT being closer to vacuum compared to that of PCBM. The maximum Voc achieved with a PQT-12:V-BT devices is 0.98 V (see inset of Fig. 3), an increase of 0.25 V over the best P3HT:V-BT device, within the range of what we expected from earlier analysis which was outlined schematically in Figure 5.2.

From that analysis, the maximum obtainable values of Voc should be between ~1.35 and ~1.5V for the P3HT based devices, and around ~1.75 V for the PQT-12 based devices, but the experimental results approach 0.75 V and 1.0 V, respectively. If we estimate a ~0.2 V voltage drop at each ohmic contact due to band bending in the semiconductor[8], there remains an additional ~0.2 to ~0.35 V (P3HT based devices) and ~0.35 V (PQT based devices) missing from the Voc values.

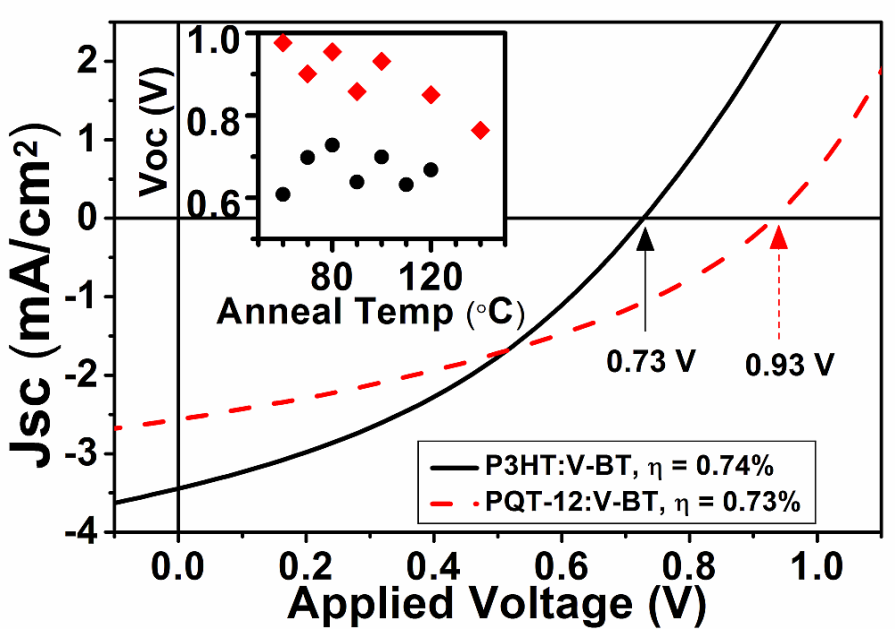

Figure 5.3: Light current-voltage characteristics of highest power conversion efficiency devices: P3HT:V-BT (80 ºC anneal, solid line) and PQT-12:V-BT (100 ºC anneal, dashed line). The Voc and power conversion efficiency of each device is indicated. The inset shows the maximum Voc obtained for both PQT-12:V-BT (red diamonds) and P3HT:V-BT (black circles) as a function of anneal temperature. Note the 0.25V increase in the highest Voc of the achieved with the PQT-12 based devices (0.98 V) over the P3HT based devices (0.73 V).

These losses may be accounted for by the nature of charge transport in disordered organic semiconductors[17] which can be quite successfully modeled using a Gaussian distribution of states with a characteristic standard deviation, σ, on the order of 50-200 meV (depending on the material and amount of disorder). In this model charge transport actually occurs when the carriers hop from site to site via thermal activation, meaning that the majority of charge carriers actually possess an energy below what one would assume from the HOMO/LUMO values. For example, this results in a reduction of the

maximum obtainable Voc of ~0.3 V in PPV:PCBM devices with a Lithium Fluoride/Aluminum cathode[70].

In conclusion, we have shown that PQT-12 may be used to increase the Voc over P3HT based organic photovoltaic devices from 0.73 V to 0.98 V, and that the small molecule V-BT is a promising small molecule acceptor which has been shown to increase the Voc over PCBM based devices. We note that the Voc (0.73 V) and η (0.74%) of our best reported P3HT:V-BT device here shows a marked improvement over our initially reported results of 0.67 V (Voc) and 0.45% (η), respectively[79].

Appendix

```
%Lawrence Dunn's transient OFET simulation program
%11/2008

clear all;
%%%%%%%%%%%%%%%%%%%%%%%%%%%%%%%%%%%%%%%%%%%%%%%%%%%%%%%%%%%%%%%%%%%%%%%%%%%%
%physical constants
e0 = 8.85e-14;  %permittivity of free space in F/cm
eIns = 3.9;  %relative permittivity of the FET dielectric
%Note that eIns = 3.9 for SiO2,
eSemi = 3.0;  %relative permittivity of the semiconductor
q = 1.60218e-19;  %elementary unit of charge in Coulombs
%%%%%%%%%%%%%%%%%%%%%%%%%%%%%%%%%%%%%%%%%%%%%%%%%%%%%%%%%%%%%%%%%%%%%%%%%%%%
%device parameters
tox = 1e-5;  %100 nm expressed in cm
L = 7.5E-4;  %Channel length in cm.  (e.g., 100 um = 1e-2 cm)
W = 2000E-4;  %Channel width in cm.  (e.g., 1000 um = 1e-2 cm)
%Cox = (e0*eIns)/tox;  %capacitance of the dielectric in F/cm^2.
%Defining the dielectric capacitance explicitly:
Cox = 16.9E-9;
Cbar = W*L*Cox/L;  %Capacitance per unit length
Vt = 0;  %Threshold voltage in V
Vd = 0;  %Drain Voltage
Vs = -19.8651;  %Source Voltage Pulse Magnitude.
Vg = 0;  %Gate Voltage:
RScope = 750;  %Ohms

%%%%%%%%%%%%%%%%%%%%%%%%%%%%%%%%%%%%%%%%%%%%%%%%%%%%%%%%%%%%%%%%%%%%%%%%%%%%
%Width Normalized Source and drain resistances in Ohm-cm.  At Room Temp
%for top contact gold/pentacene devices reasonable numbers are about
%2000 Ohm-cm.  For Bottom Contact gold/pentacene devices, it's more
%like 50,000 Ohm-cm.  See:  Frisbee et. al., JAP, Vol 99, p. 094504
%(2006).

RSourceWidthNorm = 1.4E4;
RDrainWidthNorm = 1.4E4;
RSource = RSourceWidthNorm/W;
RDrain = RDrainWidthNorm/W;

%%%%%%%%%%%%%%%%%%%%%%%%%%%%%%%%%%%%%%%%%%%%%%%%%%%%%%%%%%%%%%%%%%%%%%%%%%%%
%defining spatial 1-D Grid and number of time steps
N = 101;  %Number of Points on the grid.
dx = L/(N-1);  %spacing between points in the grid
X = (0:dx:L);
dt = 1e-12;  %time step in seconds;
NumTimeSteps = 600000;
tFinal = NumTimeSteps*dt; %time at the end of the simulation in seconds

%%%%%%%%%%%%%%%%%%%%%%%%%%%%%%%%%%%%%%%%%%%%%%%%%%%%%%%%%%%%%%%%%%%%%%%%%%%%
```

```
%Compression Factor.  if CompFactor = 1000, the code will export every
%1000th data point of Idrain
CompFactor = 3000;

%%%%%%%%%%%%%%%%%%%%%%%%%%%%%%%%%%%%%%%%%%%%%%%%%%%%%%%%%%%%%%%%%%%%%%%%%%%%
%defining parameters for Poole-Frenkel dependence of mobiliy on
%Electric field.
kb = 8.6173e-5;  %Boltzmann constant in eV/K
temp = 300;  %temperature in degrees Kevlin.
beta = 5.8e-5;  %field dependent coefficient in the Poole-Frenkel
%mobility dependent expression.  Units are eV*(V/cm)^1/2
delta = 0.05; %zero field hopping barrier or low field activiation
%energy in eV
%Defining Mobility Vector.  Poole Frenkel mobility definied within for
%loop
mup = zeros(N,1);

%%%%%%%%%%%%%%%%%%%%%%%%%%%%%%%%%%%%%%%%%%%%%%%%%%%%%%%%%%%%%%%%%%%%%%%%%%%%
%Defining time, timeShort, and IDrain vectors.
time = (1:NumTimeSteps)*dt;
timeShort = zeros(NumTimeSteps/CompFactor+1,1);
Idrain = zeros(NumTimeSteps/CompFactor+1, numVgSteps);

%%%%%%%%%%%%%%%%%%%%%%%%%%%%%%%%%%%%%%%%%%%%%%%%%%%%%%%%%%%%%%%%%%%%%%%%%%%%
%Initial Boundary Conditions and applied voltages
V = zeros(N,1);  %Defining V(x,t) for t = 0;
V(1,1) = Vs;
V(N,1) = Vd;
Vbar = Vg-Vt-V;  %defining Vbar(x,t) = Vg(t)-Vt-V(x,t) for t= 0;
I = zeros(N,1);  %defining I(x,t) for t = 0;

Ron = 1;
%%%%%%%%%%%%%%%%%%%%%%%%%%%%%%%%%%%%%%%%%%%%%%%%%%%%%%%%%%%%%%%%%%%%%%%%%%%%
dVbydx = zeros(N,1);
dVbydt = zeros(N,1);
d2Vbydx2 = zeros(N,1);
dmupbydx = zeros(N,1);

time = zeros(NumTimeSteps,1);
z0 = 2*(Vt-Vg);

z = 1;
q = 1;

%%%%%%%%%%%%%%%%%%%%%%%%%%%%%%%%%%%%%%%%%%%%%%%%%%%%%%%%%%%%%%%%%%%%%%%%%%%%
%For loop calculating time progression of voltage and current across
%the channel

for m = 1:NumTimeSteps

    if m>=2
```

```
        time(m) = time(m-1)+dt;
    end

    dVbydx(2) = (V(3)-V(2))/dx;
    dVbydx(1) = (V(2)-V(1))/dx;
    dVbydx(N) = (V(N)-V(N-1))/dx;
    dVbydx(N-1) = (V(N-1)-V(N-2))/dx;
    dVbydx(3:N-2,1) = (V(4:N-1,1)-V(2:N-3,1))/(2*dx);


    mup(:,1) = 0.06643;
    dmupbydx(4:N-3,1) = (mup(5:N-2,1)-mup(3:N-4,1))/(2*dx);
    dmupbydx(3,1) = (mup(3,1)-mup(2,1))/dx;
    dmupbydx(N-2,1) = (mup(N-2,1)-mup(N-3))/dx;


    d2Vbydx2(2) = (dVbydx(3)-dVbydx(2))/dx;
    d2Vbydx2(1) = (dVbydx(2)-dVbydx(1))/dx;
    d2Vbydx2(N) = (dVbydx(N)-dVbydx(N-1))/dx;
    d2Vbydx2(N-1) = (dVbydx(N-1)-dVbydx(N-2))/dx;
    d2Vbydx2(3:N-2,1) = (V(4:N-1,1)+V(2:N-3,1)-(2*V(3:N-2,1)))/(dx*dx);

    LHSterm1 = (mup.*V.*d2Vbydx2);
    LHSterm2 = (mup.*dVbydx.*dVbydx);
    LHSterm3 = (0.5*z0*mup.*d2Vbydx2);
    LHSterm4 = (V.*dVbydx.*dmupbydx);
    LHSterm5 = (0.5*z0*dVbydx.*dmupbydx);

    dVbydt(3:N-2,1) = -1*(LHSterm1(3:N-2,1)+LHSterm2(3:N-
2,1)+LHSterm3(3:N-2,1)+LHSterm4(3:N-2,1)+LHSterm5(3:N-2,1));
    V(3:N-2,1) = V(3:N-2,1) + dt*dVbydt(3:N-2,1);

    Rch(2:N-2,1) = dx./(mup(2:N-2,1).*Cbar.*(Vg-Vt-V(2:N-2,1)));
%Resistance per Unit Length at each point
    Rch(1) = RSource;
    Rch(N-1) = RDrain;
    Rch(N) = RScope;

    V(2) = V(1)+(RSource*( (V(3)-V(1))/(RSource+Rch(2))));
    V(N-1) = (RDrain+RScope)*(V(N-2)/(Rch(N-2)+RDrain+RScope));
    V(N) = RScope*(V(N-2)/(Rch(N-2)+RDrain+RScope));

    I(3:N-2,1) = -Cbar*mup(3:N-2,1).*(Vg-Vt-V(3:N-2,1)).*(dVbydx(3:N-
2,1));  %defining I(x,t)

    I(2) = I(3);
    I(1) = I(2);
    I(N-1) = I(N-2);
    I(N) = I(N-1);
```

```
if z == CompFactor
    %%%%%%%%%%%%%%%%%%%%%%%%%%%%%%%%%%%%%%%%%%%%%%%%%%%%%%%%%%%%%%%%%%%%%%%
    %IChannelOut is a matrix of the current values along the
    %channel at different times that will later be exported as a
    %text file.
    timeOut(q,1) = time(m);
    IDrainOut(q,1) = I(N-1,1);
    IChannelOut(q,1:N) = I(1:N,1);
    VChannelOut(q,1:N) = V(1:N,1);
    %%%%%%%%%%%%%%%%%%%%%%%%%%%%%%%%%%%%%%%%%%%%%%%%%%%%%%%%%%%%%%%%%%%%%%%

    %  Uncomment this section if you want to plot Current vs
    %distance along the channel.  Note an avi movie file of the
    %current progression is also exported.

    %         plot(X,I(:,1), 'r-', 'LineWidth', 2.0);
    %         axis([0 .00075 -2E-4 1E-5]);
    %         timeText = strvcat(['channel length = '
    %          num2str(7.5)'um'],...
    %             ['mobility ~ 0.067 cm^2/Vs'],...
    %             ['Vgs-Vt ~ -' num2str(20) 'V'],...
    %             ['time = ' num2str(dt*m) 's'],...
    %             ['IDrain = ' num2str(IDrainOut(q,1)) 'A']);
    %         text(.0004, -1.5E-4, timeText);
    %
    %         xlabel('distance along channel (cm)')
    %         ylabel('current (A)')
    %
    %         if m == (CompFactor)
    %             aviobj = avifile([pwd '\transientMovie.avi']);
    %
    %         elseif m > (CompFactor)
    %             aviobj = addframe(aviobj,gcf);
    %         end
    %
    %         drawnow;


    plot(X,V(:,1), 'r-', 'LineWidth', 2.0);
    axis([0 .00075 -20 1]);
    timeText = strvcat(['channel length = ' num2str(7.5) 'um'],...
        ['mobility ~ 0.067 cm^2/Vs'],...
        ['Vgs-Vt ~ -' num2str(20) 'V'],...
        ['time = ' num2str(dt*m) 's'],...
        ['IDrain = ' num2str(IDrainOut(q,1)) 'A']);
    text(.0004, -16, timeText);

    xlabel('distance along channel (cm)')
    ylabel('Voltage (V)')
```

```
        if m == (CompFactor)
            aviobj2 = avifile([pwd '\transientVoltageMovie.avi']);

        elseif m > (CompFactor)
            aviobj2 = addframe(aviobj2,gcf);
        end

        drawnow;

        q = q+1
        z = 1;

    end
    z = z+1;

end

clear mex;


%%%%%%%%%%%%%%%%%%%%%%%%%%%%%%%%%%%%%%%%%%%%%%%%%%%%%%%%%%%%%%%%%%%%%%%%%%%%
%Saving DC Id values to a text file;

titleLine = ('time,Id');
for j = 1:length(titleLine)
    IDrainOutText(1,j) = titleLine(1,j);
end

for j = 2:(length(IDrainOut)+1)
    tempStr = ([num2str(timeOut(j-1,1)) ',' num2str(IDrainOut(j-
1,1))]);
    IDrainOutText(j,1:length(tempStr)) = tempStr;
end

[numLinesText,trash] = size(IDrainOutText);

fileName = ([pwd '\IDrainOut.txt']);
fid = fopen(fileName, 'wt');

if (fid < 0)
    error(['could not open file' fileName]);
end;

for i = 1:numLinesText
    textMessage = char(IDrainOutText(i,:));
    fprintf(fid, '%s\n', textMessage);
    clear textMessage
end
fclose(fid);
%%%%%%%%%%%%%%%%%%%%%%%%%%%%%%%%%%%%%%%%%%%%%%%%%%%%%%%%%%%%%%%%%%%%%%%%%%%%
```

Bibliography

[1]R. Farchioni and G. Grosso, *Organic Electronic Materials: Conjugated Polymers and Low Molecular Weight Organic Solids*, Springer-Verlag Press (2001)

[2]J. Mort, *Phys. Today* **47**, 32 (1994)

[3]R. Saito, C. Dresselhaus and M. S. Dresselhaus, *Physical Properties of Carbon Nanotubes*, Imperial College Press (2003)

[4]Z. Bao and J. Locklin, *Organic Field-Effect Transistors*, CRC Press (2007)

[5]W. H. Brown and C. S. Foote, *Organic Chemistry*, Harcourt Brace College Publishers (1998)

[6]D. J. Griffiths, *Introduction to Quantum Mechanics*, Prentice Hall, Inc. (1995)

[7]J. L. Brédas, J. P. Calbert, D. A. da Silva Filho and J. Cornil, *Proc. Nat. Acad. Sci. U.S.A.* **99**, 5804 (2002)

[8]R. E. Peierls, *Quantum Theory of Solids*, Oxford University Press (1965)

[9]N. Karl, *Festkörperprobleme 14*, Springer (1974)

[10]N. Karl, *Syn. Met.* **133-134**, 649 (2003)

[11]N. Karl, K. H. Kraft, J. Marktanner, M. Munch, F. Schatz, R. Stehle and H. M. Uhde, *J. Vac. Sci. Technol., A* **17**, 2318 (1999)

[12]M. Pope and C. E. Swenberg, *Electronic Processes in Organic Crystals and Polymers*, Oxford University Press (1999)

[13]L. Torsi, A. Dodabalapur, L. J. Rothberg, A. W. P. Fung and H. E. Katz, *Science* **272**, 1462 (1996)

[14]R. A. Marcus, *Rev. Mod. Phys.* **65**, 599 (1993)

[15]R. A. Marcus, *Annu. Rev. Phys. Chem.* **15**, 155 (1964)

[16]B. S. Brunschwig and N. Sutin, *Coord. Chem. Rev.* **187**, 233 (1999)

[17]H. Bässler, *Phys. Stat. Sol. B* **175**, 15 (1993)

[18]Y. N. Gartstein and E. M. Conwell, *Chem. Phys. Lett.* **245**, 351 (1995)

[19]A. B. Walker, A. Kambili and S. J. Martin, *J. Phys.: Condens. Matter* **14**, 9825 (2002)

[20]S. V. Novikov, D. H. Dunlap, V. M. Kenkre, P. E. Parris and A. V. Vannikov, *Phys. Rev. Lett.* **81**, 4472 (1998)

[21]M. Knupfer, *Appl. Phys. A* **77**, 623 (2003)

[22]S. E. Gledhill, B. Scott and B. A. Gregg, *J. Mater. Res.* **20**, 3167 (2005)

[23]G. Horowitz, *Adv. Mat.* **10**, 365 (1998)

[24]J. E. Lilienfeld, U. S. Patent Number 1,745,175 (1930)

[25]W. F. Brinkman, D. E. Haggan and W. W. Troutman, *IEEE J. Solid-State Circuits* **32**, 1858 (1997)

[26]M. E. Gershenson, V. Podzorov and A. F. Morpurgo, *Rev. Mod. Phys.* **78**, 973 (2006)

[27]V. Podzorov, S. E. Sysoev, E. Loginova, V. M. Pudalov and M. E. Gershenson, *Appl. Phys. Lett.* **83**, 3504 (2003)

[28]P. G. Le Comber and W. E. Spear, *Phys. Rev. Lett.* **25**, 509 (1970)

[29]A. B. Chwang and C. D. Frisbie, *J. Appl. Phys.* **90**, 1342 (2001)

[30]T. Minari, T. Nemoto and S. Isoda, *J. Appl. Phys.* **96**, 769 (2004)

[31]M. C. J. M. Vissenberg and M. Matters, *Phys. Rev. B* **57**, 12964 (1998)

[32]C. Tanase, E. J. Meijer, P. W. M. Blom and D. M. de Leeuw, *Phys. Rev. Lett.* **91**, 216601 (2003)

[33]L. Dunn, D. Basu, L. Wang and A. Dodabalapur, *Appl. Phys. Lett.* **88**, 063507 (2006)

[34]R. Dost, A. Das and M. Grell, *J. Appl. Phys.* **104**, 084519 (2008)

[35]L. Wang, D. Fine, D. Basu and A. Dodabalapur, *J. Appl. Phys.* **101**, 054515 (2007)

[36]W. D. Gill, *J. Appl. Phys.* **43**, 5033 (1972)

[37]J. R. Burns, *RCA Rev.* **30**, 15 (1969)

[38]P. V. Pesavento, K. P. Puntambekar, C. D. Frisbie, J. C. McKeen and P. P. Ruden, *J. Appl. Phys.* **99**, 094504 (2006)

[39]L. Dunn, B. Cobb, D. Reddy and A. Dodabalapur, *Appl. Phys. A* **In Press**, (2008)

[40]R. Dost, A. Das and M. Grell, *J. Phys. D: Appl. Phys.* **40**, 3563 (2007)

[41]D. J. Gundlach, J. Li Li and T. N. Jackson, *IEEE Electron Device Lett.* **22**, 571 (2001)

[42]G. Horowitz, M. E. Hajlaoui and R. Hajlaoui, *J. Appl. Phys.* **87**, 4456 (2000)

[43]V. Podzorov, E. Menard, A. Borissov, V. Kiryukhin, J. A. Rogers and M. E. Gershenson, *Phys. Rev. Lett.* **93**, 086602 (2004)

[44]T. Minari, T. Nemoto and S. Isoda, *J. Appl. Phys.* **99**, 034506 (2006)

[45]A. Dodabalapur, L. Torsi and H. E. Katz, *Science* **268**, 270 (1995)

[46]S. E. Fritz, S. M. Martin, C. D. Frisbie, M. D. Ward and M. F. Toney, *J. Am. Chem. Soc.* **126**, 4084 (2004)

[47]A. R. Brown, C. P. Jarrett, D. M. de Leeuw and M. Matters, *Syn. Met.* **88**, 37 (1997)

[48]C. Rost, D. J. Gundlach, S. Karg and W. Riess, *J. Appl. Phys.* **95**, 5782 (2004)

[49]M. Ahles, R. Schmechel and H. von Seggern, *Appl. Phys. Lett.* **85**, 4499 (2004)

[50]B. A. Jones, A. Facchetti, M. R. Wasielewski and T. J. Marks, *J. Am. Chem. Soc.* **129**, 15259 (2007)

[51]B. A. Jones, M. J. Ahrens, M.-H. Yoon, A. Facchetti, T. J. Marks and M. R. Wasielewski, *Angewandte Chemie International Edition* **43**, 6363 (2004)

[52]B. Yoo, T. Jung, D. Basu, A. Dodabalapur, B. A. Jones, A. Facchetti, M. R. Wasielewski and T. J. Marks, *Appl. Phys. Lett.* **88**, 082104 (2006)

[53]J. L. Brédas, J. Cornil, D. Beljonne, A. D. Santos and Z. Shuai, *Accouns of Chemical Research* **32**, 267 (1999)

[54]C. Winder and N. S. Sariciftci, *J. Mater. Chem.* **14**, 1077 (2004)

[55]B. d. Boer, A. Hadipour, M. M. Mandoc, T. v. Woudenbergh and P. W. M. Blom, *Adv. Mat.* **17**, 621 (2005)

[56]L.-L. Chua, J. Zaumseil, J.-F. Chang, E. C. W. Ou, P. K. H. Ho, H. Sirringhaus and R. H. Friend, *Nature* **434**, 194 (2005)

[57]L. Schmidt-Mende, A. Fechtenkötter, K. Müllen, E. Moons, R. H. Friend and J. D. MacKenzie, *Science* **293**, 1119 (2001)

[58]T. J. Marks, M. R. Wasielewski, A. Facchetti, M. J. Ahrens, B. A. Jones and M.-H. Yoon, US 2005/0176970 A1 (2005)

[59]B. Yoo, A. Madgavkar, B. A. Jones, S. Nadkarni, A. Facchetti, K. Dimmler, M. R. Wasielewski, T. J. Marks and A. Dodabalapur, *IEEE Electron Device Lett.* **27**, 737 (2006)

[60]H. Sirringhaus, *Adv. Mat.* **17**, 2411 (2005)

[61]C. D. Dimitrakopoulos and P. R. L. Malenfant, *Adv. Mat.* **14**, 99 (2002)

[62]S. C. Veenstra, A. Heeres, G. Hadziioannou, G. A. Sawatzky and H. T. Jonkman, *Appl. Phys. A* **75**, 661 (2002)

[63]L. Wang, G. Liu, H. Wang, D. Song, B. Yu and D. Yan, *Appl. Phys. Lett.* **91**, 063511 (2007)

[64]V. D. Mihailetchi, *Device Physics of Organic Bulk Heterojunction Solar Cells*, Thesis, University of Groningen (2005)
[65]L. J. A. Koster, V. D. Mihailetchi, R. Ramaker and P. W. M. Blom, *Appl. Phys. Lett.* **86**, 123509 (2005)

[66]C. J. Brabec, A. Cravino, D. Meissner, N. S. Sariciftci, T. Fromherz, M. T. Rispens, L. Sanchez and J. C. Hummelen, *Adv. Funct. Mater.* **11**, 374 (2001)

[67]C. J. Brabec, A. Cravino, D. Meissner, N. S. Sariciftci, M. T. Rispens, L. Sanchez, J. C. Hummelen and T. Fromherz, *Thin Solid Films* **403-404**, 368 (2002)

[68]A. Gadisa, M. Svensson, M. R. Andersson and O. Inganas, *Appl. Phys. Lett.* **84**, 1609 (2004)

[69]J. Liu, Y. Shi and Y. Yang, *Adv. Funct. Mater.* **11**, 420 (2001)

[70]V. D. Mihailetchi, P. W. M. Blom, J. C. Hummelen and M. T. Rispens, *J. Appl. Phys.* **94**, 6849 (2003)

[71]S. Barth and H. Bässler, *Phys. Rev. Lett.* **79**, 4445 (1997)

[72]L. J. A. Koster, V. D. Mihailetchi and P. W. M. Blom, *Appl. Phys. Lett.* **88**, 093511 (2006)

[73]B. S. Ong, Y. Wu, P. Liu and S. Gardner, *J. Am. Chem. Soc.* **126**, 3378 (2004)

[74]Y. Wu, P. Liu, B. S. Ong, T. Srikumar, N. Zhao, G. Botton and S. Zhu, *Appl. Phys. Lett.* **86**, 142102 (2005)

[75]B. S. Ong, Y. Wu and P. Liu, *Proc. IEEE* **93**, 1412 (2005)

[76]A. J. Cascio, J. E. Lyon, M. M. Beerbom, R. Schlaf, Y. Zhu and S. A. Jenekhe, *Appl. Phys. Lett.* **88**, 062104 (2006)

[77]Y. Liu, M. A. Summers, C. Edder, J. M. J. Fréchet and M. D. McGehee, *Adv. Mat.* **17**, 2960 (2005)

[78]http://www.adsdyes.com/products/pdf/polythiophene/ADS12PQT_DATA.pdf

[79]R. Y. C. Shin, T. Kietzke, S. Sudhakar, A. Dodabalapur, Z.-K. Chen and A. Sellinger, *Chem. Mater.* **19**, 1892 (2007)

[80]T. Kietzke, R. Y. C. Shin, D. A. M. Egbe, Z.-K. Chen and A. Sellinger, *Macromolecules* **40**, 4424 (2007)

Vita

Lawrence Dunn was born in Chicago, Illinois on June 16, 1980, the son of Robert and Anna Dunn. He completed his high school studies at the Arkansas School for Mathematics and Sciences in Hot Springs, Arkansas, in 1998. He graduated with a B.A. in physics *cum laude* and with distinction from Hendrix College in Conway, Arkansas in the spring of 2002. He began his graduate studies in physics at the University of Texas at Austin in the fall of 2002 and was awarded his M.A. in physics in December, 2004 under Dr. Gary Wilson. He joined the group of Prof. Ananth Dodabalapur in January, 2005, to begin his doctoral work at the Microelectronics Research Center at the University of Texas. From September, 2005 to September, 2007, he conducted research under Prof. Dodabalapur and Dr. Alan Sellinger at the Institute of Materials Research and Engineering, Singapore.

Permanent address: 4608 Cedar Point Drive, Austin TX 78723

This dissertation was typed by the author.